Sensitivity and fragmentation calibration of the ROSINA Double Focusing Mass Spectrometer

Inauguraldissertation
der Philosophisch-naturwissenschaftlichen Fakultät
der Universität Bern

vorgelegt von

Myrtha Marianne Hässig

von Krummenau SG

Leiterin der Arbeit:

Prof. Dr. Kathrin Altwegg

Physikalisches Institut der Universität Bern

Urheberrechtlicher Hinweis

Sensitivity and fragmentation calibration of the ROSINA Double Focusing Mass Spectrometer

Inauguraldissertation
der Philosophisch-naturwissenschaftlichen Fakultät
der Universität Bern

vorgelegt von

Myrtha Marianne Hässig

von Krummenau SG

Leiter/in der Arbeit:

Prof. Dr. Kathrin Altwegg

Physikalisches Institut der Universität Bern

Von der Philisophisch-naturwissenschaftlichen Fakultät angenommen.

Bern, den 06.09.2013

Der Dekan:
Prof. Dr. S. Decurtins

Abstract

The goal of this work has been to calibrate sensitivities and fragmentation pattern of various molecules as well as further characterize the lab model of the ROSINA Double Focusing Mass Spectrometer (DFMS) on board ESA's Rosetta spacecraft bound to comet 67P/Churyumov-Gerasimenko. The detailed calibration and characterization of the instrument is key to understand and interpret the results in the coma of the comet. A static calibration was performed for the following species: Ne, Ar, Kr, Xe, H_2O, N_2, CO_2, CH_4, C_2H_6, C_3H_8, C_4H_{10}, and C_2H_4. The purpose of the calibration was to obtain sensitivities for all detectors and emissions, the fragmentation behavior of the ion source and to show the capabilities to measure isotopic ratios at the comet. The calibration included the recording of different correction factors to evaluate the data, including a detailed investigation of the detector gain. The quality of the calibration that could be tested for different gas mixtures including the calibration of the density inside the ion source when calibration gas from the gas calibration unit is introduced. In conclusion the calibration shows that DFMS meets the design requirements and that DFMS will be able to measure the D/H at the comet and help shed more light on the puzzle about the origin of water on Earth.

Last compiled: 12.08.2013

Contents

List of Tables

List of Figures

1 Introduction

The origin of planetary systems starts with the collapse of a molecular cloud (mainly hydrogen), that compresses the matter in the center. A disc is formed around the center of gravity because of the conservation of the angular momentum. In the center of the disc and fed from the gaseous and solid material falling inward from the disc a protostar starts to form. The protostar is heated because during the collapse gravitational energy is conversed into kinetic energy. Once the temperature in the protostar reaches about 10^6 K, nuclear reactions are initiated and the protostar starts to burn [de Pater and Lissauer, 2001]. In the cooling process protoplanetary discs around it, elements and molecules undergo chemical reactions as a consequence of different temperatures and pressures. This non-trivial processes are difficult to understand because of uncertainties in the condensation sequence and since non-equilibirum chemistry plays an important role especially in the cold outer regions of the protoplanetary disc [de Pater and Lissauer, 2001]. The remaining material in the disc is then the start for planetesimals that might accrete material and grow to planetary embryos. The most massive planetesimals have the largest gravitational cross section and gain additional mass if the escape velocity does not exceed the relative velocity of the surrounding objects. How bodies from centimeter- to kilometer-size were grown is still poorly understood [Irvine and Lunine, 2004]. Eventually planetary embryos gather most of the solids through their gravitational influence and become planets. It is assumed that gravitational and magnetic torques launch waves in the gas and dust. By compressing and heating material it might be that giant gaseous planets such as Jupiter and Saturn can form [Irvine and Lunine, 2004]. The only planetary system where detailed information is available is the solar system. The formation of the solar system occurred in a similar way approximately 4.6 Gyr ago.

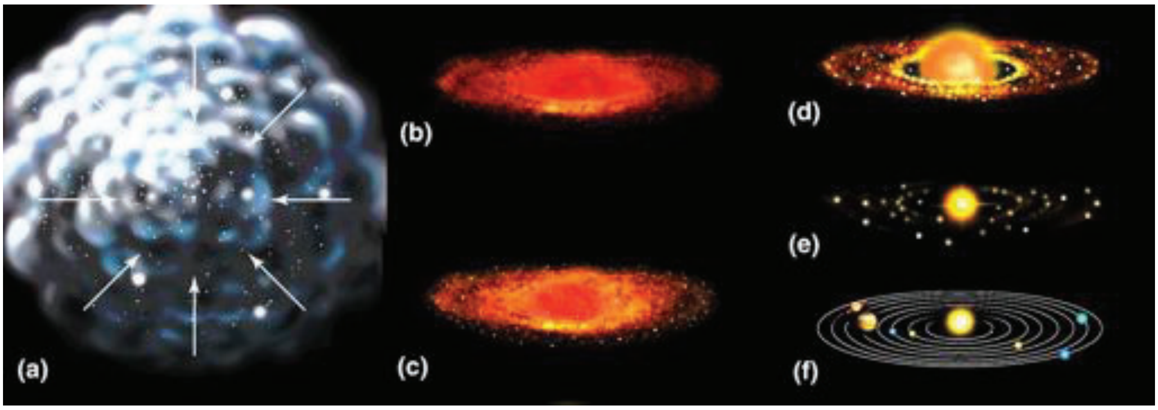

Figure 1: The formation of the solar system as schematics: (a) The molecular cloud, (b) Collapsing of the molecular cloud and formation of a disc, (c) The protostar starts to form, (d) The protostar starts burning and planetesimals build in the disc, (e) The most massive planetesimals become planetary embryos, and (f) The planets are formed. Image credit: Penn State University (2013)

The planetary system contains the star close to the center and planets orbiting the barycenter of the system. The remaining planetesimals can be trapped by the planets and form moons if not already formed during the accretion or stay loose in the form of e.g. the asteroid belt.

A schematic overview of the solar system can be found in Fig. 2. The variety of objects in a planetary system is not limited to stars, planets, and moons but contains a variety of smaller objects: Dwarf planets, asteroids, and comets. The dwarf planets are the most massive small objects and are in hydrostatic equilibrium after accumulating enough material during planet formation process. The most popular dwarf planet is Pluto. These objects have typically a diameter of a few hundred kilometers and can be seen as representatives of planetary embryos. Ceres, also a dwarf planet because of its size, can also be seen as the largest asteroid in the asteroid belt [Jewitt et al., 2008]. The smaller bodies in the solar system are either asteroids or comets, depending on their appearance at the sky. Asteroids are depleted in volatiles and consist mainly of refractory material. Therefore, asteroids don't show signs of a sublimation driven atmosphere. Asteroids in the solar system can be found from inside Mercury's orbit to outside the orbit of Neptune [de Pater and Lissauer, 2001]. Most known asteroids are concentrated between the orbits of Mars and Jupiter, known as the asteroid belt. The depletion in volatiles in asteroids has long been regarded as a consequence of the snowline concept. The snowline is commonly referred to as the heliocentric distance where water condenses and ice can be formed and is located between the orbit of Jupiter and Mars. Volatiles condensed at large heliocentric distances from the Sun during the condensation sequence of the protoplanetary disc. Closer to the Sun temperatures are higher and gas was swept away during periods of high solar activity. Therefore asteroids show a depletion of volatiles. In the asteroid belt occasionally collisions between asteroids can happen and scatter objects towards the Earth as meteorites.

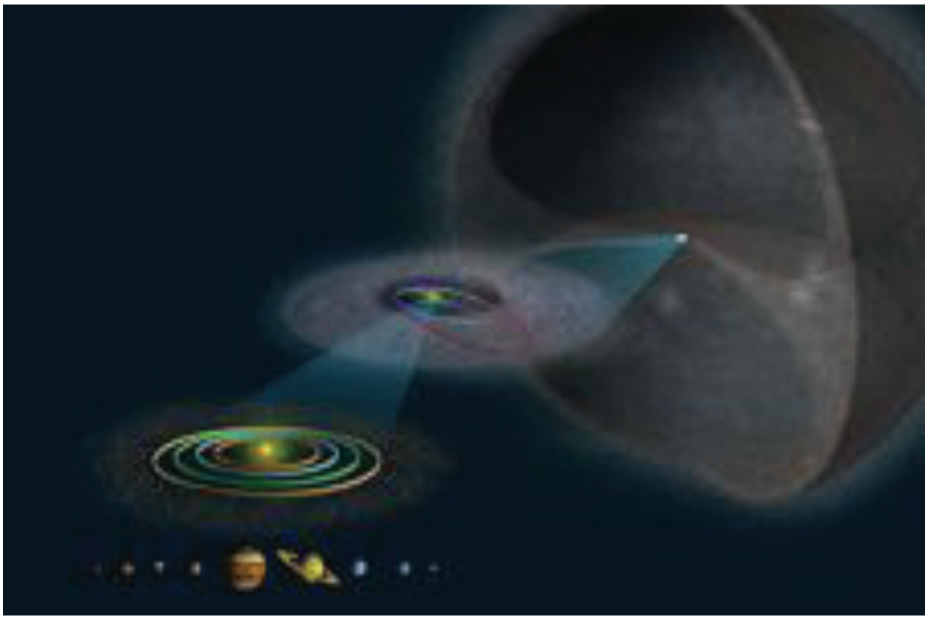

Figure 2: The schematic drawing of the solar system. From the lower left to the upper right corner: The planets of the solar system, the inner solar system with the orbits of the four inner planets and the asteroid belt, the solar system with the Kuiper belt, and the Oort cloud. Image credit: Svitil and Foley (2004).

The comets are an other group of small bodies and consist of an ice rich nucleus with low albedo. The nucleus can produce a gravitationally unbound atmosphere (coma) that is mainly driven by sublimation from the surface of the nucleus. The apparent active area of the nucleus can be enlarged by icy grains that are lifted from the surface of the nucleus and sublimate [A'Hearn et al., 2011]. When the comet gets closer to the Sun, it starts to build up a tail, containing ions and/or dust particles (see Fig. 3). Because of conservation of angular momentum of the dust particles, they slow down as they are pushed away from the comet by gas drag and solar radiation, resulting in a curvature of the tail in the opposite direction of the comets motion [de Pater and Lissauer, 2001]. In contrast to this curved shaped tail, the usually blueish tail consists of ions, neutrals, and points away from the Sun. The ions are bound to the interplanetary magnetic field lines and dragged along with the solar wind [de Pater and Lissauer, 2001]. Cometary orbits are eccentric ellipses, so that only a small fraction of the time on an orbit is spent in the inner planetary region. Comets spend most of their time in the cold outer part of the solar system and are therefore believed to contain and preserve material from the formation of the solar system. There exist two main population of comets according to their current location: The Oort cloud comets and the Kuiper belt comets. The Oort cloud is a spherical distribution of comets at distances of $> 10^4$ AU [de Pater and Lissauer, 2001]. The Oort cloud was postulated by Jan Oort due to observations of dynamically 'new' long-period comets. Because of the distribution of the semi-major axis and the inclination of the comets, that were observed at that time and scattered into the inner solar system, Oort postulated a spherical shaped cloud as the reservoir and origin of this comets [de Pater and Lissauer, 2001].

The other reservoir is the Kuiper belt, a disc shaped distribution of icy bodies beyond the orbit of Neptune, and these objects are therefore often referred to as Trans-Neptunian Objects. The Kuiper belt contains objects with low inclination orbits and is, based on dynamical arguments, divided into several subgroups: The classical Kuiper belt objects have low eccentricity orbits at heliocentric distances that are approximately $32 < a < 50$ AU [Morbidelli and Brown, 2004] and stable over the age of the solar system. Gravitational scattering of these objects by Neptune can cause highly eccentric orbits. An-other subset of the population of the Kuiper belt is in an orbital resonance of 3:2 with Neptune, the best known object thereof is Pluto. Comets originating from the Kuiper belt can be trapped by Jupiter once they are scattered into the inner solar system and become short period comets being called Jupiter family comets (JFC) [Jewitt et al., 2008].

The connection between the Oort cloud and the Kuiper belt was given by the discovery of Sedna (90377) with a high semi-major axis of 480 ± 40 AU and a perihelion of 76 ± 4 AU [Brown et al., 2004]. Since Sedna can be assigned neither to the Kuiper belt nor to the distant Oort cloud it must therefore be a transitional object of the inner Oort cloud.

For completeness a third group of possible comets is mentioned, the main belt comets (MBC). These comets have orbits in the main asteroid belt between Mars and Jupiter. These objects can show dust tails or even persistent dust emissions over timescales of months [Jewitt et al., 2008]. These outbursts were long believed to originate from collisions but might represent another population of comets although they might also be captured comets from other regions.

Small bodies have experienced relatively little changes since their formation, compared to planets or dwarf planets, that underwent alteration due to collisions and differentiation. Comets build behind the snowline and the amount of volatiles incorporated is therefore supposed to be high, and since they spend most of their life time far away from the Sun at low temperatures, comets are thought to contain the most pristine material in the solar system. Due to low temperatures at large heliocentric distances, there might have been even an incorporation of pristine dust particles in comets which are older than the dark molecular cloud [de Pater and Lissauer, 2001]. The Nice model [Gomes et al., 2005, Tsiganis et al., 2005, Morbidelli et al., 2005], postulates that the gas giants underwent orbital migration and forced objects in the asteroid belt and/or Kuiper belt on eccentric orbits that put them in the path of the terrestrial planets. During this late heavy bombardment comets might have brought water and even pre-biotic molecules to Earth and Mars. However, the role of comets as a source of water on Earth was long questioned, or at least thought to be of limited importance because of the different D/H ratios found in comets compared to Earth (e.g. Halley: Balsiger et al. (1995) and Eberhardt et al. (1995)). But recent remote sensing measurements of comet 103P/Hartley 2 (see Fig. 4) by the Herschel Space Observatory found an ocean-like D/H ratio [Hartogh et al., 2011] and might bring back comets as possible sources for water on Earth. However, the measurements of one Jupiter family comet is a fairly small sample. Further in situ measurements with instruments that provide the D/H ratio in water at a comet that originates in the Kuiper belt might shed more light on the riddle about the origin of the water on terrestrial planets.

Figure 3: Comet Hale-Bop with the straight ion tail in blueish and the slightly curved dust tail. Image credit: Jewitt et al. (2008)

Figure 4: The greyish nucleus of comet Hartley 2 and belongs to the group of JFC. Image credit: NASA/JPL-Caltech/UMD

2 Rosetta

Rosetta is a planetary cornerstone mission of the European Space Agency (ESA). The name of Rosetta originates from the famous Rosetta Stone. The reason for the naming is given in Berner et al. (2002) and a summary thereof shall be given here: the stone was found by French soldiers in 1799 near the village Rashid (Rosetta) in Egypt's Nile delta when they prepared to destroy a wall. The stone is made of granodiorite, a rock similar to granite, with an inscription. The inscriptions on the stone were identified as three different languages: hieroglyphs, Egyptian demotic, and Greek. While the hieroglyphs were more of a language in pictures for the priests, the demotic represents the written language of ancient Egypt people. By comparing the inscription it became clear that the three parts in three different languages contained essentially the same text with minor differences. Therefore the stone provided the key to the modern understanding of the Egyptian hieroglyphs and the history of a long lost culture.

Similar to the discovery of the Rosetta stone eventually leading to the deciphering of the hieroglyphs, the Rosetta mission will help scientist to unravel some of the mysteries of comets, in particular 67P/Churyumov-Gerasimenko. Comets are considered to be the most primitive objects in the solar system and the building blocks from which planets are formed, similar to the hieroglyphs as building blocks of the Egyptian language. Comets still contain ices and dust present in the original solar nebula at the time of their formation and therefore grant a unique glimpse into the conditions when our solar system emerged.

2.1 The Mission

The first and very successful ESA comet mission was Giotto which flew by comet 1P/Halley in 1986 and the Rosetta mission is the logical continuation of ESA's comet investigations. In the mean time there were several NASA missions to comets, e.g. Wild 2 with Stardust in encounter 2004 and Hartley 2 with Deep impact encounter 2010. The main scientific objective of Rosetta is to investigate the origin of the solar System through the close inspection of a comet by means of orbiter and probe. A detailed description of the Rosetta mission can be found in Schulz et al. (2009). The Rosetta spacecraft consists of an orbiter and a lander called Philae. The Rosetta spacecraft was launched in March 2004 by an Ariane-5G+ from Kourou (French Guiana) more than one year after scheduled departure. This was due to an Ariane failure in December 2002, causing the postponement of the launch. The target was switched from comet 46P/Wirtanen to 67P/Churyumov-Gerasimenko. To gain enough energy to match the orbit of the comet, several gravity assists were performed at Earth and Mars. Rosetta will escort 67P/Churyumov-Gerasimenko from more than 3 AU in heliocentric distance, when the cometary activity is still very low to past perihelion (maximal activity). During the encounter the lander will be first released for a close investigation of the nucleus while the orbiter will orbit around the comet and investigate the comet with unprecedented precision. The notable milestones of the mission during the 10 years of voyage and the following investigation of the comet are summarized in Tab. 1.

The gravity assists at the planets were required to gain enough energy to reach the orbit of 67P/Churyumov-Gerasimenko and were a chance to test the scientific instrument package. In addition they represent a great possibility to keep up the general public interest over the long mission duration. The scientific highlights during the mission are, besides the close investigation of the comet, two asteroid flybys: 2687 Steins and 21 Lutetia (see Fig. 5). Documentation of the two successful asteroid flybys of Steins and Lutetia can be found in

Table 1: Milestones of the Rosetta mission.

Mission events	Date
Launch in Kourou	02.03.2004
1. Earth gravity assist	04.03.2005
Mars gravity assist	25.02.2007
2. Earth gravity assist	13.11.2007
2867 Steins flyby	05.09.2008
3. Earth gravity assist	13.11.2009
21 Lutetia flyby	10.07.2010
Rendezvous maneuver 1	23.01.2011
Start hibernation	08.06.2011
Wake up from hibernation	20.01.2014
Rendezvous maneuver 2	22.05.2014
Orbit around 67P	Sept. 2014
Lander (Philae) delivery	11.11.2014
Perihelion Passage	Aug. 2015
Nominal end of mission	31.12.2015

Keller et al. (2010) for Steins and in the special issue of Schulz et al. (2012) for Lutetia and are not further discussed in this work.
Rosetta is the first spacecraft to cross the Jovian orbit using solar cells as its main power source. However during deep space cruise, the spacecraft is placed in hibernation with most electrical systems switched off to limit consumption of power and fuel. After the wake-up from hibernation in January 2014 the spacecraft will perform a rendezvous maneuver to reach the orbit of the comet. A series of measurements before and after lander delivery will be performed to safely release the lander on the comet's surface. Once the lander reaches the surface, it will be the first controlled touch down of a man-made probe on the nucleus of a comet and its close and detailed investigation with combined forces of orbiter and lander can begin. The measurement goals of the Rosetta mission include [Schwehm and Schulz, 1999]:

- Global characterization of the nucleus, it's surface morphology and composition
- Determination of the dynamical properties of the nucleus
- Determination of chemical, mineralogical, and isotopic composition of volatiles and refractories in the cometary nucleus
- Determination of the physical properties and interrelation of volatiles and refractories in the cometary nucleus
- Studies of the development of cometary activity and the processes in the surface layer of the nucleus and inner coma, that is dust/gas interaction
- Studies of the evolution of the interaction region of the solar wind and the outgassing comet during perihelion approach.

These prime objectives are, if successfully accomplished, considered to be crucial to address key questions of the origin and formation of the solar system.

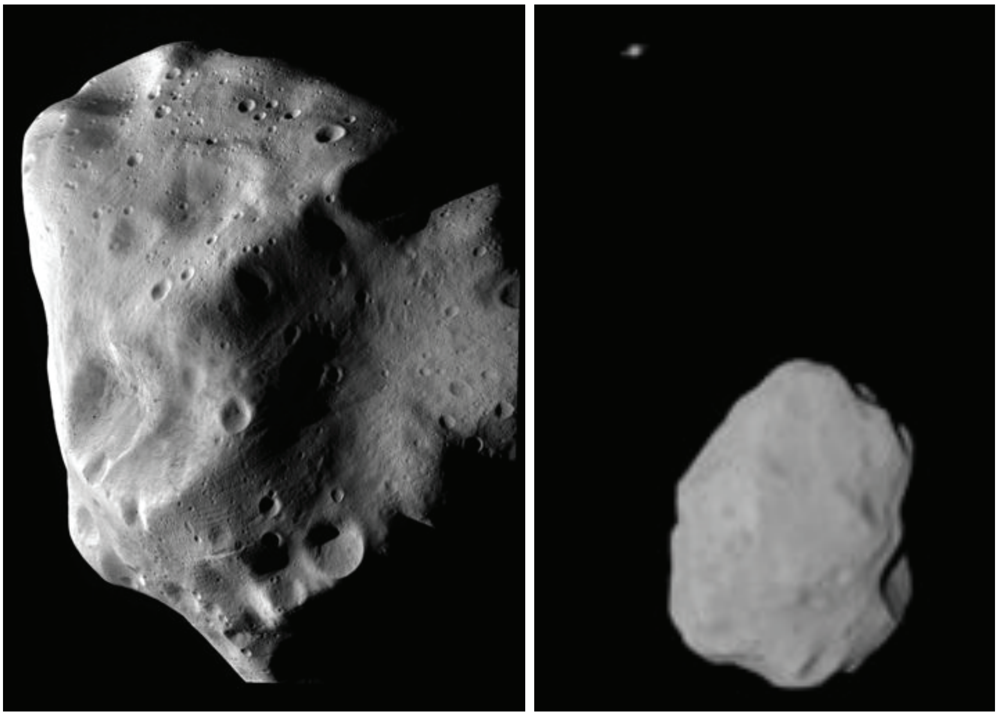

Figure 5: *Left*: Asteroid Lutetia at closest approach. *Right*: Lutetia in conjunction with Saturn. Image credits: ESA 2010 MPS for OSIRIS Team MPS/UPD/LAM/IAA/RSSD/INTA/UPM/DASP/IDA

2.2 67P/Churyumov-Gerasimenko

Comet 67P/Churyumov-Gerasimenko was first discovered in 1969 by Klim Ivanovic Churyumov and Svetlana Ivanova Gerasimenko. The comet could be observed to this day on seven perihelion passages (last perihelion passage 28. February 2009 [Lara et al., 2010]). The comet is classified as a short period comet of the Jupiter Family Comet class, based on its orbital period of 6.45 y and the aphelion distance of 5.7 AU [JPL, 2013]. The origin of JFC's is believed to be the Kuiper Belt, where gravitational encounters with outer planets let them migrate into the inner solar system. The orbits of JFC's are controlled by Jupiter, while orbital elements can be significantly changed by repeated encounters with Jupiter. It is known through backwards calculations [Lamy et al., 2009], that the orbital elements of 67P/Churyumov-Gerasimenko have significantly changed after a close encounter with Jupiter (at a distance of only 0.0518 AU) in 1959, resulting in a perihelion change from 2.78 AU to 1.28 AU, increasing eccentricity from 0.36 to 0.63, and shortening of the orbital period from 8.97 to 6.55 y. An overview of the current orbital elements can be found in Tab. 2.

The comet 67P/Churyumov-Gerasimenko (67P) had emerged as favorable alternative to the initial target 46P/Wirtanen, after cancellation of the original Rosetta launch in January 2003. In the following the target of Rosetta became the subject of several ground-based as well as space-borne (e.g. Hubble Space Telescope) observations. The result of these observations lead to sufficient knowledge about the physical characteristics of the main target to plan the mission. However these properties will be updated once Rosetta is at the

Table 2: Orbital and physical characteristics of 67P/Churyumov-Gerasimenko [Lamy et al., 2009]

Orbit	
Perihelion distance	1.29 AU
Aphelion distance	5.71 AU
Eccentricity	0.63
Inclination	7.13°
Orbital period	6.45 y
Nucleus	
Effective radius	3.38-4.40 km
Rotation period	(12.72 ± 0.05) h
R-band geometric albedo	0.037-0.043
Bulk density	0.1-0.6 g cm^{-3}
Mass	0.3-1.6 x 10^{13} kg

comet. The approximate activity of the comet can be found in Lamy et al. (2009) and is crucial for the mission planing.

2.2.1 Trajectories

There are in principle two possible trajectories to fly around the comet: bound orbits and flybys. While there exist several restrictions due to instrument as well as spacecraft safety, the trajectories are highly dependent on the comet's activity. Never the less the amount of propellant to spend on trajectories is limited and therefore trajectories should be planned carefully to maximize the scientific output.

Bound orbits are circular shaped orbits in the gravitational field of the comet and as such have a rather low usage of propellant. The Kepler velocity of the spacecraft around the comet (v_K) is given by the equilibrium of the gravitational force (F_G) and the centrifugal force (F_{cf}) acting on the spacecraft. F_G depends on the constant of gravitation ($G = 6.67428 \cdot 10^{-11} \frac{m^3}{kgs^2}$), the mass of Rosetta ($m_R$), the mass of the comet (m_c) and the distance between the spacecraft and the comets center of gravity (r). F_{cf} depends on m_R, r, and the velocity of the spacecraft around the comet $v_{s/c}$.

$$|\vec{F_G}| = \frac{G m_R m_C}{r^2} = m_R \frac{v_K^2}{r} = |\vec{F_{cf}}| \tag{1}$$

$$v_K = \sqrt{\frac{G m_C}{r}} \tag{2}$$

The Kepler velocity depends on the mass of the comet (m_c) as well as the distance of the spacecraft to the comet's center of mass (r). The minimum velocity of the spacecraft due to safety reasons including maneuver uncertainties can be assumed to be 0.08 m/s, therefore bound orbits are possible for $r \leq 30$ km.

Other forces that have to be taken into account are the gas drag from the out streaming gas of the comet and the radiation pressure from the Sun.

The gas drag[a] depends strongly on the gas flux coming from the comet as well as the exposed area of the spacecraft and is pointing away from the comet.
The gas flux coming from the comet is the gas density multiplied by the gas velocity (v_{gas} [b]). The gas density depends on the activity of the comet, Q,v_{gas}, and r. The affected area of the spacecraft is the area of the cube plus the exposed area of the solar panels and, since the solar panels are always perpendicular to the Sun, this area is known. The area depends on the sub-solar angle of the spacecraft. The gas drag is always pointing away from the comet, however, this is the most difficult force to predict since the out-streaming gas is not likely to be spherically symmetric and the absolute activity is difficult to predict. The radiation pressure exerted by the Sun depends on the affected area of the spacecraft as well as the distance from the Sun. The affected area is always the full cross-section of the solar panels and the spacecraft body while the distance between the comet and the Sun (and therefore between spacecraft and Sun) decreases. This force will therefore increase during the journey of the comet towards the Sun and is always pointing away from the Sun.
Restrictions due to spacecraft safety are: position and maneuver uncertainties, the avoidance of the shadow of the comet (no power), the platform where the radiators and the lander is/was mounted should not be exposed to the Sun at a distance < 2.2 AU, the safety during a failure mode while the spacecraft is proceeding on the flight path till it can be recovered. The navigation camera needs a reference point within its field of view and should avoid the direct sunlight.
Furthermore the following important parameters need to be considered for planning: spin axis of the comet, seasons of the comet, the cumulative flux of the trajectories (given by $1/r^2$ x time spent) and last but not least time and pointing uncertainties of the spacecraft as well as the measurements.
Bound orbits are possible in the terminator plane (plane between night and day side of the comet) with a maximal tilt angle of $< 30°$ (due to the navigation camera) at a distance (r) ≤ 30 km with a velocity relative to the

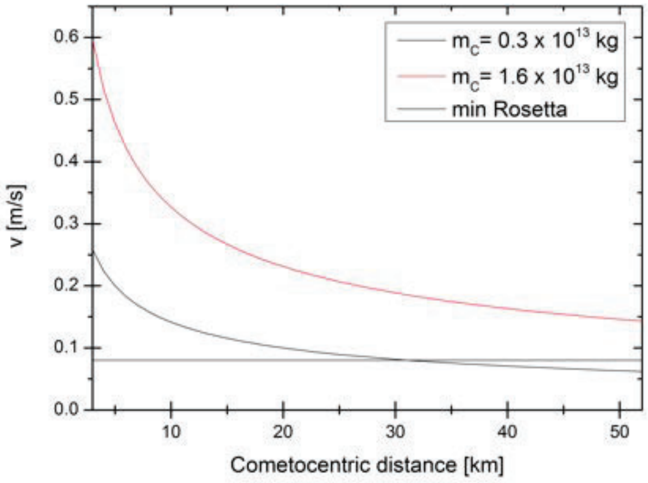

Figure 6: Kepler velocity depending on cometocentric distance and the mass of the comet.

---

[a] for one dimensional case: $|gas\ drag| = \frac{1}{2} c_d m_g n_g \sigma_{s/c} (v_{gas} - v_{s/c})^2$ with c_d: drag coefficient, m_g: mass of the gas $[kg]$, n_g: density of the gas $[particle/cm^3]$, $\sigma_{s/c}$: exposed area of the spacecraft $[m^2]$, v_{gas}: velocity of the gas $[m/s]$, and $v_{s/c}$: velocity of the spacecraft $[m/s]$.

[b] The velocity of the spacecraft relative to the velocity of the out streaming gas but since the velocity of the out streaming gas is in the order of several 100 m/s while the velocity of the spacecraft is in the order of a few m/s the latter can therefore be neglected.

comet of v_K. A possible trajectory of bound orbits is given in Fig. 7. The radiation pressure in the terminator plane is the same for every position on the orbit, the gravitational force, centrifugal force, and the gas drag should be in equilibrium. Therefore the time spent in bound orbits is highly dependent on the comet's activity and will be performed in the early phase of the mission when the gas drag is low.

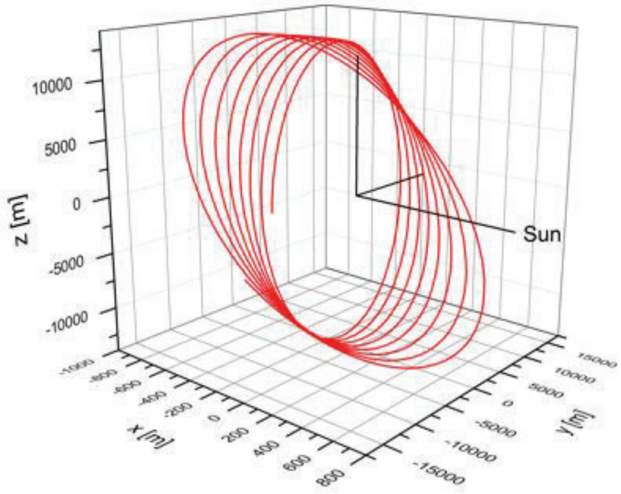

Figure 7: Bound orbit around the comet in the terminator plane. +X points from the comet's center towards the Sun, Y is in the ecliptic plane.

The flyby trajectories can further be divided into two groups: close flybys and far flybys. The flyby velocity has to be two times higher than v_K because of spacecraft safety. The reason for this is, that the spacecraft is always above the escape speed if it goes into safe mode. For close flybys the distance to the comet's center is $r > 8$km. The navigation camera must be able to see the full comet. The distance is higher for far flybys. A flyby over the sub solar point (Sun is shining on the bottom of the spacecraft, temperature sensitive!) can only be performed at Sun distances of > 2.2 AU therefore some type of flybys have to be performed before reaching this distance to gain knowledge about the most exposed area to the Sun and to get the full phase curve. However, flybys will be mainly performed while the comet is more active and bound orbits are no longer possible.

The knowledge of the exact position of the spacecraft as well as the Solar Aspect Angle (SAA) is of fundamental importance to interpret the scientific data. Spacecraft attitude and position can be accessed through NASA's SPICE toolkit.

SPICE [c] (Spacecraft, Planetary, Instruments, C-Matrix, Events) is a powerful tool offered by NASA's Navigation and Ancillary Information Facility (NAIF) for NASA flight projects and NASA funded researchers to assist scientists in planning and interpreting observations from space-based instruments aboard robotic spacecrafts. The Rosetta mission to comet 67P/Churyumov-Gerasimenko is also supported through this tool. The SPICE tool is available in different programmer languages and transforms vectors from one coordinate system into another as well as a lot of other applications, e.g. closest approach of two objects and

---

[c] for detailed documentation see: http://naif.jpl.nasa.gov/naif/index.html

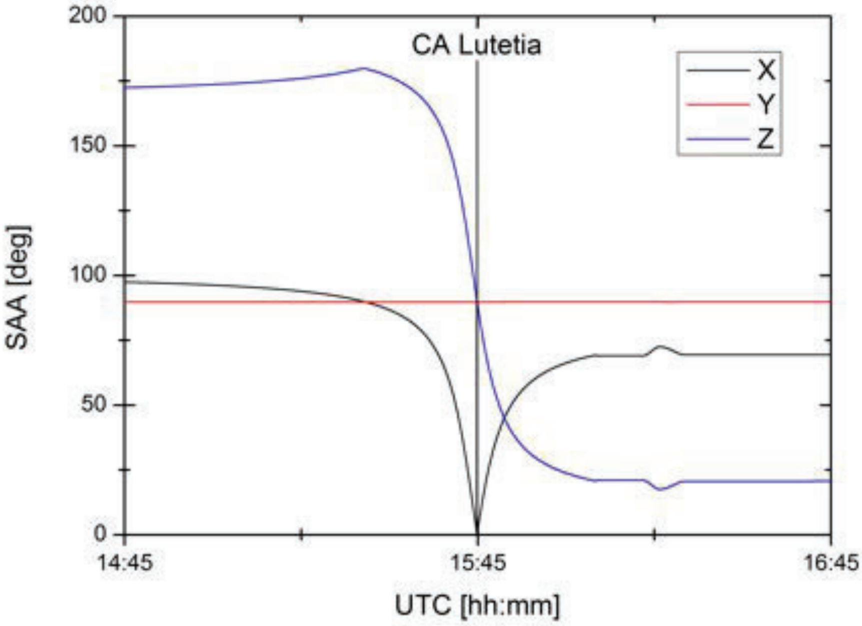

Figure 8: SAA for Rosetta during the Lutetia flyby. CA marks the closest approach of Rosetta at 15:45 UTC (2010-07-10). The angle between the +Y-axis and the Sun (Y) is nominal 90° since the solar panels are always exposed to the Sun. The angle between the +Z-axis and the Sun (Z) and X are always 180° in total.

many more. The tool comes with a set of different problems to be solved by test programs. The user is guided within documentations as well as examples. The SPICE tool can be divided into two subsections, one: the necessary kernels containing all the transformations and positions, and two: the code to extract the necessary data. The kernels contain knowledge about the coordinate system definition, data of trajectories, and time corrections. The SAA is especially important for the background problem of the gas cloud around the spacecraft [Schläppi et al., 2010] and therefore the interpretation of the data. The position of Rosetta relative to the comet is essential for the global mapping of the coma. Given as an example in Fig. 8 is the SAA during the Lutetia flyby. Documentation of the code as well as the necessary kernels are given in the App. A (SAA) and B (Trajectories).

2.2.2 Cumulative flux for different trajectories

Instruments measuring dust particles or gaseous species around the comet are especially interested in the cumulative flux along a given trajectory. To gather as much signal as possible, these instrument teams are interested in the total number of particles that enters their instrument. To deduce the flux for particles at a given location around the comet at a specific heliocentric distance there exist different approaches. The Haser model assumes spherical outgassing from the comet into the coma [Haser, 1957]. The distribution of the secondary species, produced by photodissociation of parent molecules and destroyed by photo-destruction processes, can be described by the Haser model [Combi et al., 2004].

Assuming spherical outgassing, the density around the comet depends on the production rate of the species (Q), the distance of the spacecraft to the comet (r), the gas velocity of the species (v_{gas}), and the ionization scale length (γ). The density of the parent species (n) can be calculated in the following way:

$$n(r) = \frac{Q \cdot e^{\frac{r}{\gamma}}}{4\pi \cdot r^2 \cdot v_{gas}} \tag{3}$$

With this model the distance to the comet where the density is dominated by parent species or daughter species can be deduced.

To compare the expected signal for different trajectories for in situ particle instruments, the cumulative flux has to be estimated. Neglecting the loss of parent species trough photoionization and dissociation (and $v_{s/c} \ll v_{gas}$) we can integrate Eq. 3 from closest approach to a given point in time (t_e) to obtain the total cumulative flux of all parent species:

$$\phi_{flyby} = \int_0^{t_e} \frac{Q \cdot v_{gas}}{4\pi(v_{s/c} \cdot t + r_0)^2 \cdot v_{gas}}\, dt = \frac{Q \cdot \arctan(\frac{v_{s/c} \cdot t_e}{r_0})}{4\pi \cdot r_0 \cdot v_{s/c}} \tag{4}$$

$v_{s/c}$ is the spacecraft velocity, v_{gas} the gas velocity, r_0 the minimum distance for the flyby, and t_e is approximately 3.5 days. For the full flyby the resulting cumulative flux has to be doubled (due to the symmetry the same cumulative flux arises form -3.5 days to closest approach). To scale the different integrated fluxes a time duration of 14 d per segment was taken. Over the duration of one segment two far flybys can be performed and one close flyby. The duration of a close flyby while collecting material is the same as for a far flyby but half of the segment time is used to fly back to a similar distance relative to the comet. The density of the comet at these distances is very small compared to that at the close flyby distance and therefore the additional flux collected over this time can be neglected.
The cumulative integrated flux for the segment duration of a bound orbit with the assumption of spherical symmetry of the comet's activity (Q) and the distance to the comet (r) is:

$$\Phi_{Orbit} = n \cdot v_{gas} \cdot t_e = \frac{Q \cdot v_{gas} \cdot t_e}{4\pi \cdot r^2 \cdot v_{gas}} = \frac{Q \cdot t_e}{4\pi \cdot r^2} \tag{5}$$

To calculate and compare the different fluxes collected during trajectories the total production rates for a low active comet were used (see Tab. 3).

Table 3: Total production rates for a low (LAC) and a high (HAC) active comet representing possible scenarios for 67P/Churyumov-Gerasimenko at different heliocentric distances.

Heliocentric Distance [AU]	LAC [1/s]	HAC [1/s]
1.24 (Perihelion)	4.14 x 10^{27}	1.13 x 10^{28}
2.00	4.60 x 10^{26}	2.50 x 10^{27}
3.00	3.70 x 10^{25}	5.40 x 10^{26}
3.50	2.10 x 10^{25}	3.80 x 10^{26}

Fig. 9 shows the different cumulative fluxes for representative trajectories. The bound orbits are favored for the time where the comet starts to get active because the dust and gas instruments can collect more material than during flybys. When the comet gets more active and bound orbits are no longer feasible because of the gas drag pushing the spacecraft away from the comet, flybys are performed and far flybys are favored over close flybys with a closest approach of 30 km, since two far flybys can be performed per segment as opposed to one close flyby and the dust and gas instruments can collect more material.

The cumulative fluxes increase much less (factor of six) than the activity of the comet (factor of 100 and more) because the flyby distances have to be increased for spacecraft safety and navigation due to the higher gas drag. An other restriction is the propellant available, while for bound orbits a minimal amount of propellant (Δv) is used, far flybys use more propellant depending on the flyby velocity. Close flybys are even more Δv consuming because of the higher flyby velocity: for safety reasons the spacecraft has to fly always double the Kepler velocity to avoid a collision course with the comet, even if the spacecraft goes into a safe mode. However, regardless of the trajectory the dust and gas instruments can only collect material that enters the instrument, therefore the comet should be in the field of view. Therefore the comparison presented here is based on rough assumptions but gives a good overview.

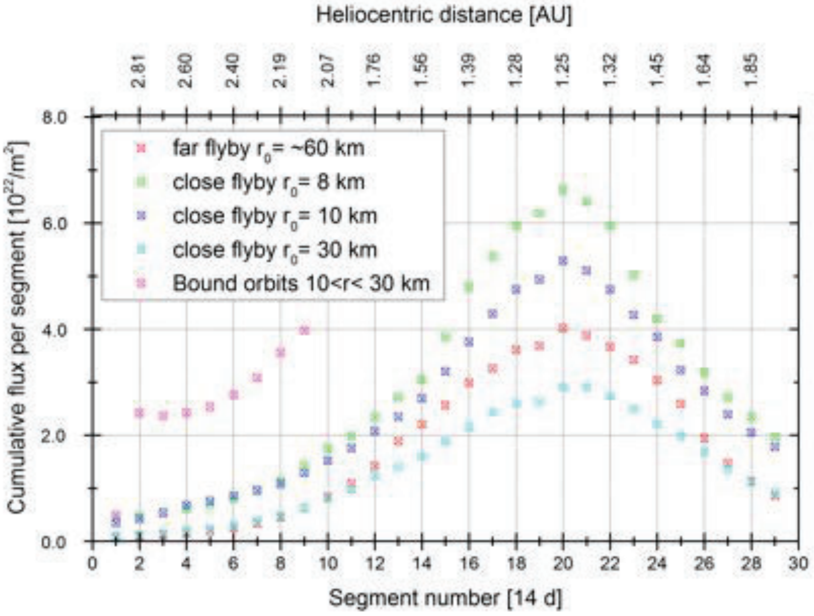

Figure 9: Cumulative flux for different trajectories depending on the activity of the comet and therefore on the heliocentric distance for a low active comet (LAC see Tab. 3).

In case of non-sperically symmetric outgassing patterns, bodies, and forces have to be taken into account, it is required to employ more complicated and higher dimensional models. Among these are fluid-type approaches [Crifo and Rodionov, 1997] or Direct Simulation Monte Carlo models [Tenishev et al., 2008, Tenishev, 2011]. Detailed results of the latter can be accessed through the ICES tool which allows access to pre-computed simulations obtained for comet 67P/Churyumov-Gerasimenko [University of Michigan, 2013].

2.3 Payload

Table 4: Rosetta Payload. Detailed description for every instrument can be found in the Rosetta book Schulz et al. (2009)

Name	**Instrument**	**Category**
ORBITER		
ALICE	UV spectroscopy	Remote sensing
CONSERT	Radio sounding, nucleus tomography	Nucleus large-scale structure
COSIMA	Dust mass spectrometer (SIMS)	Coma composition
GIADA	Dust velocity and impact momentum	Dust flux and mass distribution
MIDAS	Grain morphology with AFM	Coma composition
MIRO	Microwave spectroscopy	Remote sensing
OSIRIS	Multi-color imaging	Remote sensing
ROSINA	Neutral and ion mass spectrometry	Coma composition
RPC	Plasma Consortium	Comet plasma environment & SW interaction
RSI	Radio Science Instrument	Radio Science
SREM	Radio environment monitor	Radio Science
VIRTIS	VIS and IR mapping spectroscopy	Remote sensing
LANDER		
APXS	α-particle-X-ray spectrometer	Nucleus composition
CIVA	Panoramic camera, IR microscope	Nucleus surface structure
CONSERT	Comet nucleus sounding	Nucleus structure
COSAC	Evolved gas analyzer	Nucleus composition
MUPUS	Surface and Subsurface science	Nucleus structure
PTOLEMY	Isotopic composition sampling	Nucleus composition
ROLIS	Descent camera	Nucleus surface structure
ROMAP	Magnetometer, Plasma monitor	Nucleus structure
SD2	Sampling and distribution	Nucleus structure
SESAME	Surface investigation	Nucleus surface structure

In order to fulfill the mentioned mission objectives the Rosetta orbiter carries a set of twelve scientific instruments to the coma of the comet as well as ten scientific instruments mounted on the lander Philae to the comet's nucleus. The Rosetta orbiter is a cube shaped frame of 2.8 x 2.1 x 2.0 m^3 (Fig. 10). Most of the scientific instruments are mounted on the platform mainly pointing in the direction of the comet (+Z-direction). On both sides of the central cube (in ±Y-direction), huge solar panels of 32 m^2 each guarantee power supply of 850 W even at large heliocentric distances of 3.4 AU [Glassmeier et al., 2009]. The construction holding the solar panels as well as the central cube are mainly made from honeycomb structures. Most of the spacecraft as well as the instruments are covered in multi-layer insulation (MLI) foil, while the spacecraft is vented in the -Z-direction away from the instruments. For communication with the Earth and data delivery a controllable high gain parabolic antenna of 2.2 m diameter is mounted on the opposite side of the lander (+X-direction). The lander is mounted on the -X side of the spacecraft and therefore shielded from direct sunlight most of the time. The spacecraft is three axis stabilized and the orientation is controlled by 24 thrusters with 10 N each. The altitude of the spacecraft is controlled by a set of navigation sensors as well as four reaction wheels. The Rosetta spacecraft has a total launch mass of 2.9 t, while 1.72 t thereof is propellant. 165 kg is scientific payload and the lander weight 100 kg [Glassmeier et al., 2009]. An overview of the scientific payload of the orbiter and the lander can be found in Tab. 4 [Glassmeier et al., 2009].

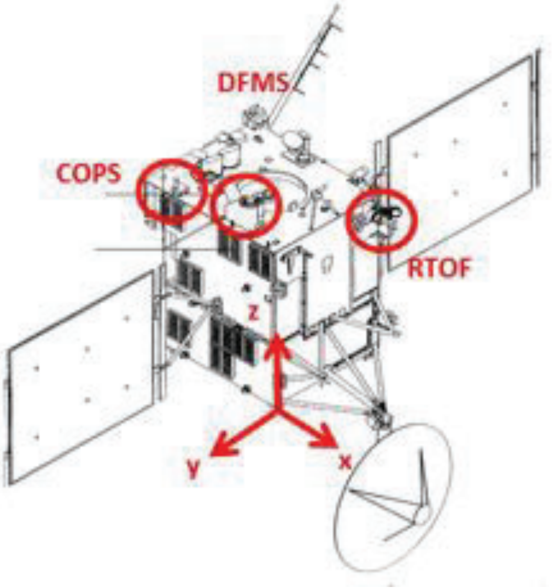

Figure 10: The orbiter of Rosetta, with the ROSINA instruments highlighted. The +Z-direction points away from the instrument platform and is supposed to point most of the time towards the comet [Schläppi et al., 2010].

2.4 ROSINA

The Rosetta Orbiter Spectrometer for Ion and Neutral Analysis (ROSINA) is an instrument package to determine the elemental, isotopic and molecular composition of the cometary atmosphere and ionosphere and the physical properties (temperature, velocity) of the neutral and ionized components in the coma of comet 67P/Churyumov-Gerasimenko. The measurements of the isotopic composition in the volatile light elements (C, H, O, and N) in the cometary coma are difficult, because low abundance isotopes of these elements, (e.g. D, ^{13}C, ^{17}O, ^{18}O, ^{15}N) are within a very close mass range of very abundant isobaric hybrides (H_2, ^{12}CH, ^{16}OH, $H_2^{16}O$, ^{14}NH) and a mass resolution $m/\Delta m$ of up to 3000 at 1% peak hight is needed to separate e.g. ^{13}C from CH. The $^{13}C/^{12}C$ ratio is key for nearly every solar system model. To accomplish these objectives, ROSINA (for detailed description see Balsiger et al. (2007)), consisting of two mass spectrometers and a pressure sensor will fullfill this task due to its unprecedented capabilities for space borne mass spectrometers:

- mass range of 1 u/e to > 300 u/e to detect simple atoms as well as heavy organic molecules
- very high mass resolution of $m/\Delta m = \sim$3000 at 1 % peak height to resolve e.g. $^{12}C^{16}O$ from $^{14}N_2$ and ^{13}C from ^{12}CH
- wide dynamic range of up to 10^{10} and very high sensitivity of $> 10^{-5}$ A/mbar

The strategy to fly two mass spectrometers and a pressure sensor in a package has not only technical advantages, but with regard to the long mission duration also provides redundancy. The three sensors are commanded and controlled by the Digital Processing Unit (DPU). The ROSINA sensor package is in total 1/5 of the mass of the total payload weight of the orbiter.

Since the launch of Rosetta was postponed, the flight models of ROSINA could be replaced by the flight spare models. The advantage of this was, that the later built models could be flown. During building of the instruments one gains more knowledge about the process and the later build instruments are usually in a better condition than the first version. Therefore the model used in the lab is the original Flight Model (FM) while the original Flight Spare (FS) is on Rosetta.

2.4.1 COPS

The COmetary Pressure Sensor (COPS) is designed to measure the neutral gas parameters (density and velocity) around the comet. It consists of two gauges (see Fig. 11): the nude gauge and the ram gauge. The nude gauge is designed to measure the total neutral gas density, while the ram gauge measures the molecular flow. The combination of both measurements provides knowledge about the total particle density and the gas velocity of the cometary volatiles. COPS is not only a scientific instrument but serves also as safety for the two mass spectrometers as well as other instruments, where an increase in pressure (e.g. $> 10^{-6}\ mbar$) can cause damage through high voltage discharges and thus have to be switched off.

The nude gauge is technically build in a Bayard-Alpert design, where neutrals are ionized trough electron impact ionization. The ions are then accelerated towards a cathode for collection and the resulting current is measured by a sensitive electrometer. The cathode is made of a thin molybdenum wire and the measured current of the electrometer is directly proportional to the total neutral particle density, the proportionality however is species dependent.

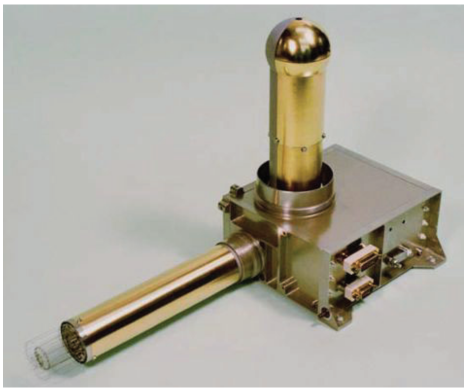

Figure 11: COmetary Pressure Sensor (COPS). Image credit: Balsiger et al. (2007)

The ram gauge measurement principle is similar to the nude gage. The neutral gas is thermalized within an equilibrium chamber in front of the ionization volume. This measurement is very temperature sensitive and therefore microtip field emitters are used instead of the hot cathode of the nude gauge. The gauges are mounted on booms in order to minimize interference with the spacecraft. The COPS sensor then is mounted on the instrument platform while the nude gauge exceeds the instrument platform and the ram gauge points in the direction of +Z. The nude gauge has a field of view of roughly 4π (excluding the direction of the boom). The ram gauge measures a ram pressure in +Z direction (dynamic pressure), and with the difference in dynamic and static (nude gauge) pressure the gas velocity can be derived.

2.4.2 RTOF

The Reflectron-Time-of-Flight mass spectrometer (RTOF) is one of the mass spectrometers of ROSINA (see Fig. 12). All TOF instruments are based on the same principle: All particles start at the same time (pulse), are accelerated to the same energy, fly along a potential free drift path, and are then detected time dependent at the detector. Because all the particles undergo the same acceleration potential and therefore have the same energy, heavier ions (larger mass to charge (m/q) ratio) are slower than lighter ions resulting in a longer time of flight of a given distance. The instrument performance is manly dependent on the fast electronics of the detector. To further enhance the resolution of the instrument, the time between the particles has to be increased, this is achieved by a longer flight distance. The flight time is directly proportional to the flight distance (for a constant velocity) and therefore a longer flight distance results in a higher resolution. This can be achieved with a fold of the trajectory using reflectrons as done for RTOF. RTOF covers a mass range of 1 u/e to >300 u/e and has a high sensitivity. RTOF can record a spectrum of the entire mass range almost simultaneously and within the nominal integration time of 200 s.

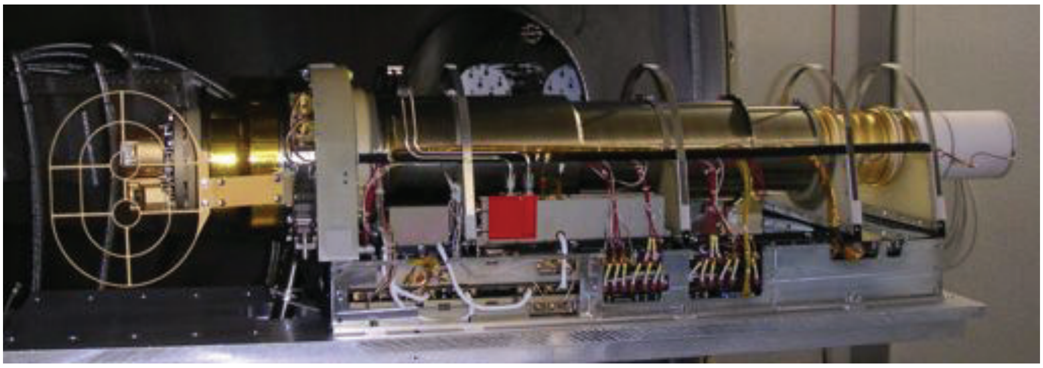

Figure 12: Reflectron-type Time of Flight mass spectrometer (RTOF)

2.4.3 DFMS

The Double Focusing Mass Spectrometer (DFMS) is the main subject of this work and a detailed description can be found in Chapter 3. RTOF and DFMS are designed to provide redundancy and both instruments together fulfill the primary objectives of ROSINA. While RTOF has a larger mass range (1 u/e – 300 u/e), DFMS complements it with the required mass resolution of $m/\Delta m = \sim 3000$ at 1% peak height.

2.4.4 DPU

The Digital Processing Unit (DPU) is the control unit of the three ROSINA sensors (see Fig. 13). It commands the measurement modes for each instrument and handles the science data. Furthermore it is the interface between the spacecraft and ROSINA.

The principal drivers of the DPU design: optimum use of the allocated telemetry rate, single-failure tolerance for all functions serving more than one sensor, and the independence of availability of radiation hardened parts. The primary data rate during full operation of all three sensors exceeds the maximum telemetry rate of the spacecraft by magnitudes.

Reducing the amount of scientific data is therefore a fundamental need. A compression of the data can be done in two levels, one in the sensor electronics itself and second in the subsequent software processing by spectrum windowing or averaging, either in lossless or lossy fashion. The lossy compression can cause degradation in mass resolution and/or time resolution but on the other hand is more powerful in deducing the file size (and thus telemetry) of the obtained science spectra.

Figure 13: Digital Processing Unit (DPU). Image credit: Balsiger et al. (2007)

3 DFMS instrument description

DFMS is a double focusing mass spectrometer with an unprecedented high mass resolution of $m/\Delta m$ ~3000 at 1% peak height for (*in situ*) space science [Balsiger et al., 2007]. It can measure ion and neutral densities of 1 cm^{-3} and has a dynamic range of $\sim 10^{10}$. The sensor can be divided into two parts: the instrument and the electronics box. The electronics box is a compact part located under the instrument which is directly attached to the spacecraft. The whole sensor except the ion source is covered in Multi Layer Insulation (MLI). The MLI is designed to passively control the thermal behavior of DFMS. The nominal temperature range for DFMS to be operated is between -20 °C and +50 °C [Zahnd, 2002]. The MLI can help to heat the instrument into the operation range, since the temperature at the beginning of the mission is expected to be lower. The instrument itself has also heaters for example in the RDP-electronics to heat the MCP/LEDA. The MLI shields the ions to be measured by the instrument from the electric and magnetic fields of DFMS. The sensor is located on the instrument platform of Rosetta, with the field of view (FOV) of the instrument aligned perpendicular to the instrument platform and pointing away from the spacecraft (+Z direction). The instrument platform of Rosetta is intended to point towards the comet.
A sealed cover over the entrance of the instrument protects it during mounting on the spacecraft as well as avoiding contamination from Earth. The seal of the cover is broken open after launch and the cover mechanism can move the cover away from the entrance. The cover is mostly open during flight for safety reasons.
A particle (ion or neutral) undergoes the following sections in DFMS: Ion source, transfer optics, analyzer sections, zoom optics and finally ends up in one of the three detectors.

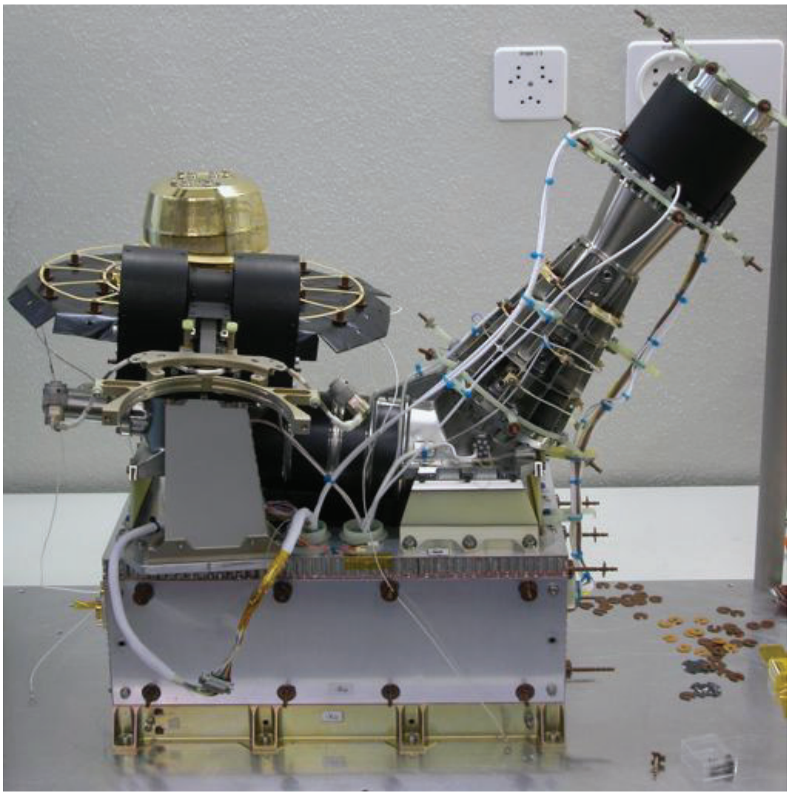

Figure 14: DFMS FM

In the ion source neutrals are ionized by electron bombardment, while for external generated ions the source works as attractor for these ions. After this, ions (as well as the former neutrals) are extracted to the analyzer section through the transfer optics. Depending on the resolution mode of the spectrum the ions are focused on one of two slits in front of the analyzer section. For high resolution (HR) the slit is narrower than for low resolution (LR). The analyzer section of DFMS is designed according to the Nier-Johnson geometry [Johnson and Nier, 1953] in which a deflection of 90° in a radial electrostatic field analyzer (ESA) is followed by a magnetic deflection of 60°. Such a geometry leads to a compensation of the energy dispersion between electrostatic and magnetic fields, which results in an energy and direction focusing. After the analyzer section, only ions with the right mass to charge ratio (m/q) reach the zoom optics. In this section the focal point on the focal plane can be adjusted by a hexapole or the image scale can be increased by a combination of two quadrupoles. Finally the ions are detected by the main detector, a combination of a Micro Channel Plate and a Linear Detector Array (MCP/LEDA) or on one of the two additional detectors, the Channel Electron Multiplier (CEM) or the Faraday Cup (FC).

3.1 Ion source

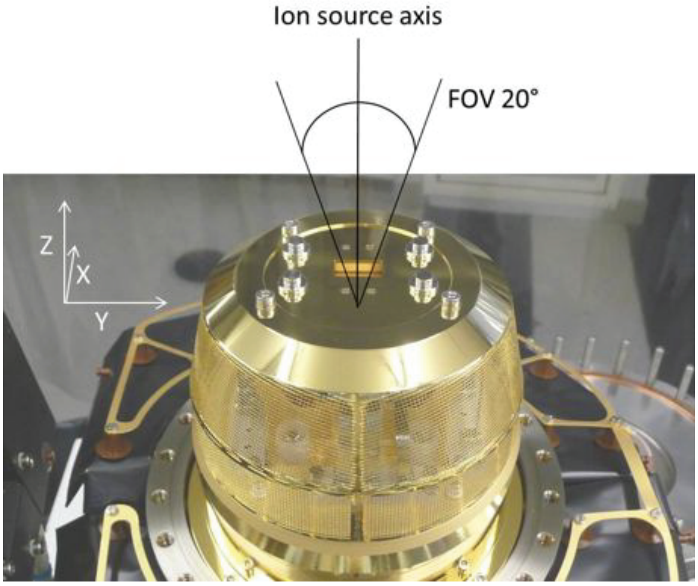

Figure 15: Picture of DFMS ion source with the ion source axis and the main FOV of 20° x 20°. For a better understanding of the position of the FOV the axis of the spacecraft frame are added.

The ion source has a main FOV of 20° x 20° and is centered in the ion source axis which lies parallel to +Z, while the narrow angle FOV (2° x 2°) is perpendicular to the source axis and parallel to the +X, see Fig. 15. The ion source can be operated in one of two modes: the neutral mode or the ion mode. An overview of the ion source potentials and the electrodes can be found in Fig. 16. In the neutral mode neutrals are ionized by electron impact ionization. While externally formed ions are efficiently prevented from entering the ion source by floating the ion source on a positive potential of +200 V on the ion source box potential (ISB) (see Tab. 5).

Table 5: Ion source potentials of DFMS

Electrode	Description	Reference potential
ISB	Ion Source Box	S/C
ISP	Ion Suppressor	ISB
IRP1	Ion Repeller 1	ISB
IRP2	Ion Repeller 2	ISB
SLL	Source Lens Left	ISB
SLR	Source Lens Right	ISB
BD	Beta Detection	ISB
SES	Source Exit Slit	ISB

The electron beam is perpendicular to the ion source axis and generated by one of two filaments by thermionic emission. A weak magnetic field of 200 G guides the electrons. The emission of the filament can be regulated to 2 μm, 20 μm and 200 μm while the not emitting filament serves as trap to monitor the emission current. Both filaments can be used as emitting filaments for redundancy. The electron energy can be varied between 10–90 eV to benefit from a suppression of fragmentation or multiple ionization for lower energies and to maximize the ionization cross section for higher energies. However, the nominal electron energy is now set to 45 eV after the work of Schläppi (2011), because a decreasing of the signal for higher electron energies was detected. To achieve this electron energy of 45 eV with the emitting filament 1 the following setting of potentials is required:

Table 6: Filament potentials of DFMS for filament 1 as emitting filament

Electrode	Description	Reference potential	Setting [V]
Fil1bias	Fil 1 Bias, Trap	ISB	-45
Fil2bias	Fil 2 Trap, Bias	ISB	+50
ERP	Electron Repeller	ISB	-50

The ERP located behind the filament is set 5 V more negative to push the electrons towards the ionization region and the filament 2 serving as trap for the electrons. The reduction of the electron energy from 70 eV to 45 eV might have a major influence on the multiple ionization as well as the fragmentation behavior of molecules. After the ionization of the neutrals in the ion source box, the ions are extracted by the source lenses (SLL and SLR) through the ionization box exit slit. The source lenses allow a deflection of the ion beam in the plane of the ion trajectories. While in the perpendicular direction the beta deflection potential (BD) inside the beta deflection housing can be used to deflect the ion beam. Then the ions are accelerated towards the source exit slit with a potential of -1 kV relative to ISB (SES = -1 kV).

In the ion mode ISP, IRP2 and IRP1 are used to attract ions that are externally formed and focus them in the ionization region. In addition, the coarse mesh grid (MG) surrounding the ion source can be used to enlarge the influence of DFMS on the electrical field configuration. Since the spacecraft could be positively charged, the mesh grid can help to suppress the positive potential. The filament can be switched off or in sub emission, where the filament is heated but not emitting. After this the ions are focused on the SES by adapting the source lens potential (SLL + SLR).

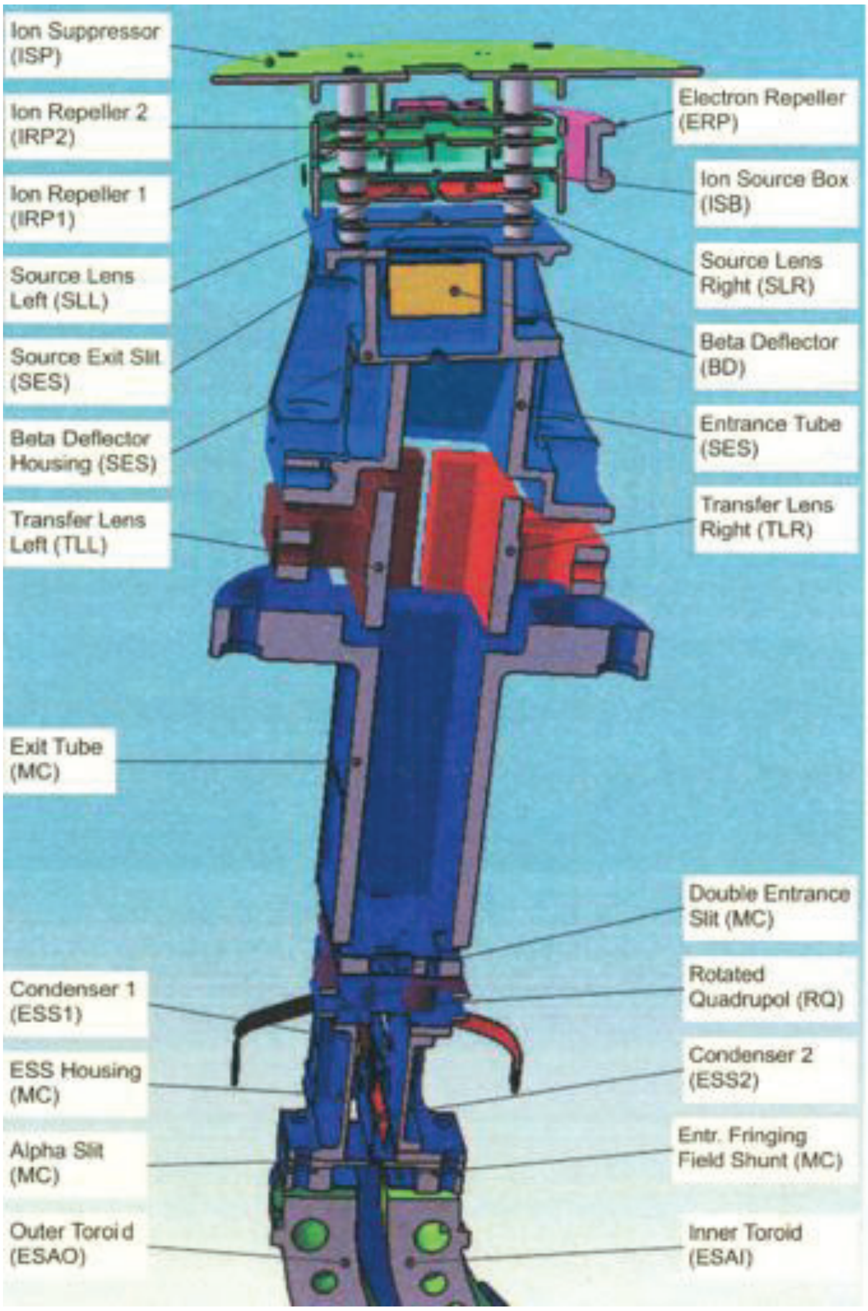

Figure 16: DFMS ion source and transfer optics with the potentials. The influence of the electrodes on the ion optical path can be found in the text.

3.2 Transfer optics

The transfer optics section fulfills two different tasks simultaneously: the further acceleration of the ions as well as focusing of the ion beam on one of the two resolution selective slits. The additional acceleration voltage depends on the measurement mode. In the neutral mode, formal ions undergo the acceleration voltage V_{accel}. V_{accel} depends on the m/q ratio of the species and physical properties of the magnet e. g. the radius r_B of the sector magnet and the magnetic field B. For derivation see Sec. 3.4:

$$V_{accel} = \frac{1}{2}\frac{q}{m}r_B^2 B^2 \tag{6}$$

In the ion mode, the initial kinetic energy of ions entering the magnet section has to be taken into account for further acceleration. Therefore the V_{accel} voltage is corrected since ions and former neutrals passing trough the magnet section should ideally impinge on the same position of the detector [Schläppi, 2011]. Therefore the acceleration in the ion mode V^*_{accel} is different from V_{accel} in the neutral mode. The difference depends on the initial energy of the ions T_{ion}/q:

$$V^*_{accel} = V_{accel} + T_{ion}/q \tag{7}$$

With the adaption of V^*_{accel} the ions and former neutrals have the same kinetic energy. Therefor all other voltages of the DFMS analyzer (ESA, magnet, zoom optics, detector) have to be set exactly the same way for ion and neutral mode.

The focusing on one of the two resolution dependent slits is achieved with an assembly of two deflection plates called the transfer lens (TLL + TLR). For high resolution (HR) mode the slit width is 14 μm while for low resolution (LR) mode it is 200 μm. The optical axis of the transfer optics is tilted by 6° relative to the axis of the ion source to prevent cometary dust entering the analyzer section. After the two slits a rotational quadrupole (RQ) assembly can be used to correct miss-alignments of the ion beam. The ion beam then enters the slit switch region, where the ion beam is guided on to the alpha slit in front of the ESA. Ions passing the high resolution slit are not influenced by this region since the ion optical axis of the transfer optics is aligned with the alpha slit. In contrary the ions passing the low resolution slit are guided back on the alpha slit within the slit switch region (ESS1 + ESS2).

3.3 Electrostatic analyzer (ESA)

In the ESA section the ion population is focused in energy and angle. Ions of the same energy entering the ESA at the same point but with different entering angles, are focused on the same image point at a specific distance from the ESA exit. Simultaneously ions with the same entrance angle, but different energies, are spatially separated because of the different diffraction radii they describe in the electrostatic field. A detailed mathematical description and simulations of the ESA can be found in Wüthrich (2007). The ESA consists of two deflection plates of toroidal shape. The deflection plates have two different radii in the plane of the DFMS cross section; the inner one has a radius of 57.5 mm while the outer one has a radius of 62.5 mm. The electrostatic section is completed with a pair of Matsuda Plates (MP) to close off the ESA and are used to optimize the image point. To guarantee an exact deflection of 90° and to terminate the influence of the electrostatic field on both sides of the ESA, fringing field shunts are located at entrance and exit of the ESA. 19.5 mm after the ESA an energy slit limits the passage of ions with an energy deviation of more than ± 1% of the selected ion energy. An ion of mass (m), charge (q) and velocity (v) passing the

ESA on the middle equipotential surface is forced to fly on a circular arc of similar curvature as the ion optical element. Therefore, the centrifugal force F_{cf} and the electrostatic force F_{esa} acting on this ion have to compensate each other. F_{cf} is dependent on m, v and is inversely proportional to the radius of the ion flying through the ESA (r_{esa}). The radius of the middle equipotential surface of the ESA is r_{esa} = 60 mm. While F_{esa} depends on q and the electrostatic field E_{esa} applied over the ESA

$$F_{esa} = qE_{esa} = \frac{mv^2}{r_{esa}} = F_{cf} \tag{8}$$

The kinetic energy of the ions $\frac{mv^2}{2}$ can be expressed by the acceleration energy qV_{accel}, since the ion velocity is much lower than the speed of light in vacuum.

$$E_{esa} = \frac{2V_{accel}}{r_{esa}} \tag{9}$$

The potential difference across the ESA deflection plates ($\frac{\Delta U_{esa}}{d} = E_{esa}$) can be determined according to equation (9) and the geometrical information of the distance between the plates (d = 5 mm) as following:

$$\Delta U_{esa} = \frac{1}{6} V_{accel} \tag{10}$$

3.4 Magnet

After the ESA section ions go to the magnet section. The magnetic analyzer is located 99.5 mm after the energy slit of the ESA and separates the ions in momentum space. The magnetic analyzer is a 60° sector magnet consisting of two permanent magnets with a medial radius r_B of 10 cm. The permanent magnets are made of Salarium-Cobalt (Sm-Co) alloy while the yokes and pole pieces are made of Iron-Cobalt (Fe-Co) alloy. The sector borders of the magnet are titled 5° with respect to the perpendicular of the ion optical axis. The magnetic field (B) is temperature (T) and sensor (FM, FS) dependent:

$$B_{FM}(T_{mag}) = 0.3563[T] - 1.2969 \cdot 10^{-4} \left[\frac{T}{^\circ C}\right] (T_{mag}[^\circ C] - T_0[^\circ C]) \tag{11}$$

$$B_{FS}(T_{mag}) = 0.3550[T] - 1.7262 \cdot 10^{-4} \left[\frac{T}{^\circ C}\right] (T_{mag}[^\circ C] - T_0[^\circ C]) \tag{12}$$

The coefficients have been calculated for the reference Temperature T_0 = -22 °C. At room temperature (T_{mag} = 20 °C) the magnetic field of the FM is B_{FM}= 0.3617 T while for the FS it is B_{FM} = 0.3623 T. Differences in the ion optical setting of the magnetic analyzer between FM and FS are due to the different magnetic fields as well as possible geometrical differences due to manufacturing tolerances. Ions leaving the ESA section are spatially separated by energy and by entering the magnet analyzer undergo the Lorentz force F_l and describe a circle according to their momentum. In the magnet analyzer the centrifugal force F_{cf} and F_l are in equilibrium. F_l depends on the charge q, the velocity v of the ion and the magnetic field B.

$$F_l = qvB = \frac{mv^2}{r} = F_{cf} \tag{13}$$

Solving this equation for the refraction radius r and replacing the velocity according to $v = \sqrt{\frac{2qV_{accel}}{m}}$ (kinetic energy = acceleration energy), leads to:

$$r = \sqrt{\frac{2mV_{accel}}{qB}} \tag{14}$$

This equation shows that only ions with the right mass to charge ratio will pass the magnet according to $r = r_B$. To measure ions of a specific mass to charge ratio V_{accel} is set to the corresponding potential. All others will describe a different radius r and hit the hardware of the magnet. Note that equation (14) and (6) are the same if the refraction radius r is equal to the medial radius r_B of the magnet.

3.5 Zoom optics

Ions leaving the magnet section enter the zoom optics. A hexapole (HP) after the magnet is used to adjust the alignment of the focal plane relative to the ion optical axis. The nominal angle between focal plane and ion optical axis is 28.3°. The following zoom optics (also referred to as zoom system) consist of two consecutive quadrupoles and is capable of increasing the image scale at the detector by a factor of 5–7 resulting in an increase of the resolution of $\sim 20\%$. The zoom optics can only be used for ion beams close to the ion optical axis. Therefore the use of the optical zoom is limited to the position sensitive MCP/LEDA detector, which lies in the ion optical axis.

3.6 Detector package

The DFMS detector package consists of three detectors: A position sensitive MCP in combination with the LEDA, CEM and FC. All three detectors are aligned in the focal plane. The MCP/LEDA is the main detector and is positioned in the middle of the detector package along the nominal ion optical axis. The CEM is located on the left hand side of the MCP/LEDA, while the FC is located on the right hand side (see Fig. 17). The diffraction radius of the ion flight path in the magnet with a shift in V_{accel} is adapted to guide ions of similar m/q onto the two other detectors. If an ion with a specific m/q is measured with the MCP/LEDA slightly heavier ions impinge more to the right in Fig. 17 and ions with a lower m/q are detected more to the left. With the same V_{accel}, ions with a lower m/q ratio impinge on the side of the CEM while heavier ions impinge on the side of the FC. V_{accel} is limited to -6500 V, therefore 12 u/e can only be detected with the CEM. To detect e.g 18 u/e with the MCP/LEDA, 18 is commanded as central mass m_0 and the required V_{accel} applied. A spectrum of the total mass range consists of several individual spectra, depending on the resolution mode. The mass range per spectrum covered in HR is much smaller than in LR. Two spectra of a mass scan in HR do not necessarily overlap since m_0 are integer masses, and the covered mass range for $m_0 = 13$ is ±0.1 and for $m_0 = 100$ is ±0.8. For LR the covered mass range for $m_0 = 13$ is ±0.65 and for $m_0 = 100$ is ±5.0.

3.6.1 MCP/LEDA

The main detector of DFMS is a position sensitive imaging detector located a the intercept of the focal plane and the nominal ion optical axis. It consists of two micro channel plates in Chevron configuration with a thickness off 0.33 mm [Balsiger et al., 2007] and a pore diameter of 6 μm, while the tubes are inclined to 13° with respect to the ion optical axis. The amount of secondary electrons released by an ion that impinges on the MCP is dependent on the energy of the ion, the species and the MCP performance. To increase the detection

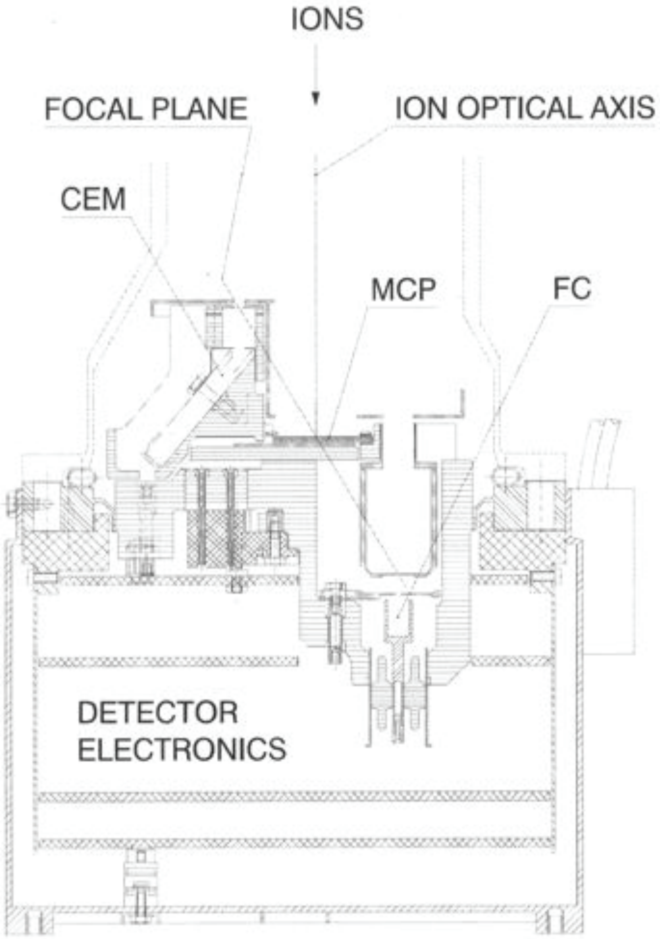

Figure 17: DFMS detector with focal plane of the analyzer and the ion optical axis. The position sensitive MCP is in the center of the detector package and aligend with the ion optical axis. The CEM and FC detectors are located at the end of the focal plane. Figure taken from [Balsiger et al., 2007].

of heavy ions (low V_{accel}) a post-acceleration voltage (PA) can be applied on the front of the MCP (up to -3 kV) to increase the energy of the ions. The unsymmetrical structure of the detector head, in particular around the MCP, where the PA is applied causes a significant restriction of the mass resolution. This effect is well understood and documented in Wüthrich (2007) and Riesen (2007). A PA of -1 kV is nominally applied in HR modes and for commanded masses ≥ 70.

Between the MCP front and back a variable voltage can be applied to determine the gain of the detector (MCP_{gain}). An ion that impinges on the MCP front, releases secondary electrons, that are accelerated towards the MCP back (nominal -200 V) . The released secondary electrons then knock out other electrons as soon as they hit the side walls of the tubes, causing a cascade of electrons. The generated electron-cloud is detected by two independent rows of 512 anodes called Linear Electron Detection Arrays (LEDA). Each LEDA anode is 22 μm x 8 mm in size and the gap between two anodes is 3 μm. The DFMS MCP detector is operated in analog-mode and not in counting mode. This has the advantage that during the recording of one mass spectrum, the amplification of the MCP can be varied over a wide range (from $10^0 - 10^6$ electrons per impinging ion). The range of possible amplifications of the detector transfers directly into the dynamic range of the sensor itself. An other advantage is the detection frequency of the MCP/LEDA, which is much higher than for the other two detectors. An example of two spectra of the same commanded mass in LR and HR can be found in Fig. 18.

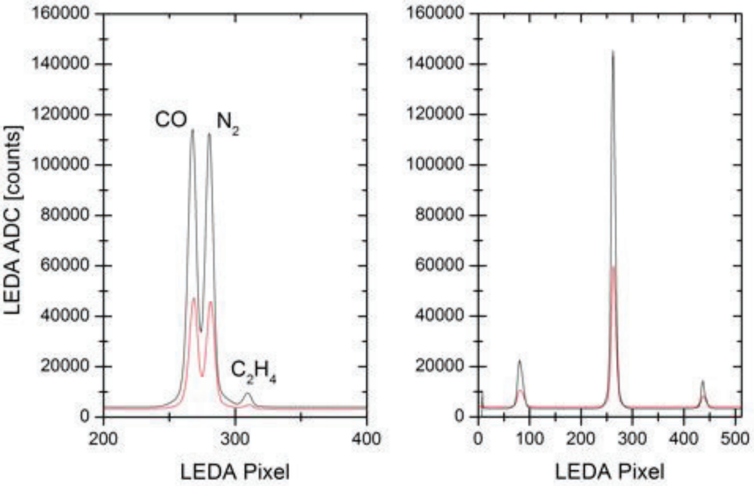

Figure 18: DFMS FM spectrum of 28 u/e with the MCP/LEDA in HR and LR. These spectra are recorded with an emission of 200 μA and an integration time of 19.8 s. The black line is recorded with rowA of the LEDA and the red line with rowB. In HR N_2 is clearly separated from CO and C_2H_4. In LR CO, N_2 and C_2H_4 overlap but 27 u/e and 29 u/e are visible.

3.6.2 CEM

The second detector is a Channel Electron Multiplier (CEM). In front of the detector (~ 1 cm) a slit of 25 μm is located to ensure that high resolution spectra can be obtained. The standard operation of the CEM is performed in counting mode with a potential of -2337 V over the CEM but can also be operated in analog mode. To record a CEM spectra the ion beam is shifted over the entrance slit of the CEM in little mass steps. The shift parameter is resolution and mass dependent (LR: $\Delta m = \frac{m}{10^3}$ and HR: $\Delta m = \frac{m}{10^4}$). This shift parameter is used since software version V6.A, before the step sizes were a factor of 4 smaller. The number of steps for one spectra is also mass and resolution dependent, while for LR the number of steps is $\sim \frac{140}{\sqrt{m}} + 1$ and for HR the number of steps is $\sim \frac{240}{\sqrt{m}} + 1$. This numbers are implemented in the software since version V7.AE, before the number of steps was one step smaller. The shifting of the ion beam over the entrance slit of the CEM is nominal done with a change in V_{accel} but can also be performed by applying different electric fields over the ESA. The integration time of one spectrum is the integration time of one step (nominal 1000 ms) multiplied by the number of steps. The CEM is therefore much more time consuming than the MCP/LEDA detector but has the advantage that the signal on the detector is not species dependent nor degrading over time as the MCP. An example of two spectra of the

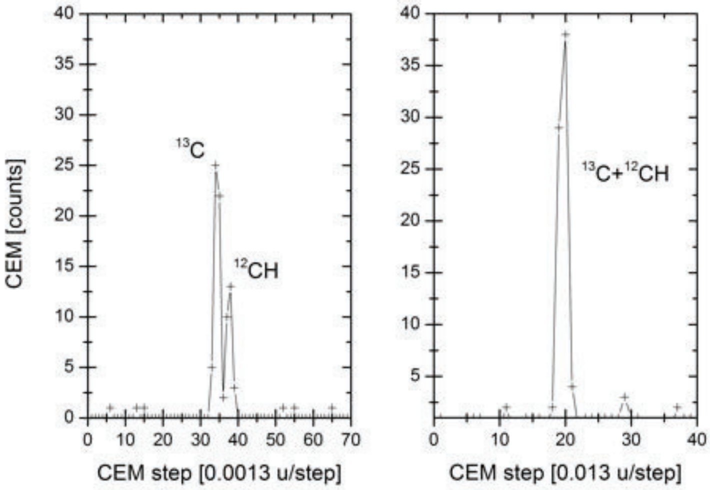

Figure 19: DFMS FM CEM scan of 13 u/e. Theses spectra are recorded with an emission of 20 μA and an integration time of 1000 ms per step while CO_2 was introduced into the chamber. In HR ^{13}C and ^{12}CH are clearly separated.

same commanded mass in LR and HR can be found in Fig. 19.

3.6.3 FC

The third of the three detectors is a Faraday Cup (FC) that measures directly the ion current with an electrometer. A wide slit of 0.35 mm is located in front of the cup. A mass spectra is recorded by shifting the ion beam over the entrance slit with a step with of $\Delta m = \frac{m}{2000}$ independent of the resolution mode. The detector can measure currents in the range of 10^{-14} – 10^{-8} A and is therefore not used for low intensity measurements. However, its simplicity guarantees internal calibrations of the other detector as well as long time stability measurements. An example of two spectra of the same commanded mass in LR and HR can be found in Fig. 20.

3.7 GCU

The Gas Calibration Unit (GCU) of DFMS contains a gas mixture of CO_2, Ne, and Xe. Two gas containers are attached outside of DFMS on the electronic box and gas tubes introduce the gas directly into the ion source of DFMS. For redundancy the GCU has two independent gas tanks and tubes to introduce the gas into the ion source. To introduce the gas into the source a tube with a ball inside is heated in an on off fashion. When the tube is heated it expands while gas can pass between the wall of the tube and the ball and enter the ion source. The GCU is used for the calibration of the mass scale for the MCP/LEDA and to adjust the CEM stepping center mass. The mass range of a CEM spectra is rather small, therefore the peak shift is adjusted to have the highest signal in the middle of the steps.

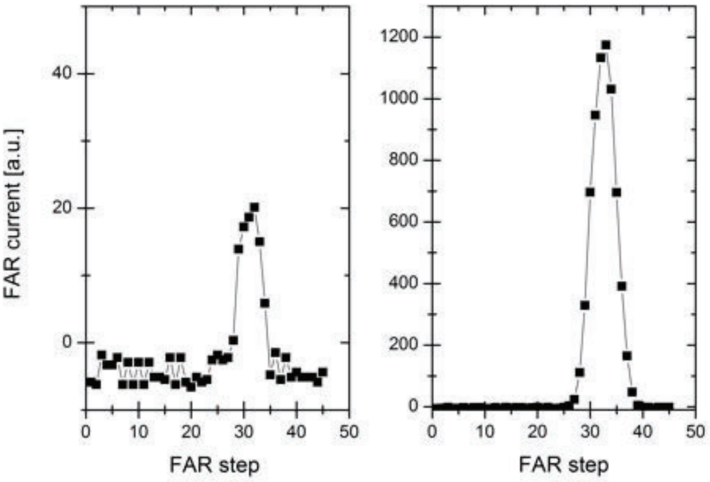

Figure 20: DFMS FM Faraday cup scan of 28 u/e for HR (left) and LR. The step width for both scans was 0.014 u/step. The emission was 200 μA and the integration time 1000 ms per step.

3.8 DFMS operation

There exist rather large differences in the operation of DFMS FM and FS. The ground support equipment (GSE) for DFMS FM consists of a power supply simulating the 28 V spacecraft bus and an ordinary computer with a special operating system (GSEOS). GSEOS simulates the interaction between the operation center, the spacecraft and the DPU. To operate the instrument and detect ions on the detectors, many different voltages have to be adjusted and applied. The ion source voltages are set measurement mode dependent. To measure ions the voltage set is different from the one used for neutrals. The voltage set for ions and neutrals are stored in a table named 'Rositabs' in the DPU memory. Other voltages are resolution and mass dependent e.g. the slit region (ESS1 + ESS2) or the zoom voltages (ZQ1 and ZQ2). The voltages of the analyzer section are mass dependent (ESAI, ESAO, and V_{accel}). The mass dependent voltages are calculated according to the mass that is to be analyzed. The detector region has an other set of voltages that are signal dependent, like the gain of the MCP (MCP_{Front}). The gain is adapted automatically by an algorithm to adjust the signal on the LEDA. This gain adjust can be toggled on or off manually for the FM. All the voltage ranges are controlled by the DPU and error messages are implemented if the set voltage is not in the safety range. For DFMS FM all this voltages can be adapted manually or a spectrum of a certain mass (commanded mass) can be recorded, while the voltages are set automatically. To reduce the commanding the DPU provides measurement modes to command all this voltages automatically. The DFMS FS is mainly commanded in this way for obvious reasons as the signal travel time or the workload during commissioning. Modes have the advantage that measurement sequences can be performed according to the science questions to tackle or instrument calibrations. The modes can cover a mass range by commanding the masses according to the signal mass range on the detector. This mass range is then covered within a mode and contains several spectra. An other possibility is to record only specific masses in a mode, if one is interested in noble gases it is less time consuming to record spectra only of masses that are interesting (e.g. m/q 20, 40, 84, 132). The calibration modes with the GCU, are recorded in a similar fashion. Sets of modes can be combined in sequences to simplify the planning of the operations.

3.9 Technical problems

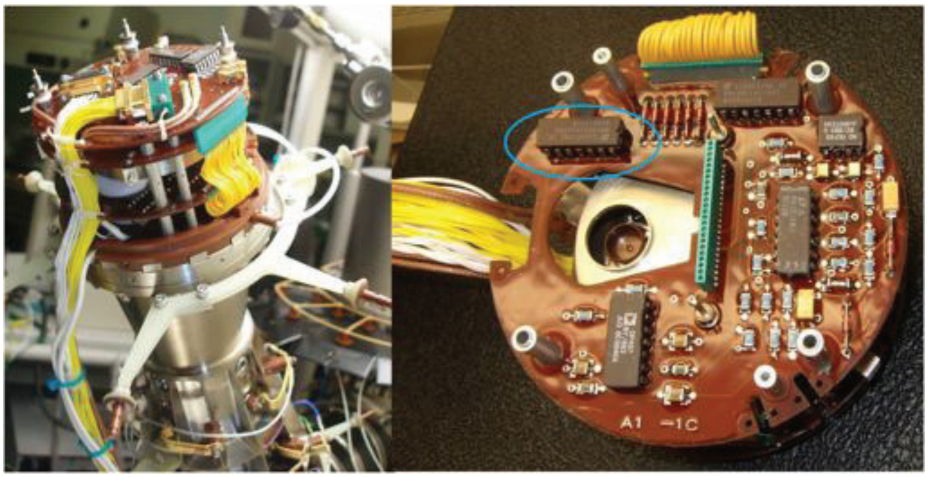

Figure 21: Remote Detector Package (RDP): on the left side from top to bottom RDP-CON, RDP-FEM, RDP-DVI and RDP-FLI. On the right side the defect an later replaced inverter on the bottom side of the RDP-DVI board.

The detector package of DFMS is described in Sec. 3.6. Behind the detector package the Remote Detector electronics Pack (RDP) is located (for detailed documentation see Neefs et al. (2004)). The Remote Detector Package (RDP) consists of four boards (from the detector package upwards): RDP-FLI, RDP-DVI, RDP-FEM and RDP-CON.
After an arcing of the V_{accel}, the MCP/LEDA rowB showed an unexpected behavior. Three effects are detectable (see Fig. 22): a drop in counts, a plateau and a 'memory' effect. The drop in counts is in the first ∼20 pixels. The plateau starting at a random pixel covers parts of rowB. The 'memory' effect, shows some signal on the same pixels as the peak of the previous taken spectrum.
Several tests were performed in collaboration with BIRA and a possible damage of the LEDA or parts behind was localized. After the replacement of the LEDA, the three effects were still detectable. By further inspection of the RDP electronics a tattered inverter on the RDP-FLI was found and replaced. After this only the plateau effect is still randomly detected and might be due to a timing problem during the switch on of the MCP.
The new LEDA has a depleted signal on pixel 8 of rowB and an inflated signal on pixel 9. The same effect is seen on rowA for pixel 429 (inflated) and 430 (depleted). The effect must be taken in to account for the pixel gain evaluation.
The V_{accel} for DFMS FM and FS, was then limited to -6500 V, to avoid other technical problems.

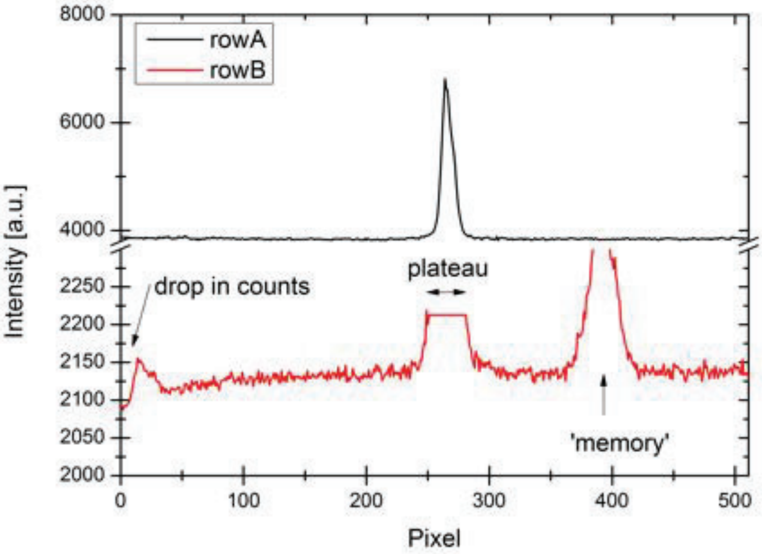

Figure 22: The three effects observed for rowB of LEDA for FM. The drop down in counts can be the first ∼20 pixels, a plateau where a peak is seen for rowA and the 'memory' effect. The 'memory' effect, shows still some signal on the same pixels as the spectrum before the peak was located.

4 DFMS characteristics

This chapter gives an overview of the data treatment and the characteristics of DFMS. In the ion source the neutrals are bombarded with electrons, this can cause an instrument dependent characteristic fragmentation of molecules. How efficient a neutral is ionized depends on the ionization cross section of the neutral, which depends on the bombarding electron energy. The transmission through the sensor is an instrument characteristic function, and takes into account possible mass discrimination and the ion optical path through the instrument. The data evaluation of the different detectors is fundamental, and possible calibration functions for DFMS FM and FS are given. Corrections of the data especially for the MCP/LEDA detector are given in the order of data treatment. The pixel gain and the recalibration of the MCP/LEDA gain polynomial are necessary correction factors for the data analysis of the MCP/LEDA. The results presented here are a continuation of earlier work and detected problems.

The sensitivity (S) of DFMS for the detection of a neutral species can be divided into three parameters:

$$S \propto \sigma \cdot \tau \cdot yield \tag{15}$$

Where S is the sensitivity, σ the ionization cross section, τ the sensor transmission and *yield* the detection efficiency.
The ionization cross section is species and electron energy dependent. For DFMS the electron energy is nominal set to 45 eV (for detailed explanation see Schläppi (2011)) but can be varied. The transmission through the sensor gives knowledge about how efficient ions are guided through the sensor depending on their mass to charge ratio. For DFMS the transmission is not the same for both resolutions since the flight path through the sensor is not the same. The detection efficiency is highly dependent on the type of detector. For example the impinging ion on the MCP/LEDA must have enough kinetic energy to release secondary electrons. The detection efficiency of the CEM and FC is not species dependent and therefore can be set to one.

4.1 Ion source

The ionization of neutrals in the ion source is an electron impact ionization. The energy of the electrons has an influence on the ionization efficiency and the fragmentation of a neutral. The electron bombardment of neutrals can cause fragmentation of the molecule, the distribution of the main molecule (*parent*) and the fragments depends on the molecule and the electron energy, as well as the detection efficiency. It is therefore highly instrument dependent.

4.1.1 Ionization cross section

The probability of a particle to get ionized by electron impact is proportional to the ionization cross section. Therefore, a particle is more likely to get ionized, if the ionization cross section is bigger. The ionization cross section of a particle depends on the size of the particle and the energy of the impacting electron. Furthermore the electron energy must be high enough to ionize the neutral. The ionization energy for neutral atoms in the ground level is < 25 eV [Handbook of Chemistry and Physics, 2012]. The ionization efficiency has a rather typical maximum for an electron energy of 70 – 100 eV (see Fig. 23). However, this is not the case for DFMS, since the ion source geometry also has an influence on the ionization efficiency and the maximum is at 45 eV (see Schläppi (2011)).

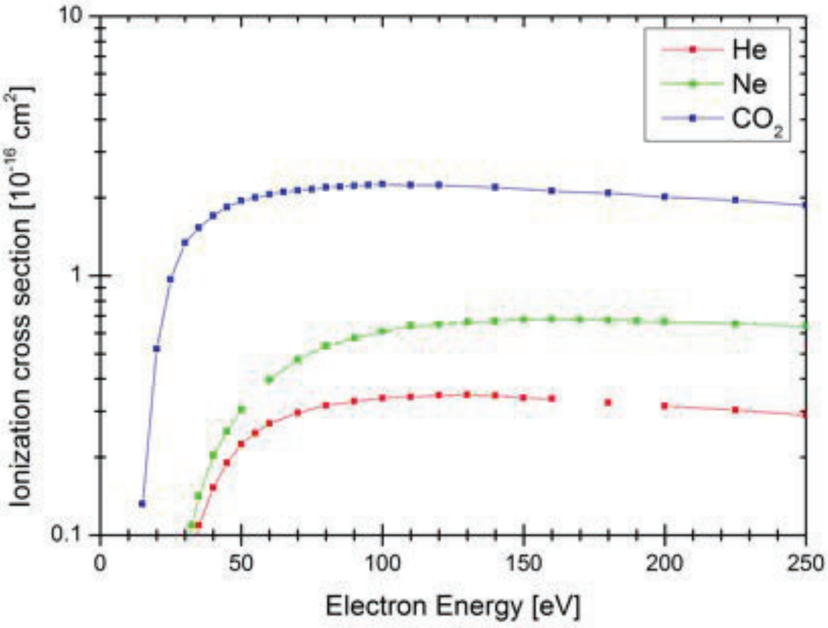

Figure 23: Ionization cross section of He, Ne and CO_2 dependent on the electron energy. A maximum for the ionization cross section can be found for electron energies of 70 – 100 eV. Data from Rice University (2013).

4.1.2 Fragmentation pattern

The fragmentation pattern of a molecule is an instrument dependent pattern. During the ionization process (by electron impact ionization) not only the *parent* is ionized it also can fragment into fragments. The fragmentation pattern is highly dependent on the electron energy. The fragmentation of the *parent* can be forced with higher electron energies. The lower electron energies causes a higher amount of *parents* and simplifies the interpretation of a spectrum. The fragmentation pattern for CO_2 measured with DFMS FM for different electron energies compared to NIST[d] can be found in Fig. 24. The fragmentation pattern is the intensity of the *parent* (CO_2) and the fragments (CO and O) relative to the sum of the intensity (CO_2, CO, O and CO_2 doubly charged). C is also a fragment of CO_2 but since the mass range detected by the MCP/LEDA does not cover this mass, the intensity of C is not taken into account. The fragmentation pattern for an electron energy of 45 eV does not fit the NIST values for 70 eV. A reason for this could be that the electron energy is reduced for DFMS, and therefore less fragmentation occurs. However the fragmentation pattern of NIST can neither be reproduced with an electron energy of 70 eV (see Fig. 24).

---

[d] The data in NIST (*http : //webbook.nist.gov/chemistry/*) for the fragmentation pattern is given as normalized intensities for the fragments or the *parent*. This intensity was then normalized to the total of the intensities.

Therefore measurements of the fragmentation pattern are part of the calibration campaign for DFMS. With a reduced electron energy of 22 eV it is clearly visible that the amount of detected *parents* is much higher and almost no fragmentation occurs (see Fig. 24). There are still some fragments detectable but the amount compared to the total signal for CO_2 is much smaller. The same effect in the other direction can be seen for an electron energy of 70 eV. The amount of fragments is much higher than for 45 eV while the signal of the *parent* is depleted. The amount of doubly charged CO_2 recorded with DFMS FM regardless of the electron energy is much lower than for NIST. The setting of different electron energies are helpful for the interpretation of the data to distinguish fragments from *parents*. For example the signal for CO can be due to the fragmentation in the ion source of CO_2 or of the *parent* itself. The total signal of CO_2, including the signal of the *parent* and the fragments, is much higher for an electron energy of 45 eV. The total signal for CO_2 with an electron energy of 22 eV is only $\sim$ 12% of the total signal for 45 eV, while the total signal for CO_2 with an electron energy of 70 eV is 36%. This is in agreement with the above mentioned fact, that the ion source of DFMS is more efficient for an electron energy of 45 eV.

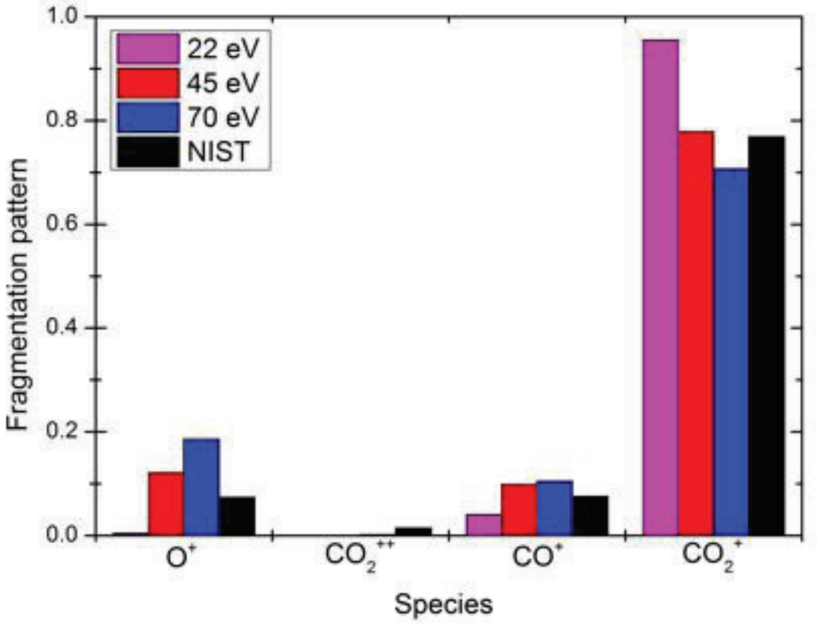

Figure 24: Fragmentation pattern comparison of CO_2 for different electron energies in the ion source, recorded with the MCP/LEDA. For discussion see text.

4.2 Sensor transmission

Transmission of a particle through the instrument is a mass/charge dependent function. The knowledge about the transmission can help to deduce possible sensitivities for species that could not be measured. This is the case for compounds that could harm the instrument, not be introduced into the calibration chamber, or for which the pressure could not be stabilized. In principle, the transmission can be deduced for every species for which the ionization cross section, the fragmentation behavior, the sensitivity and the detection efficiency of the detector is known (according to Equ. 15). However, the fragmentation behavior of DFMS is part of the calibration campaign and can therefore not be assumed to be well known. This leaves the noble gases as candidates to deduce the sensor transmission, since noble gases do not fragment and the ionization cross section is well known for different electron energies. To avoid uncertainties of the detection efficiency the transmission of the instrument was deduced from CEM measurements. The sensor transmission of DFMS can be deduced from the sensitivity measurements of the noble gases (for a detailed description of the sensitivity measurements see Sec. 5.4). The sensitivities of the noble gases are then corrected for the different ionization cross sections for an ionization energy of 45 eV relative to Ar. The correction factors for the different noble gases can be found in Tab. 7. Since the ion path through the sensor is resolution dependent, the transmission function is given for both resolutions independently.

Table 7: The ionization cross section for noble gases for an ionization energy of 45 eV [Rice University, 2013].

Species	Ionization cross section [$10^{-17}\ cm^2$]	Correction factor relative to Ar
Ne	2.5	0.10
Ar	24.9	1.00
Kr	33.8	1.36
Xe	46	1.86

$$\tau_{HR}(m) = a_{HR} \cdot m^{-1.135} \tag{16}$$

$$\tau_{LR}(m) = a_{LR} \cdot m^{-0.853} \tag{17}$$

τ_{HR} is the transmission of the instrument for HR and τ_{LR} for LR.
The transmission function has an emission and resolution dependent correction factor a, while m is the mass to charge ratio of the species.
It is known from previous measurements that the sensitivity for an emission current of 200 μA is slightly lower than for the other emissions. This can be explained by the higher space charge around the filament, that widens up the electron beam and the ratio of electrons reaching the ionization region is lower compared to the other emissions. To account for this process the correction factor a_i for the transmission is slightly lower for 200 μA. The correction factor a_i for all emissions and both resolutions can be found in Tab. 8.

Table 8: The correction factors a_i for τ for all emissions and both resolutions.

Emission	HR/LR	a_i for τ
2 and 20 μA	LR	3.126 x 10^{-16}
200 μA	LR	1.304 x 10^{-16}
2 and 20 μA	HR	8.411 x 10^{-17}
200 μA	HR	2.147 x 10^{-17}

The sensor transmission should be the same for FS and FM. However, the sensitivity for the FS for 200 μA is known to be higher than for the other emissions. This is documented in several memos about the sensitivity of GCU measurements (see Eberhardt (2008a), Altwegg (2008a), Eberhardt (2008b), and Altwegg (2008b)). A possible explanation could be that the ion source geometry is slightly different for the FS and the electrons are guided more efficient into the ionization region than for the FS. Therefore the correction factors a_i of the FM for an emission of 200 μA should be adapted for the FS.

4.3 MCP/LEDA data

The MCP/LEDA is the main detector of DFMS. It consists of MCP and LEDA of two independent rows each with a pixel number of 512. To derive the ion current per spectrum for one species i the following steps have to be taken into account:

1. Subtract offset for both rows individually
2. Correct for individual pixel gain for both rows separately
3. Apply mass scale for both rows individually
4. Sum of the peak of species i for both rows together (Sum_i)
5. Correct for MCP_{Gain}
6. Calculate ion current ($I_{MCP,i}$) for species i

$$I_{MCP,i} = \frac{Sum_i \cdot c_{adc} \cdot c_{leda}}{MCP_{Gain} \cdot t} \tag{18}$$

Where $c_{adc} = \frac{2.5V}{2^{12}-1}$ is the conversion factor of the 12 bit LEDA analog to digital converter and $c_{leda} = 4.22 \cdot 10^{-12}\ F$ the anode capacity and divided by the total integration time t (nominal $t = 66$ ms $\cdot\ 300 = 19.8$ s). The ion current $I_{MCP,i}$ is then in A.

For calibration purposes as well as for the evaluation of the statistical error the number of ions per spectrum is useful and defined as:

$$n_i = \frac{I_{MCP,i} \cdot t}{q} \tag{19}$$

where n_i is the number of ions of species i per spectrum, $I_{MCP,i}$ is the ion current, t the total integration time and q the elementary charge.

The statistical error in % of $I_{MCP,i}$ is therefore

$$\Delta n_i = \frac{1}{\sqrt{n_i}} \cdot 100 \tag{20}$$

The above mentioned steps to derive the ion current per spectrum are discussed step by step in the following chapters. The applied corrections for the FM are used during calibration in Chapter 5) and possible approaches for the FS are mentioned.

4.3.1 Offset correction

Before a spectrum is recorded on the LEDA, an amount of charge is applied on both rows of the LEDA. The amount of applied charge depends on the accumulation number of a spectrum, since each time before the LEDA starts to record, the same charge is applied. The nominal integration time and accumulation number is 66 ms and 300. The offset due to the accumulated charge during the recording process of one spectrum, has to be subtracted from the counts in a spectrum. To determine the offset function (O_i), the signal of the peak is cut out, and the remaining counts are then fitted. This has to be done individually for both rows since the applied charge is not the same for both rows. The reason for this could be a slightly different resistance for each row. However, since the amount of charge and the resistance are the same for all recorded spectra of the FM the function of the offset stays the same.

$$O_{FMrowA} = -2 \cdot 10^{-6} p^3 + 0.0017 p^2 - 0.5268 p + 4091.1 - d_A \tag{21}$$

$$O_{FMrowB} = -1 \cdot 10^{-6} p^3 + 0.0013 p^2 - 0.5058 p + 3363.2 - d_B \tag{22}$$

While p is the pixel number, d_A and d_B are adjusted individually for each spectrum to reduce the number of counts to a level of ± 5 counts per pixel, for pixels where no peak is found. The signal of the spectrum in counts is then reduced to a few counts, where no peak is detected, while the counts of the peak is reduced by the offset (see Fig. 25).

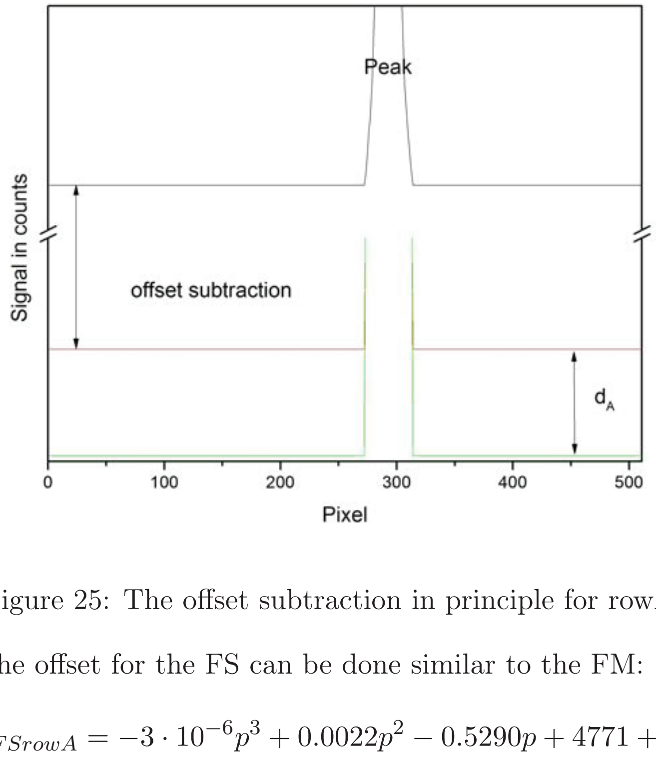

Figure 25: The offset subtraction in principle for rowA.

The correction of the offset for the FS can be done similar to the FM:

$$O_{FSrowA} = -3 \cdot 10^{-6} p^3 + 0.0022 p^2 - 0.5290 p + 4771 + d_A \tag{23}$$

$$O_{FSrowB} = -2 \cdot 10^{-6} p^3 + 0.0015 p^2 - 0.249 p + 5530 + d_B \tag{24}$$

Differences between FM and FS can be explained by the slightly different resistances of the LEDA.

4.3.2 Individual pixel gain

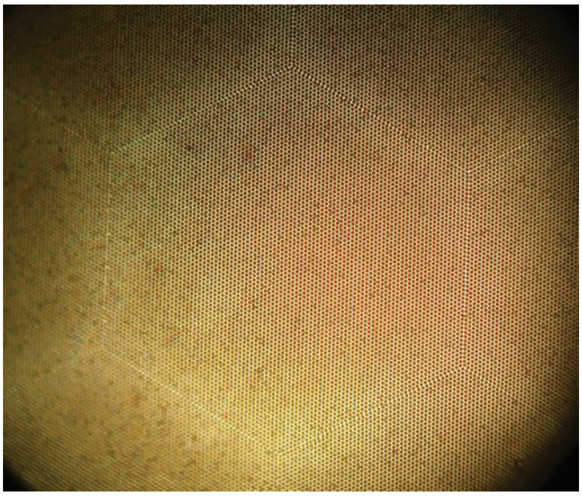

Figure 26: Picture of an MCP with the hexagonal structure due to fabrication fashion. The structure causes a modulation in the individual pixel gain of 24 pixels for the FM.

The pixel gain is a correction factor for every individual pixel to correct for the degradation of the MCP over time. The degradation of the MCP is due to an uneven ion current impinging on the area of the MCP. The ion optics focuses the main ion current in such a way on the MCP, that the commanded mass is in the middle of the MCP. Since therefore, most ions impinge in the middle of the MCP, most electrons are emitted there, resulting in an depletion of the MCP center.
The following proceeding for the measurement of the individual pixel gain correction is a summery of the work of Riesen (2007) and Schläppi (2011). This depletion of the MCP is first mentioned and corrected by Riesen (2007), and is expected and well understood. Measurements for the pixel gain correction are performed and analyzed in the following way:

- A narrow peak (LR) is shifted with a step width of 4 pixels over the whole MCP/LEDA by commanding slightly different masses. The range of the commanded masses is given by the mass range of one spectrum. Δm is then calculated according to the mass range of 4 pixels. For example if the peak is H_2O, the mass range is 17.05 u/e – 18.98 u/e, $\Delta m = 0.0145$ and a total of 134 spectra is recorded. The detector gain of the MCP has to remain the same during recording. Therefore the gain algorithm that calculated the detector gain according to the intensity of the peak, has to be switched off once the detector gain is adjusted for the peak to be shifted.

- To calculate the pixel gain correction factors, the intensities of the peaks relative to the pixel are added and scaled to the average of pixel 20 to 492 to avoid border effects of the MCP/LEDA. The dimensionless correction factors are then in the range of ∼0.4 – 1.5. A correction factor of 1.0 means that the intensity of the peak recorded for this pixel is exactly the average of the other intensities.

The commanding of the different masses can be done within a measurement mode for H_2O, on the detector gain adjusted by the gain algorithm for the intensity of the H_2O peak (FM

and FS). An other possibility for the FM is to use a batch wherein, the species and the gain step can be adapted (integration time is 6.6 s). The shift in pixels is optimized for recording time and modulation effects of the step width overlaying the known modulation of the MCP with a step width of 24 pixels for the FM.
The modulation of the pixel gain of the MCP for the FM is well known and due to the fabrication of the MCP. A picture of a MCP fabricated in a similar fashion as for the FM can be found in Fig. 26. The fabrication of the MCP for the FS was different to avoid this modulation.

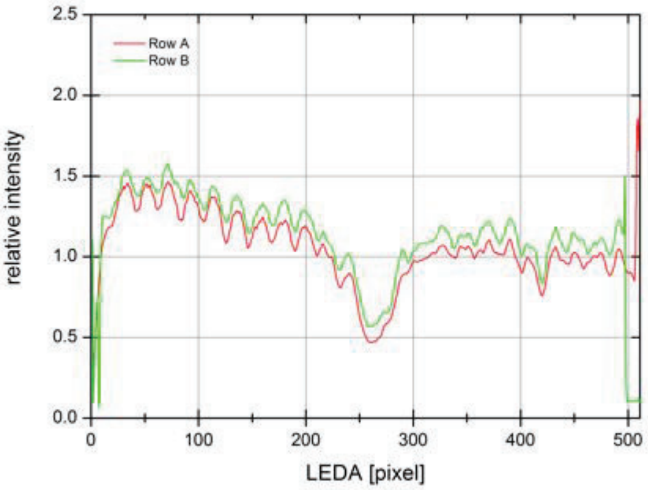

Figure 27: FM individual pixel gain of rowA and rowB of the same species on the same MCP_{Front} (GS=14). To distinguish the two rows, rowB is plotted with an offset of 0.1. No reliable corrections are given for the edges of the MCP, due to data processing.

The proceeding of the spectra is done separately for rowA and rowB. RowA and rowB are treated separately since the ion beam is not always perfectly focused in the middle of the MCP. However the variation between the two rows is marginal (see Fig. 27).
To apply the correction of the individual pixel gain on a spectrum, the number of counts for every individual pixel is divided by the correction factor of the specific pixel of rowA or rowB for the recorded MCP_{Gain} of the spectrum.
Since the peak in the middle of the LEDA is no longer amplified in the same amount (can be less than 50% of the nominal amplification) through the MCP, the correction factor there is the lowest one. The correction factor is not dependent on the species of the peak but highly dependent on the gain step or the difference of $MCP_{Front} - MCP_{Back}$ (see Riesen (2007) and Schläppi (2011)). A specific difference between $MCP_{Front} - MCP_{Back}$ is called gain step (GS). The highest gain is GS 16 and has a $\Delta(MCP_{Front} - MCP_{Back})$ of -2300 V, the lowest gain has GS 1 and $\Delta(MCP_{Front} - MCP_{Back})$ is -1300 V.
For a successful and correct recording of the individual pixel gain for one GS (duration 2 h) a highly stable density of the recorded species around the instrument is necessary. This requires a regulated pressure (if additional gas is introduced into the chamber) and a temperature stable instrument and environment. The intensity of the ion beam that is shifted over the MCP should be stable, therefore variations of the density around the instrument and in the chamber should be limited. To get a stable environment for the FS the variations

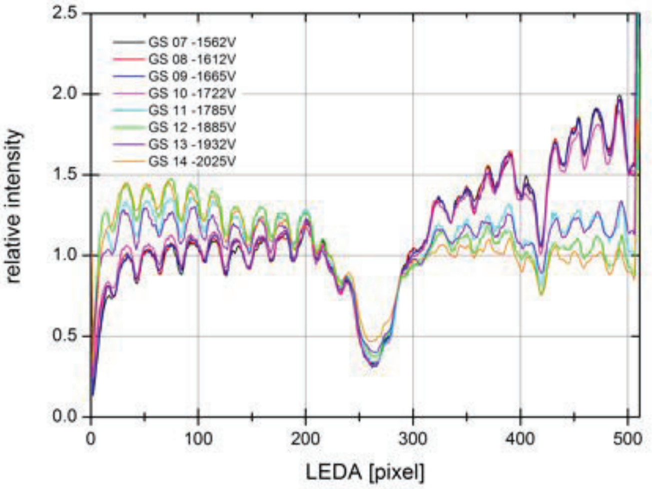

Figure 28: FM individual pixel gain of row A on gain step 7 to 14.

of the densities around the instrument due to spacecraft outgassing [Schläppi et al., 2010] have to be limited.

A set of the recorded individual pixel gain for the FM can be found in Fig. 28. The recording is part of the calibration measurements and the resulting correction factors are applied during analysis. The set was recorded with the above mentioned batch on several species. GS 16 to 11 was recorded with a peak of the background gas, and different emissions. GS 10–7 was recorded with additional CO_2-gas introduced into the chamber with a regulated pressure inlet. To have a stable background density the instrument was running at least 2 h before starting the measurements of the individual pixel gain.

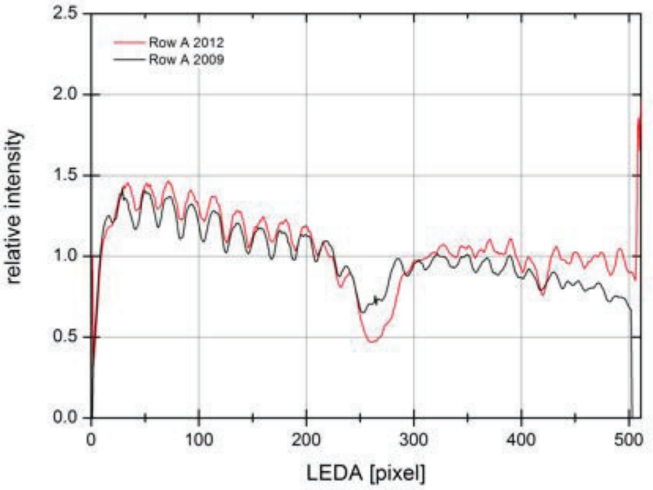

Figure 29: FM comparison of pixel gain recorded in 2009 and 2012, with a depletion in the middle of the MCP of ~40%.

Comparison of the individual pixel gains of FM in Schläppi (2011) and the new recorded ones, show a further depletion of the MCP in the center of ∼40% (see Fig. 29). A further depletion was expected since the measurements recorded with the MCP were proceeding. Between the two measurements are ∼3000 h of MCP operation or 3 years of intense measurement period. The recording of a set of the individual pixel gain for the FM as well as for the FS should therefore be done on a regular time basis depending on the MCP operation time. For the FS a measurement set every 3–4 month is therefore recommended.

4.3.3 Applying the mass scale

The most difficult and critical step is to apply the mass scale. In this step the pixel numbers are translated into mass to charge ratios. A shift of several pixels can lead to completely different interpretations according to the species that caused the spectrum. While for m/q = 13 u/e there exists only tow species that can cause a peak on this spectrum (^{13}C and CH), for m/q = 19 u/e much more possibilities exist and the peak of fluorine might be wrongly interpreted as ^{18}OH (a shift of 15 pixels). Therefore this step has to be done very careful. The mass of a spectra according to the pixel number can be calculated as:

$$m(p) = m_0 \cdot e^{(p-p_0)\frac{x}{D \cdot z}} \tag{25}$$

Where $m(p)$ is the mass to charge ratio that falls on this specific pixel p, which is the pixel number ($1 \leq \mathrm{p} \leq 512$). p_0 is the pixel where the commanded mass m_0 is located and x is the step width between two pixels ($x = 25\ \mu m$). D is the dispersion factor (D = 127'000 μm [Wüthrich, 2007]) and z is the zoom factor (LR: $z = 1$ and HR: $z = \sim 6.4$)
In an ideal case of a perfectly adjusted instrument, the ion optical axis of the sensor intersects the focal plane of the MCP/LEDA. The commanded mass m_0 of a spectrum should therefore be in the center of the MCP/LEDA, on pixel 256, and both rows should record exactly the same signal (after subtraction of the offset). In general this is true and the consequence thereof is the depletion of the MCP in the middle section. However, the commanded mass m_0 is not always on pixel 256 but falls on pixel zero (p_0). In LR this has a much smaller effect since the resolution between tow pixels is much smaller than in HR (Δm/pixel $\propto e^{\frac{1}{z}}$). For FM shifts of ∼± 50 pixels for p_0 are detected during the calibration campaign for HR. The GCU spectra are important to calibrate p_0 since the expected species (Ne, CO_2 and Xe) are known and therefore the according p_0 for spectra wherein these species are found. However, the GCU spectra give only limited information about p_0, compared to the total mass range. An other phenomenon is a shift of p_0 for $m_0 \geq 70$ u/e in HR, due to the applied post acceleration (PA = -1 kV). The function of p_0 for HR is divided into three parts (see Eq. 26, 27 and 28), to account for the different zoom values (see Tab. 9), since a correction of the zoom value can also cause a shift of p_0. The calculated p_0 according to Eq. 26, 27, and 28 for HR should fit for the first and second order segment of the variable m_0 within ± 2 pixels, while the zero order segment (offset) of the function might change with time due to temperature influences of the magnet.

$$p_0(m_0) = -0.3958 m_0^2 + 15.169 m_0 + 165.03 \qquad 13 \leq m_0 < 22 \tag{26}$$

$$p_0(m_0) = -0.0101 m_0^2 + 0.7971 m_0 + 290.8 \qquad 22 \leq m_0 < 70 \tag{27}$$

$$p_0(m_0) = -0.498 m_0 + 335.25 \qquad 70 \leq m_0 \leq 100 \tag{28}$$

The function of p_0 for LR is a linear function (see Eq. 29), since the number of pixels between two masses is a linear function for the commanded mass. This function is also strongly temperature dependent since the pixel, where the commanded mass impinges depends on the radius of the ion path through the magnet and therefore the temperature.

$$p_0(m_0) = -0.0747m_0 + 266.46 \quad 13 \leq m_0 \leq 136 \tag{29}$$

The calculated p_0 according to Eq. 29 for LR should fit for the first and second order segment of the variable m_0 within ± 2 pixels, while the zero order segment (offset) of the function might change with time due to temperature influences of the magnet.
The dispersion factor of the MCP/LEDA is well known [Wüthrich, 2007]. All the detector potentials are floating on V_{accel} and only this potential is mass dependent, all the other potential differences are constant. This effect is well understood and documented in Wüthrich (2007) and Riesen (2007). Therefore the dispersion factor is a constant over the total mass range since the distribution of the ion beam over the MCP/LEDA is dependent on the potential differences of the detector.
The zoom factor is constantly one for LR since the zoom optics are not applied in this measurement mode. For HR the zoom factor is nominal 6.4 but because of a recalibration of the mass dependent voltages applied on the zoom quadrupoles, for $m_0 \leq 20$ u/e, the zoom factor is in the range of $5 \leq z \leq 6.6$ (see Tab. 9). To account for the applied post acceleration and resulting concentration of the peaks on the LEDA, the zoom factor for $m_0 \geq 70$ u/e is much smaller than the nominal 6.4 (see Tab. 9).

Table 9: Zoom values for HR for DFMS FM

m_0	z [± 0.2]	m_0	z [± 0.2]
13	5.8	21–69	6.4
14	5.3	78	3.8
15	6.0	80	3.8
16	6.3	82	3.8
17	6.4	83	3.8
18	6.3	84	3.8
19	6.6	86	3.8
20	6.2		

4.3.4 MCP/LEDA gain polynomial

The MCP/LEDA gain polynomial describes the amplification of the signal through the MCP. If an ion impinges on the MCP, a cascade of electrons is released and detected on the LEDA. To interpret the number of counts into the number of ions that impinged on the MCP, the gain of the MCP has to be known (see Eg. 30). The gain of the MCP is described as a function depending on the potential difference of the MCP ($MCP_{Front} - MCP_{Back}$). A specific difference between $MCP_{Front} - MCP_{Back}$ is called gain step (GS). The highest gain for FM is GS 16 and has a $\Delta(MCP_{Front} - MCP_{Back})$ of -2300 V, the lowest gain has GS 1 and $\Delta(MCP_{Front} - MCP_{Back})$ is -1300 V.

$$Gain = \frac{\#ions}{\#electrons} \tag{30}$$

The calibration of the gain polynomial was first performed during the detector calibration. These measurements were done for the FM and the FS only with the detector in the calibration chamber (FM: Nevejans et al. (2001) and FS: Neefs et al. (2002)). A refitting of the gain polynomial was done during the pre flight calibration campaign (FM: Langer (2003a) and FS: Langer (2003b)). However during the calibration of DFMS FM by Riesen (2007), a correction factor for the gain was applied to compare measurements of different GS. To avoid this correction factor the gain polynomial was re calibrated for this work.

$$MCP_{Gain} = \frac{I_{ion}}{I_{leda}} \tag{31}$$

Where I_{ion} are the number of ions that impinge on the MCP and I_{leda} is the signal measured on the LEDA. Typically the gain of a two stack MCP with the above mentioned configuration and dimensions is in the range of $\sim 10^6$ at an applied voltage of -2 kV.

The measurement setup was the same as for the measurements of the individual pixel gain. For high GS the signal of the background gas was used while for lower GS additional gas (CO_2) was let into the chamber. Spectra in LR of the commanded mass 16, 18, 20, 34 and 44 are measured on the nominal GS for the signal. Then the GS was manually adapted (± 1 GS) and a spectrum was recorded. The factor between two gain steps is given by the ratio of the peak areas at the corresponding gain steps. To avoid pixel gain corrections, the highest signal of the peak is manually shifted to the same pixel. If several measurements were done for the same gain steps the average of the ratio between two measurements was taken. The statistical error is the standard deviation of the average. For the total uncertainties of 6% the statistical error of the single measurements $< 3\%$ as well as uncertainties of the average $< 5\%$ are taken into account.

Table 10: MCP/LEDA Gain Table

Gainstep	*Gain* FM *old**	$MCP_{Front} - MCP_{Back}[V]$	*Gain* FM $refitted^{+}$
1	4.94E-02	-1300	1.41E-01
2	2.62E-01	-1342	3.88E-01
3	1.16E+00	-1382	1.01E+00
4	5.11E+00	-1425	2.79E+00
5	2.02E+01	-1468	7.63E+00
6	7.82E+01	-1514	2.20E+01
7	2.84E+02	-1562	6.48E+01
8	9.64E+02	-1612	1.94E+02
9	3.09E+03	-1665	5.97E+02
10	9.40E+03	-1722	1.90E+03
11	2.76E+04	-1785	6.41E+03
12	7.73E+04	-1855	2.25E+04
13	2.01E+05	-1932	7.84E+04
14	5.19E+05	-2025	2.89E+05
15	1.34E+06	-2140	1.02E+06
16	3.97E+06	-2300	2.78E+06
	*[Langer, 2003a]		$^{+}$ *in this work*

Two gain ratios (1-2 and 2-3) were not measured, because no signal could be detected for a pressure of $\sim$ 5 x 10^{-7} mbar. Therefore they were extrapolated from the gain polynomial,

which fits the detector gains for the gain steps 3 to 16. However, the physical interpretation of a gain < 1 is not understood by the author and measurements are not likely to be performed on this gain steps. The absolute calibration of GS 16 was done with single ion measurements. The pressure level was adjusted so that the number of ions impinging on the MCP within one spectrum (2 s) were limited to one. The resulting signal on the LEDA, was then interpreted as the gain for one ion. The average of the 100 single ion measurements then gives the start point of the gain polynomial at gain step 16. Because of the uncertainties due to statistics the total error (10%) for this point is slightly higher than for the other measurements (see Fig. 30), however total uncertainties are smaller than symbol size.
The calculated gain polynomial is the following:

$$MCP_{Gain}(x) = 10^{2.36\cdot10^{-9}x^3+8.33\cdot10^{-6}x^2-9.26\cdot10^{-4}x-10.95} \tag{32}$$

Whereas x is $MCP_{Front} - MCP_{Back}$ voltage. The measured gain is not comparable to the old measurements within error bars therefore the gain polynomial was refitted. An explanation could possibly be found in the different measurement setup. In the first setup only the detector was used for calibration and now the whole sensor. Another reason could be the decreasing of the MCP's efficiency due to aging.
Isotopic measurements of the D/H ratio for Water in LR of H_2O and $HD^{18}O$ imply high accuracy for the refitted gain polynomial (for further detail see Sec. 5.5). The ratio is measured, covering seven gain step and fits the literature value within error bars.

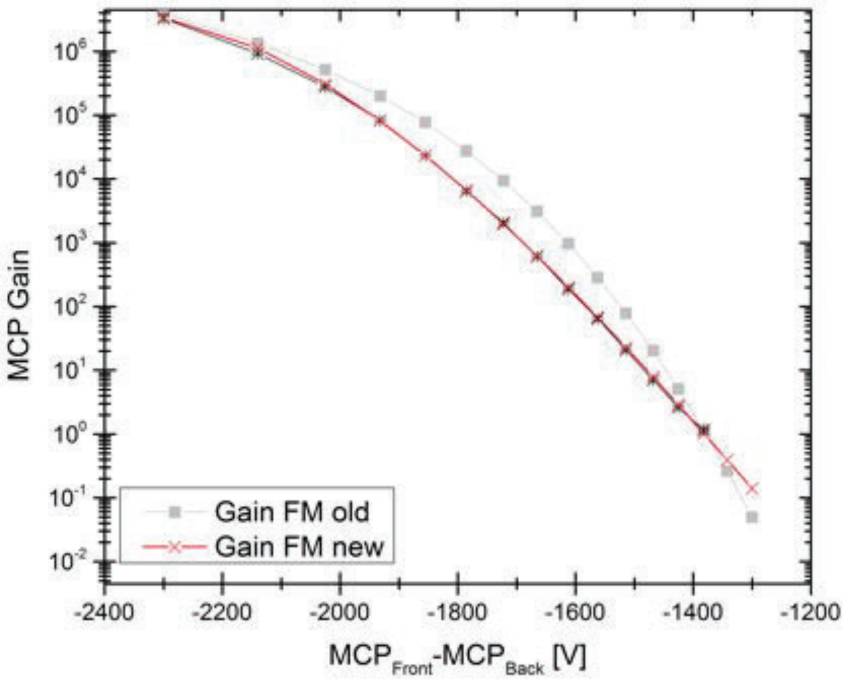

Figure 30: MCP gain for DFMS FM. The 'old' gain are the gain values from the first calibration [Langer, 2003a] and 'new' gain are the values of the calibration in this work.

4.4 CEM data

To evaluate CEM data, the calculation of the ion current for the CEM is described and the mass shift between two steps to calculate the mass scale. The CEM detector is mainly operated in digital mode, where CEM operates in a constant high gain plateau at a front voltage of – 2337 V. The repetition voltage in the CEM is – 100 V. In this mode events are counted, more precisely the arrival of a secondary electron cloud, caused by an impacting ion. The saturation limit for counting is around $2 \cdot 10^6$ events per second. A spectrum of the CEM detector is recorded by shifting the ion beam in little mass steps over the entrance slit of the CEM detector. The nominal integration time per step is 1000 ms and the number of steps is mass and resolution dependent.

Table 11: CEM mass step width and number of steps per spectrum

	Step width	Number of steps
Low resolution	$\Delta m = \frac{m}{1000}$	$\sim \frac{140}{\sqrt{m}} + 1$
High resolution	$\Delta m = \frac{m}{10000}$	$\sim \frac{240}{\sqrt{m}} + 1$

The shifting of the ion beam over the entrance of the CEM causes an overlap of the ion beam. The overlap is calculated the following:

$$c_{ol} = \frac{D\frac{\Delta m}{m}}{w_s} \tag{33}$$

Where D is the dispersion (127'000 μm), $\frac{\Delta m}{m}$ is the step width and w_s is the width of the entrance slit of 25 μm. The overlap correction factor for LR is $c_{ol} = 5.08$ and $c_{ol} = 0.508$ for HR.

The ion current of a species i ($I_{CEM,i}$) of the CEM detector operated in digital mode is calculated the following:

$$I_{CEM,i} = \frac{c_{ol} \cdot Sum_i}{t} \tag{34}$$

The Sum_i is the sum of the peak of species i and t is the integration time per step (nominal 1 s). The statistical error of the CEM is calculated in the same way as for the MCP/LEDA in Eq. 19 and 20.

4.5 FC data

To evaluate FC data, the calculation of the ion current for the FC is described. The FC has an entry slit width of 0.35 *mm* which is big compared to the beam width (∼0.25 *mm*) in high resolution mode and comparable to the beam width (∼0.357 *mm*) in low resolution mode. While stepping the ion beam over the detector entrance of the FC, the ion beam will always reach a position where the whole beam passes into the detector unhindered. Therefore, the amplitude of the peak is used for ion current calculations. The FC step size is not resolution dependent nor the number of steps:

$$\Delta m = \frac{m}{2000} \tag{35}$$

m is the commanded mass and the number of steps is then $\sim \frac{240}{\sqrt{m}} + 1$. The integration time t per step is 1 s. The Faraday Cup is a simple detector with only an electrometer at its end. A spectrum consists of the measured electrometer output per step which is provided in the unit mV.

The ion current of species i ($I_{FC,i}$) of the FC detector is calculated the following:

$$I_{FC,i} = \frac{c_{el} \cdot V_{max,i}}{t} \tag{36}$$

Where $V_{max,i}$ is the amplitude of the peak of species i, c_{el} is the correction constant to transfer the measured voltage into the corresponding current.

$$c_{el} = 3.33 \cdot 10^{-15} \left[\frac{A}{mV}\right] \tag{37}$$

The statistical error of the FC is calculated in the same way as for the MCP/LEDA in Eq. 19 and 20.

4.6 Sensitivity

The sensitivity of a sensor for one species is the detected particles (atom or molecule) relative to that available. To detect a particle it has first to be ionized, where fragmentation can occur, then guided through the sensor and finally detected. The sensitivity of DFMS for species i is defined as the total signal (current) detected for the species relative to the density of the species and the emission:

$$S_{total,i} = \frac{I_{ion}}{\rho I_{emi}} \tag{38}$$

While $S_{total,i}$ is in cm^3, I_{emi} is the emission current in A and ρ is the density in cm^{-3}. I_{ion} is the current detected for i. The total signal contains the signal due to the *parent*, the fragments, the isotopes and the doubly charged particles. To transform the signal into the corresponding ion current, the data is proceeded as described in Sec. 4.3, 4.4, and 4.5.

Unfortunately the densities are usually measured as pressures, although a current and therefore a density is measured and correction factors for different species have to be applied. The relation between density (ρ) and pressure (p) in a specific volume is given by:

$$pV = Nk_BT \quad \Rightarrow \quad \rho = \frac{N}{V} = \frac{p}{k_BT} \tag{39}$$

While p is the pressure in Pa, V is the volume in cm^3, N is the number of particles, k_B is the Boltzmann constant (1.38 x 10^{-23} J/K) and T is the temperature in K.

To calculate the density for a specific pressure, a room temperature of 293 K was used in the lab.

The sensitivities of the CEM and the FC for one species should be comparable within uncertainties since both detectors measure a current. The difference between the MCP/LEDA and the CEM in sensitivity is the relative detection efficiency (*yield*). The detection efficiency of the MCP/LEDA depends strongly on the released electrons of the MCP when an ion impinges on the MCP. The yield of a micro channel plate can be calculated (see Meier and Eberhardt (1993)), however the calibration for this calculation was performed with a similar micro channel plate configuration but with much higher gains, and as discovered during calibration the values might not fit necessarily for the MCP/LEDA setting of DFMS. A factor of ∼14 between the sensitivity for low and high resolution can be explained by the resolution dependent slit area (200 μm / 14 μm = 14.3), however this is no longer true when post acceleration is applied in HR. Nevertheless the transmission through the sensor is also resolution dependent and therefore the factor between LR and HR can vary. However the knowledge about this corrections might help to estimate the sensitivity for species, that are not applicable for calibration measurements, because this species can harm the instrument, the chamber or are poisonous.

5 Calibration of DFMS in a static environment

To understand and interpret data of ROSINA at the comet, the sensors have to be calibrated in an environment similar to that of the comet. Therefore the testing environment CASYMIR (CAlibration SYstem for the Mass spectrometer Instrument ROSINA) was designed for this purpose. The calibration of DFMS describes the sensitivity of the instrument for different species, the fragmentation behavior of the ion source, the capability to measure isotopic ratios, and the relation of the signal of the instrument relative to different densities of the environment. To simulate the different velocities of neutrals relative to the instrument, CASYMIR can be operated in two modes: static and dynamic. In the static mode the velocity distribution of the neutrals is thermal and the same for every direction. In the dynamic mode the neutrals have a velocity in one direction. Both sensors FM and FS were calibrated within a calibration campaign with a limited number of gases (CO_2, Ne, Xe, and the GCU-gas, that is a mixture of the three) [Langer et al., 2003]. The further calibration of the FM for several species is key to understand and interpret the measurements at the comet. The first calibration campaign for neutral species after launch can be found in Riesen (2007). The calibration therein was performed in a static and dynamic mode for CO_2, Ne, Kr, and Xe.

The calibration is focused on the following measurements: sensitivity of the instrument for different species, fragmentation behavior of the ion source, and ability to measure isotopic ratios. The calibration campaign presented in this work was performed for the following species:

Table 12: The gases used for calibration of DFMS FM.

Species	Description	Purity* [%]	Remark e.g.
Ne	Neon	99.9998	[Bockelée-Morvan et al., 2004]
Ar	Argon	99.9998	[Bockelée-Morvan et al., 2004]
Kr	Krypton	99.9998	[Bockelée-Morvan et al., 2004]
Xe	Xenon	99.9998	[Bockelée-Morvan et al., 2004]
H_2O	Water	distilled	[Hartogh et al., 2011]
N_2	Nitrogen	99.9998	[Bockelée-Morvan et al., 2004]
CO_2	Carbon dioxide	99.9998	[Bockelée-Morvan et al., 2004]
CH_4	Methane	99.9998	[Bockelée-Morvan et al., 2004]
C_2H_6	Ethane	99.9998	[Bockelée-Morvan et al., 2004]
C_3H_8	Propane	99.9998	[Schläppi et al., 2010]
C_4H_{10}	n-Butane	99.9998	[Schläppi et al., 2010]
C_2H_4	Ethylene	99.9998	[Bockelée-Morvan et al., 2004]

* purity is given by gas company

5.1 Calibration facility (CASYMIR)

CASYMIR was designed for the calibration of the ROSINA instruments in 1997 – 2000 and further updated during subsequent measurement campaigns. A detailed description of the assembly of CASYMIR and the diagnostic tools can be found in Westermann (2000). CASYMIR is designed to simulate the atmospheric conditions in the vicinity of the comets nucleus. It is designed in a multi staged vacuum chamber system to allow calibration at very low gas pressure as well as calibration within a neutral molecular beam (see Westermann et al. (2001) and Fig. 31). The calibration facility can be operated in either static or dynamic mode to calibrate mass spectrometers. In the static mode only the last two volumes (V1 and V0) in front of the instrument are used. The gas inlet is performed through a leak valve (LV4). In the dynamic mode, gas from the gas mixing unit (GMU) is introduced through the nozzle into chamber V3. The beam is then collimated by a skimmer between V3 and V2. An iris between V2 and V1 can reduce the area of the beam. In V1 and V0 the beam can expand and is measured at the end of the docking section by an instrument.

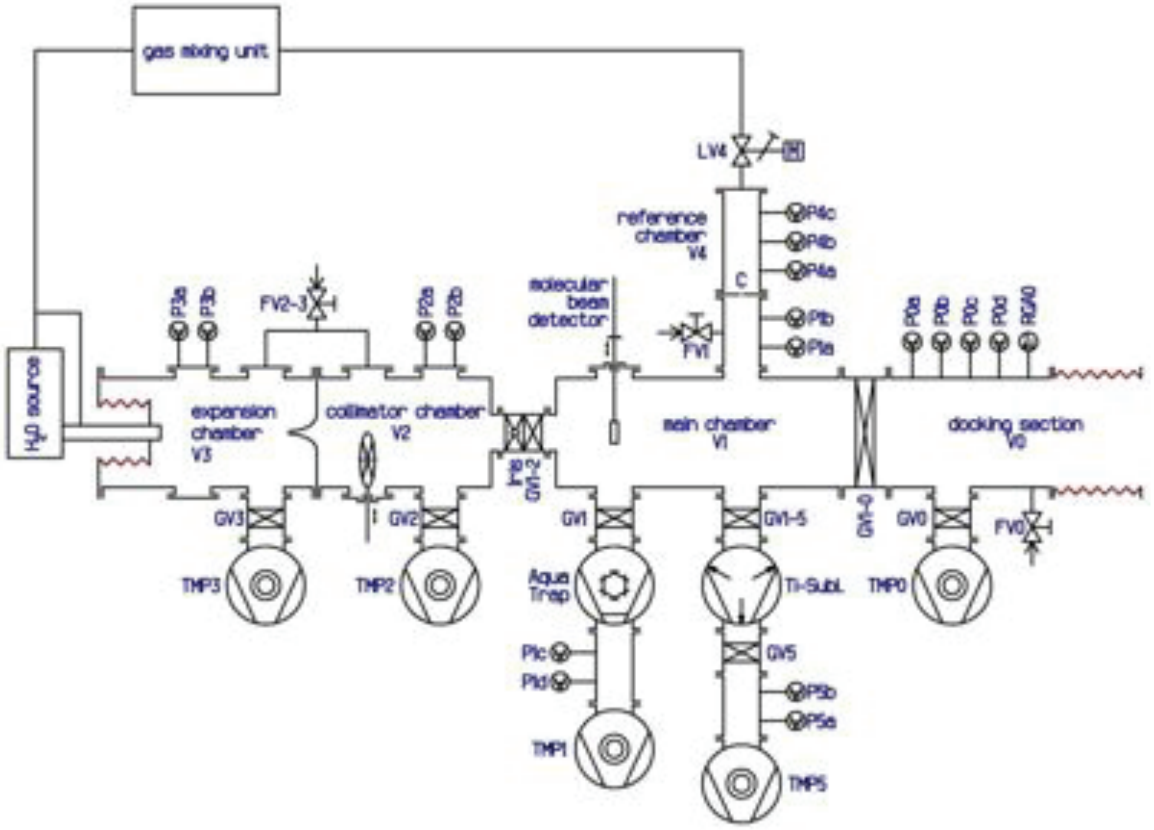

Figure 31: CASYMIR: This figure shows a schematic view of the calibration facility. The instrument is docked on the right hand side after the bellows. The facility allows introduction of the gas in two different ways: static mode and dynamic mode. In the dynamic mode, gas from the gas mixing unit in the upper left and is introduced through the nozzle into V3. The beam is then skimmed between V3 and V2. An iris between V2 and V1 can reduce the area of the beam. In V1 and V0 the beam can expand and is measured at the end of the docking section by an instrument. In the static mode gas is introduced into V1 through a needle valve (LV4), while the V2 is separated from V1 by a closing a gate valve.

The calibration presented in the following text, was performed in a static mode. To avoid contamination, the bottles are directly attached in front of the leak valve (LV4), while pumping and purging was performed through the GMU. The GMU can be filled with gas through flow controllers, but this is only used for gas mixtures of several gases to control the ratio of the gas mixture in the GMU, or for the dynamic mode. In the dynamic mode a beam of one or more gases is introduced through the nozzle into the first volume (V3).

5.2 Measurement procedure

The calibration contains measurements for all three detectors (MCP/LEDA, CEM, FC) at all three emission settings (2 μA, 20 μA, 200 μA) in both resolution modes (LR and HR). To measure the pressure as close as possible to DFMS an additional Granville-Phillips ion gauge was installed in the flange where DFMS is attached to the calibration system. The calibration was performed in the most thermal and pressure stable or stabilized environment[e]. To perform the calibration measurements the following procedure was used:

1. The instrument was running in a thermally stable environment while measurements were performed. Therefore the instrument was running at least 1.5 h before the calibration measurements started.
2. Background measurements of the residual gas in the chamber were performed before the calibration gas was introduced into the chamber.
3. The calibration gas inlet was stabilized and controlled with a thermal valve. The calibration measurements were done after a stabilization time of $>$ 0.5 h, although the pressure was already at a stable level before this time.
4. The same measurements were performed for every calibration gas while the same spectra were measured at the beginning of calibration as well as at the end.

The measurements of two gases (Ne and Ar) at the beginning of the calibration campaign were performed on different pressure levels to find a correlation between the density in the chamber and the recorded signal. Once the correlation was found to be linear the rest of the measurements were performed at one pressure level.

5.3 Data treatment

Proper evaluation of the measurements is an essential part of the calibration. To transfer the signal detected into an ion current, the steps for the different detectors (MCP/LEDA in Sec. 4.3, CEM in Sec. 4.4 and FC in Sec. 4.5) were followed as previous described. The sensitivities, fragmentation pattern, and isotopic ratios are calculated:

- Sensitivities
  The sensitivities were calculated according to Eq. 15. The pressure measurements were corrected for the Granville-Phillips ion gauge. Correction factors can be found in App. F.
- Fragmentation pattern
  The fragmentation pattern is the ratio of the intensities of each mass peak belonging to the species relative to their cumulative intensities and is a dimensionless number. For example the fragmentation pattern of H_2O is calculated by dividing the ion currents of O, OH and H_2O by the total of the three. As reference the fragmentation pattern for the same molecule in NIST is given although it is known that the electron energies are not the same. Tables of the fragmentation pattern for each gas can be found in App. E.

---

[e] The calibration in a absolute static environment (no pumps and no gas inlet during measurements) was not feasible, because of sensor protection.

- Isotopic ratios
  The isotopic ratios were calculated by dividing the ion currents measured for the isotope divided by the ion current for the most abundant isotope. The relative isotopic abundances given in literature for Earth [Handbook of Chemistry and Physics, 2012] were then treated in the same way. For comparison the measured value has been divided by the literature value. A value of exactly one indicates that the measurement is in total agreement with the literature value.

5.4 Noble Gases

In the following a summary about remote sensing measurements of noble gases is given [Bockelée-Morvan et al., 2004]: The noble gases (He, Ne, Ar, Kr, Xe, Ra) are highly volatile and chemically inert. The abundances of noble gases in the cometary nuclei as well as in the coma are potentially diagnostic for the role played by cometary bombardment on the formation and evolution of planetary atmospheres. Noble gas abundances are also key indicators of the temperature conditions and condensation processes in the outer solar nebula. The abundances of noble gases in a comet's nuclei are diagnostic of the thermal history of the comet. Remote observations of the noble gases are difficult to perform because their resonance transitions lie in the far-UV ($\lambda \leq 1200$ Å) spectral region. Only space born observations can access these wavelength. The detection of He does not help to solve the riddle about the thermal history of the comet but can be used as probes of the solar wind conditions and of the interaction between cometary nuclei and the evidence of solar wind. However the detection of He in the coma of comet 67P/Churyumov-Gerasimenko is not possible for DFMS since the mass range is limited to 12 u/e. Several upper limits can be found for Ne/O , while a depletion of 25-2600 relative to the solar value could be detected (25: Krasnopolsyk et al. (1997), 2600: Krasnopolsky and Mumma (2001)). The detection of Argon with remote sensing is difficult because of the confusion of Ar with other spectral lines at low resolution, therefore the detection of Ar in comet Hale-Bopp is questionable. The search for noble gases has been attempted by several space born observations but there has not yet been a convincing detection of any noble gas sublimation from a cometary nucleus [Bockelée-Morvan et al., 2004]. Therefore the detection of noble gases in cometary nuclei is questionable and difficult. DFMS will provides the best circumstances yet for the detection of noble gases due to its sensitivity and mass resolution. Therefore it is likely that DFMS will provide the first conclusive measurements of noble gases in the comet's coma.

5.4.1 Ne Neon

The detection of Ne at comets has been questionable although upper limits have been deduced from space born measurements. However Ne was chosen as a component of the GCU-gas of DFMS and therefore used for calibration. The calibration measurements were performed at three different pressure levels: 2 x 10^{-8} mbar, 2 x 10^{-7} mbar, and 4 x 10^{-7} mbar corrected for Ne (for correction factor see App. F). Special calibration modes exist for the FM to measure ^{20}Ne and ^{22}Ne for each detector and all emissions. These modes were used during calibration, therefore the ratio of ^{21}Ne to ^{20}Ne was not measured. However isotopic measurements for this ratio can be found in Riesen (2007) which are in good agreement with literature. The background pressure before calibration measurements was at the level of ~1 x 10^{-9} mbar with a typical residual gas composition containing mostly water and carbon dioxide.

The signal measured with the detector should increase with the amount of particles in the chamber, therefore measurements were performed in three different pressure ranges. The dependency between the pressure and the detected ions on the MCP/LEDA is given in Fig. 32. The number of ions measured on the MCP/LEDA is increasing linear to pressure. Ion statistical uncertainties are smaller then symbol size in the plot.

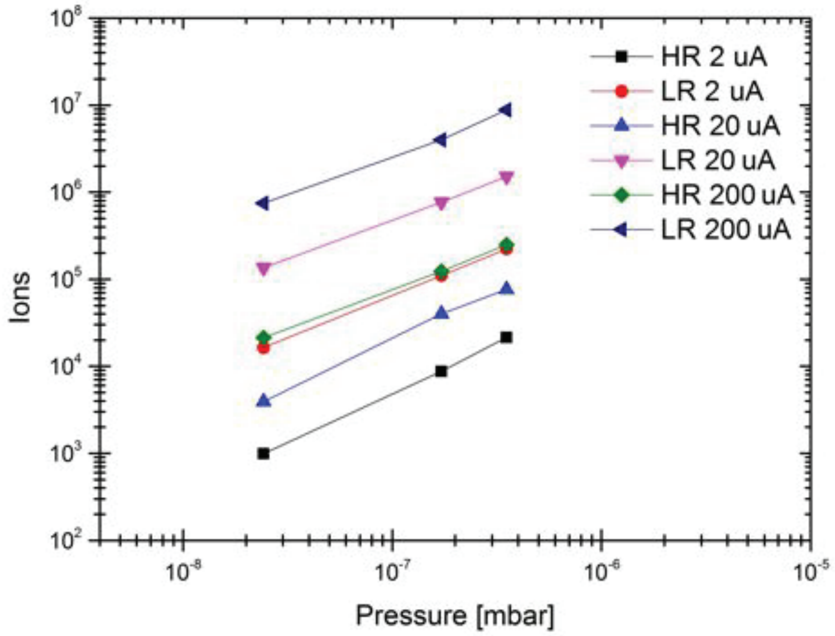

Figure 32: The linearity between measured signal and the pressure for Ne.

Isotopic measurements were performed with MCP/LEDA and CEM. Results relative to the literature value are given in Fig. 33. Error bars are due to statistical errors ($< 3\%$) as well as calibration uncertainties of the detectors of 5%. With the exception of the measurement with the MCP/LEDA and 2 μA emission in LR all the measurements are in good agreement with the literature value. The isotopic ratios in LR depend strongly on the measurements in HR since the ratio of the species within one peak in LR is deduced from HR measurements because of the higher resolution. The peak of 22 u/e is due to ^{22}Ne and doubly charged CO_2, while they overlap in LR they can be easily resolved in HR. The proportion of ^{22}Ne to the total signal in this mass in HR was used to deduce the proportion of ^{22}Ne to the total peak in LR. The purity of the introduced gas with respect to possible contamination in the tubes is also important. However the purity of the introduced gas was 99.9998% while background measurements were performed for every detector and emission, and should therefore be neglected.

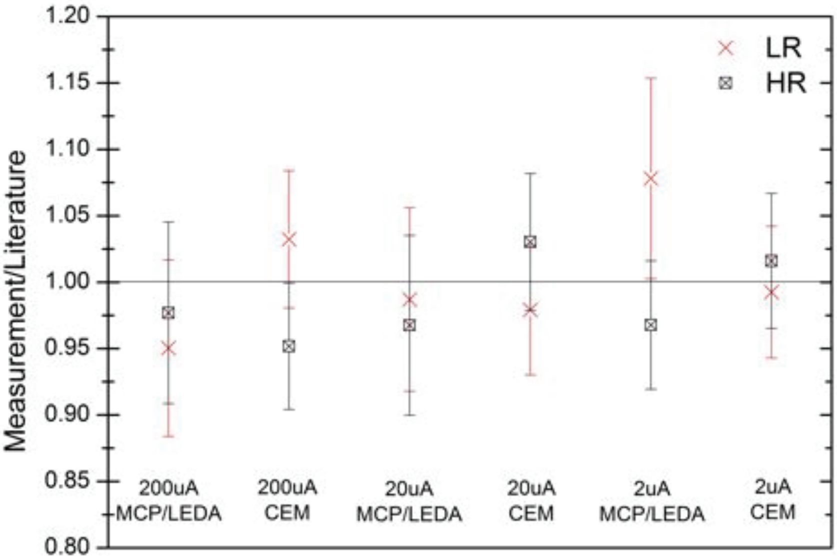

Figure 33: Comparison of DFMS isotopic measurements of $^{22}Ne/^{20}Ne$ with literature values for the MCP/LEDA and CEM for all emissions. The agreement between literature value and the measurements is with the exception of the LR measurement for the 2 μA with MCP/LEDA reasonable.

Table 13: Sensitivities of DFMS FM for Ne

Emission	MCP/LEDA	CEM	FC
	Ne Sensitivities for HR [cm^3]		
200 μA	3.548 x 10^{-20}	4.920 x 10^{-20}	4.496 x 10^{-20}
20 μA	1.008 x 10^{-19}	1.440 x 10^{-19}	N/A
2 μA	2.392 x 10^{-19}	2.964 x 10^{-19}	N/A
	Ne Sensitivities for LR [cm^3]		
200 μA	1.219 x 10^{-18}	1.197 x 10^{-18}	1.568 x 10^{-18}
20 μA	2.251 x 10^{-18}	2.093 x 10^{-18}	2.302 x 10^{-18}
2 μA	3.010 x 10^{-18}	2.705 x 10^{-18}	2.529 x 10^{-18}

Sensitivity measurements were performed in LR and HR for all detectors and emissions (see Tab. 13). The sensitivity is the average of the sensitivities for every pressure level. The sensitivity of one pressure level is calculated by the sensitivity for the main species (^{20}Ne) multiplied by the total abundance for all isotopes together (^{20}Ne: 100%, ^{21}Ne: 0.30%, ^{22}Ne: 10.22% [Handbook of Chemistry and Physics, 2012]). The pressure is species dependent and therefore corrected by a species dependent factor (correction factor for the pressure can be found in Appendix F). The high resolution mode is less sensitive compared to low resolution. A factor of ~14 between LR and HR can be explained by the resolution dependent slit. The CEM detector is more sensitive in HR than MCP/LEDA, while the FC is in good agreement with the CEM sensitivity. The sensitivity for the 200 μA emission mode is lower than 20 μA and 2 μA. This can be explained by higher space charge of the electrons around the filament, and therefore electrons are not guided as efficiently into the ionization region as for the other emissions (see Sec. 4.2). The sensitivity for high resolution for the FC detector at an emission of 20 μA and 2 μA was not applicable (N/A), since no signal peak could be detected.

The statistical error for the sensitivity measurement is $< 1\%$. The uncertainties of the pressure measurement are ~14% (see App. F). Calibration uncertainties of the MCP/LEDA such as gain calibration and individual pixel gain corrections are estimated as $\sim$ 7%. Calibration uncertainties of the CEM and the FC detector are assumed to be $\sim$ 5%. The total uncertainties for the sensitivity in HR are therefore: 16% for MCP/LEDA and 15% for CEM & FC. The evaluation of the proportion of the signal in LR is deduced from the HR spectra therefore an additional uncertainty ($\sim$ 5%) has to be taken into account, leading to slightly higher uncertainties. Uncertainties for the sensitivity in LR are therefore: 17% for MCP/LEDA and 16% for CEM & FC.

5.4.2 *Ar* Argon

Ar has been proposed to be detected in comets, but as mentioned above detection is still not completely confirmed. The GCU-gas of the ROSINA instruments do not contain *Ar* to avoid confusion in the measurements, although no background contamination due to the GCU-gas on the spacecraft could be detected. The background of Rosetta due to outgassing of the spacecraft contains C_2O at < 40 u/e, however the resolution of the instrument is high enough to resolve both compounds in HR.

The measurements for the calibration were performed on three different pressure levels (for *Ar* corrected pressure: 3 x 10^{-9} mbar, 8 x 10^{-9} mbar, 8 x 10^{-8} mbar). The measurements for *Ar* were performed manually for all detectors and emissions to reduce measurement time and avoid pixel gain corrections for the MCP/LEDA. The background pressure before measurements was at the level of ~5 x 10^{-10} mbar. The dependency between measured signal (^{40}Ar) with the MCP/LEDA and the pressure in the chamber can be found in Fig. 34. The statistical uncertainty of the signal is smaller than symbol size. The signal is linear with the pressure in the chamber while *Ar* gas was introduced into the chamber. The measurement for LR at 2 μA and HR at 20 μA overlap at the higher pressure levels but they do only partly overlap at the lowest pressure level (see Fig. 34). A possible explanation why they do only partly overlap at the lowest pressure level could be the statistical uncertainties or the uncertainties of the pressure measurement of 14% that is not plotted. The amount of ions that impinge on the detector at the same pressure level is clearly higher for low resolution than for high resolution.

The isotopic abundances for $^{36}Ar/^{40}Ar$ and$^{38}Ar/^{40}Ar$ for the MCP/LEDA and CEM for all emissions can be found in Fig. 35 (MCP/LEDA) and 36 (CEM). Both isotopes are $<$ 1% of ^{40}Ar and therefore require a good sensitivity and a dynamic range of $>10^3$. However with the exception of the 2 μA measurements of the CEM all the measured isotopic ratios are within error bars in good agreement with the literature value (see Fig. 35 and 36). Error bars are due to statistical errors (MCP: $< 8\%$ for $^{38}Ar/^{40}Ar$ and $< 4\%$ for $^{36}Ar/^{40}Ar$, CEM: $< 10\%$ for $^{38}Ar/^{40}Ar$ and $< 5\%$ for $^{36}Ar/^{40}Ar$) as well as calibration uncertainties of the

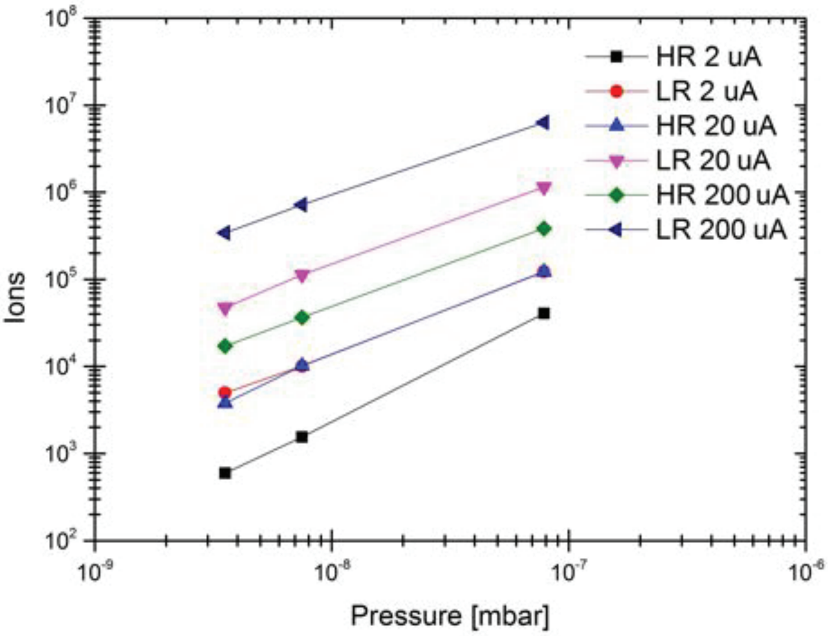

Figure 34: The linearity between measured signal and the pressure for Ar.

detectors (of 5%). To reduce pixel gain errors, the highest signal was always shifted to the same pixel for the MCP/LEDA.

Sensitivity measurements were performed in LR and HR for all detectors and emissions (see Tab. 14). The pressure is again corrected for Ar. The sensitivity is the average of the sensitivities for every pressure level. The sensitivity of one pressure level is calculated by the ion current for the main species (^{40}Ar) multiplied by the total abundance for all isotopes together (^{40}Ar: 100%, ^{36}Ar: 0.33785%, ^{38}Ar: 0.06345% [Handbook of Chemistry and Physics, 2012]) and the amount of doubly charged particles of ^{40}Ar of 0.35 %. The amount of doubly charged particles for noble gases is very low since noble gases are not likely to be multiply charged. An-other reason could be that the electron energy in the ion source is reduced to 45 eV. The sensitivities for the CEM detector are higher for Ar than those for the MCP/LEDA detector while the sensitivities for the FC are in agreement. A possible reason for this could be that the detection efficiency of the MCP/LEDA for Ar is lower than for the CEM. The emission of 20 μA and 2 μA is more sensitive than the 200 μA. The statistical error for the sensitivity measurement is $< 1\%$. The uncertainties of the pressure measurement are $\sim$14% (see App. F). Calibration uncertainties of the MCP/LEDA such as gain calibration is estimated as $\sim$ 5%. Calibration uncertainties of the CEM and the FC detector are assumed to be $\sim$ 5%. The total uncertainties for the sensitivity in HR are therefore: 16% for MCP/LEDA and 15% for CEM & FC. The evaluation of the proportion of the signal in LR is deduced from the HR spectra therefore an additional uncertainty ($\sim$ 5%) has to be taken into account, leading to slightly higher uncertainties. Uncertainties for the sensitivity in LR are therefore: 17% for MCP/LEDA and 16% for CEM & FC.

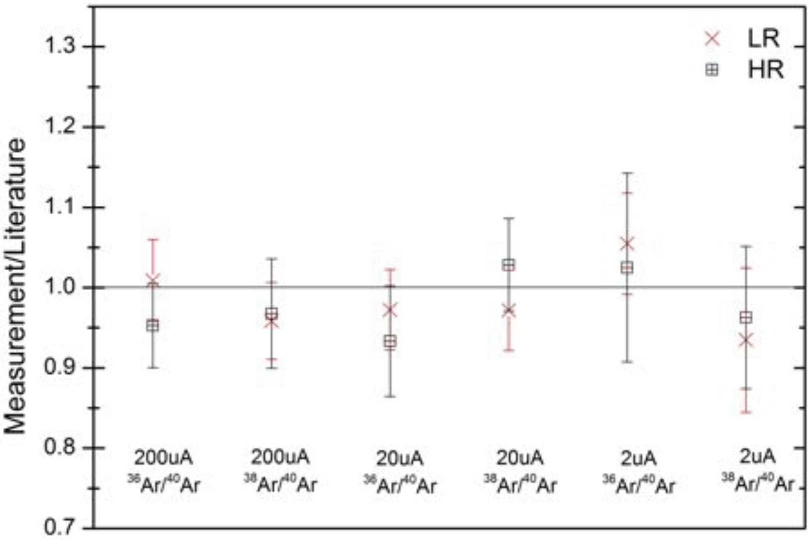

Figure 35: Comparison of DFMS isotopic measurements of $^{36}Ar/^{40}Ar$ and $^{38}Ar/^{40}Ar$ with literature values for the MCP/LEDA for all emissions. The agreement between literature value and the measurements is reasonable.

Table 14: Sensitivites of DFMS FM for Ar

Emission	MCP/LEDA	CEM	FC
	Ar Sensitivities for HR [cm^3]		
200 μA	2.047 x 10^{-19}	5.387 x 10^{-19}	5.539 x 10^{-19}
20 μA	5.484 x 10^{-19}	1.670 x 10^{-18}	1.110 x 10^{-18}
2 μA	6.589 x 10^{-19}	1.846 x 10^{-18}	1.243 x 10^{-18}
	Ar Sensitivities for LR [cm^3]		
200 μA	3.834 x 10^{-18}	8.250 x 10^{-18}	8.529 x 10^{-18}
20 μA	6.430 x 10^{-18}	1.357 x 10^{-17}	1.516 x 10^{-17}
2 μA	7.150 x 10^{-18}	1.535 x 10^{-17}	1.492 x 10^{-17}

5.4.3 Kr Krypton

The calibration measurements for Krypton were performed at one pressure level. Background contamination could be neglected since Krypton was not detected in the background measurements performed before introducing gas into the chamber. The pressure was corrected for Krypton and at 1 x 10^{-7} mbar while the background was 1 x 10^{-9} mbar. Previous krypton calibration measurements can also be found in Riesen (2007). The isotopic abundances of ^{78}Kr, ^{80}Kr, ^{82}Kr, ^{83}Kr and ^{86}Kr relative to the most abundant isotope ^{84}Kr for CEM and MCP/LEDA for 200 μA can be found in Fig. 38 (CEM) and 37 (MCP/LEDA). The measurements for the other emissions show a similar behavior as the 200 μA. All the abundances (^{78}Kr: 0.61%, ^{80}Kr: 4.0%, ^{82}Kr: 20.32%, ^{83}Kr : 20.16%, ^{84}Kr: 100% and ^{86}Kr: 30.35% [Handbook of Chemistry and Physics, 2012]) are within error bars in good agreement with the literature values. The statistical errors for the CEM and the MCP/LEDA are < 1%. Calibration uncertainties for the MCP/LEDA of < 5% and the

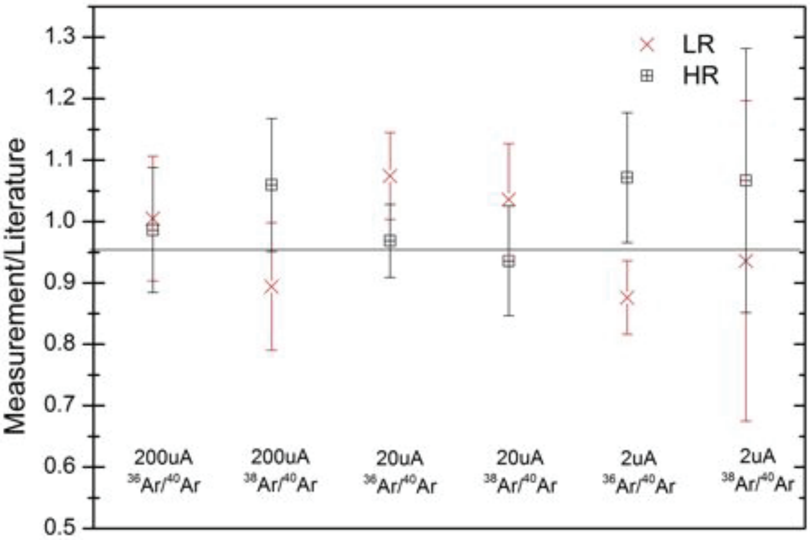

Figure 36: Comparison of DFMS isotopic measurements of $^{36}Ar/^{40}Ar$ and $^{38}Ar/^{40}Ar$ with literature values for the CEM for all emissions. The agreement between the literature values and the measurements are reasonable with the exception of the 2 μA $^{36}Ar/^{40}Ar$ measurements.

CEM of $< 5\%$ was taken into account. To avoid pixel gain corrections for the MCP/LEDA, measurements were performed manually to shift the highest signal always to the same pixel.

Table 15: Sensitivities of DFMS FM for Kr

Emission	MCP/LEDA	CEM	FC
	Kr Sensitivities for HR [cm^3]		
200 μA	4.042 x 10^{-19}	4.126 x 10^{-19}	3.775 x 10^{-19}
20 μA	9.235 x 10^{-19}	7.701 x 10^{-19}	N/A
2 μA	9.798 x 10^{-19}	1.009 x 10^{-18}	N/A
	Kr Sensitivities for LR [cm^3]		
200 μA	6.491 x 10^{-19}	6.367 x 10^{-18}	5.580 x 10^{-18}
20 μA	8.953 x 10^{-19}	7.362 x 10^{-18}	6.606 x 10^{-18}
2 μA	9.350 x 10^{-19}	9.643 x 10^{-18}	N/A

The sensitivity of all detectors and all emissions for Kr in LR and HR can be found in Tab. 15. The sensitivity of the MCP/LEDA and CEM is the total of all isotopic abundances for Kr and the amount of doubly charged particles (0.35 %) multiplied by the sensitivity of the most abundant isotope ^{84}Kr. The sensitivity of the FC and the CEM are in good agreement. However, no signal was detected for HR with an emission of 20 μA and 2 μA for the FC as well as for LR at 2 μA (N/A). The sensitivities for an emission of 200 μA is lower than for the other emissions. The sensitivity for high resolution for the MCP/LEDA is almost the same as for low resolution, even though the sensitivity of the CEM for low resolution is higher than for high resolution. This can be explained by the additional acceleration (post acceleration) of the ions towards the MCP for high resolution. Therefore the velocity of the

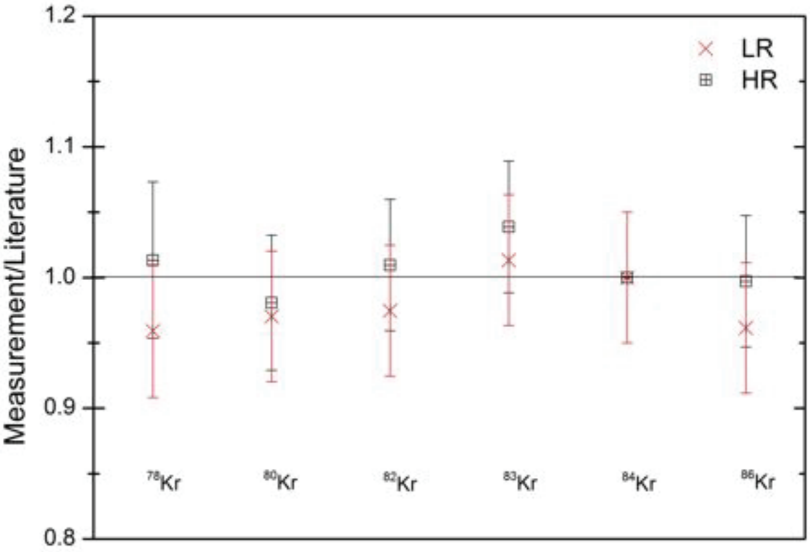

Figure 37: Comparison of DFMS isotopic measurements of $^{78}Kr/^{84}Kr$, $^{80}Kr/^{84}Kr$, $^{82}Kr/^{84}Kr$, $^{83}Kr/^{84}Kr$ and $^{86}Kr/^{84}Kr$ with literature values for the MCP/LEDA for 200 μA emissions. The agreement between literature value and the measurements is reasonable.

ions in high resolution is much higher when they impinge on the MCP than for low resolution. The secondary electrons emission yield of the MCP is species and energy dependent, and therefore the detection of the same species with a higher velocity is more efficient. The statistical error for the sensitivity measurement is $< 1\%$. The uncertainties of the pressure measurement are $\sim$14% (see App. F). Calibration uncertainties of the MCP/LEDA such as gain calibration is estimated as $\sim$ 5%. Calibration uncertainties of the CEM and the FC detector are assumed to be $\sim$ 5%. The total uncertainties for the sensitivity in HR are therefore: 16% for MCP/LEDA and 15% for CEM & FC. The evaluation of the proportion of the signal in LR is deduced from the HR spectra therefore an additional uncertainty ($\sim$ 5%) has to be taken into account, leading to slightly higher uncertainties. Uncertainties for the sensitivity in LR are therefore: 17% for MCP/LEDA and 16% for CEM & FC.

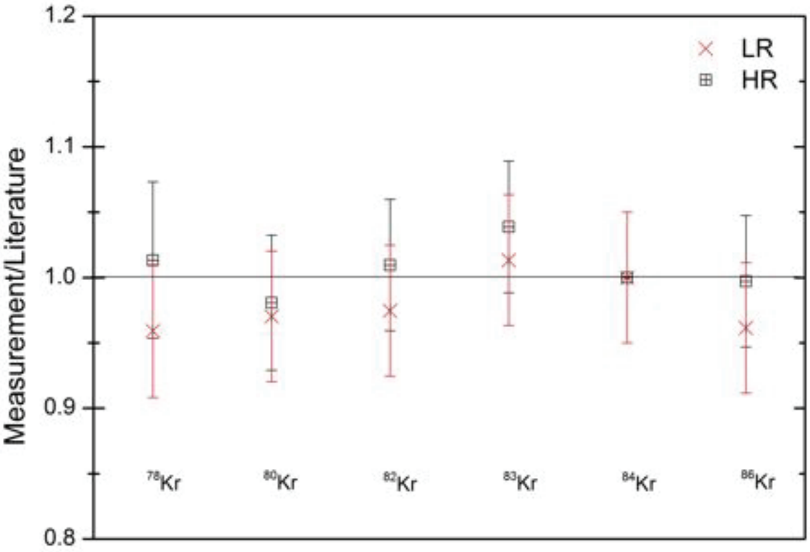

Figure 38: Comparison of DFMS isotopic measurements of $^{78}Kr/^{84}Kr$, $^{80}Kr/^{84}Kr$, $^{82}Kr/^{84}Kr$, $^{83}Kr/^{84}Kr$ and $^{86}Kr/^{84}Kr$ with literature values for the CEM for 200 μA emissions. The agreement between literature value and the measurements is reasonable.

5.4.4 Xe Xenon

Xenon is the heaviest of the noble gases. The GCU-gas of DFMS contains Xenon for calibration. However a possible detection of Xenon in the comet's coma is feasible.
The calibration measurements for Xenon were performed at one pressure level for all emissions and detectors. Background contamination could be neglected since Xenon was not detected in the background measurements performed before introducing gas into the chamber. The pressure was corrected for Xenon and at 3.5 x 10^{-8} mbar (for correction factor see App. F) while the background was 5 x 10^{-10} mbar. The calibration measurements were performed manually, since the nominal scan modes for high resolution only cover the mass range 13 u/e (12 u/e for CEM) to 100 u/e and therefore don't cover the masses of Xenon. The detection of all Xenon isotopes was difficult for isotopes with low abundances. If the signal is very low it is recorded on GS 16 with a maximal detector gain. The signal of Xe disappears in high resolution for the maximal detector gain (GS 16) if a front voltage of -2500 V is applied on the MCP. For all other gain settings this is not true if the number of ions impinging on the MCP is high enough that they are detected at lower gains (GS $<$ 16). The maximum gain was therefore avoided during measurements with the MCP/LEDA.

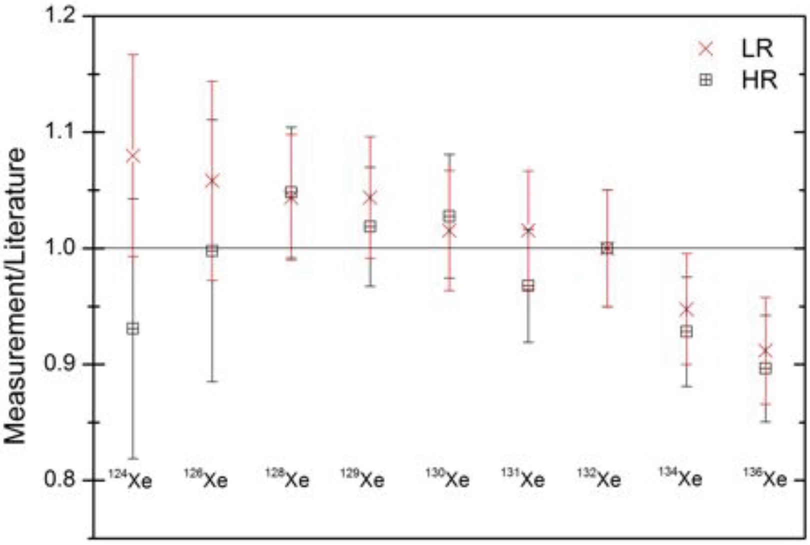

Figure 39: Comparison of DFMS isotopic measurements of ^{124}Xe, ^{126}Xe, ^{128}Xe, ^{129}Xe, ^{130}Xe, ^{131}Xe, ^{132}Xe, ^{134}Xe and ^{136}Xe (relative to the most abundant isotope ^{132}Xe) with literature values for the MCP/LEDA for 200 μA emissions. The agreement between literature value and the measurements is reasonable for the lighter ions, however it does not agree for the two heaviest ions ^{134}Xe and ^{136}Xe. A possible explanation can be found in the text.

The isotopic abundances of all isotopes for an emission of 200 μA for the MCP/LEDA and the FC (LR) can be found in Fig. 39 (MCP/LEDA) and 40 (FC). The isotopic abundances for the lighter ions (^{124}Xe, ^{126}Xe, ^{128}Xe, ^{129}Xe, ^{130}Xe, and ^{131}Xe) relative to the most abundant isotope ^{132}Xe detected with the MCP/LEDA are in good agreement with the literature values. However the isotopic abundance of the heavier ions ^{134}Xe and ^{136}Xe does not fit the literature value. A possible explanation could be that the velocities of these heavy ions are lower than for the lighter ions because of the almost (mass dependent) acceleration voltage (V_{accel}) and therefore the heavy ions don't release the same amount of electrons while impinging on the MCP. In low resolution this seems to be even more obvious since the abundance of the isotopes relative to the literature value decreases with mass. This effect can be avoided by measuring the ratios with the other two detectors since they are not velocity-sensitive. Therefore the isotopic abundances were measured with the FC and the CEM. To show the capabilities of the FC the isotopic abundances in LR can be found in Fig. 40. The isotopic abundances of ^{128}Xe, ^{129}Xe, ^{131}Xe, ^{134}Xe and ^{136}Xe are within error bars in good agreement with the literature value. Uncertainties are due to statistics ($< 4\%$) and calibration of the detector (5%). However the isotopic abundance of ^{124}Xe, ^{126}Xe and ^{130}Xe does not fit the literature value. An explanation for the less abundant isotopes could be that their signal is below the detection limit of the FC, and might therefore be overestimated, leading to abundances that are too high. The fact that the more abundant isotopic ratio for ^{130}Xe does not fit the literature value could also indicate that the estimated calibration error for the FC of 5% might be underestimated. However since the FC is designed for instrument internal calibration and not to measure isotopic abundances, the calibration error is of minor interest.

Sensitivity measurements were performed in LR and HR for all detectors and emissions for

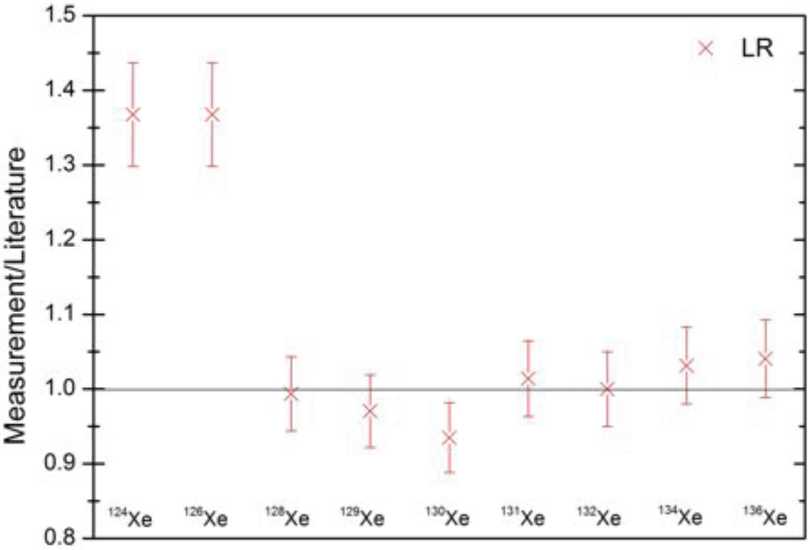

Figure 40: Comparison of DFMS isotopic measurements of ^{124}Xe, ^{126}Xe, ^{128}Xe, ^{129}Xe, ^{130}Xe, ^{131}Xe, ^{132}Xe, ^{134}Xe and ^{136}Xe (relative to the most abundant isotope ^{132}Xe) with literature values for the FC for 200 μA emissions in low resolution. The agreement between literature value and the measurements is reasonable with the exception of the less abundant isotopes ^{124}Xe, ^{126}Xe and ^{130}Xe. A possible explanation can be found in the text.

one pressure level (see Tab. 16). The sensitivity is calculated by the signal for the main species (^{132}Xe) multiplied by the total abundance for all isotopes together (^{124}Xe: 0.335%, ^{126}Xe: 0.335%, ^{128}Xe: 7.14%, ^{129}Xe: 98.33%, ^{130}Xe: 15.17%, ^{131}Xe: 78.77%, ^{132}Xe: 100%, ^{134}Xe: 38.82%, and ^{136}Xe: 32.99% [Handbook of Chemistry and Physics, 2012]) and the amount of doubly charged particles of ^{132}Xe of 1.30%. The pressure measurements are corrected for Xe. The CEM detector is more sensitive for Xe than the MCP/LEDA detector while the FC is as sensitive as the CEM. No signal could be detected for the FC at 2 μA at either resolution nor for high resolution at an emission of 20 μA and therefore these sensitivities are not applicable (N/A). The emission of 20 μA and 2 μA is more sensitive than the 200 μA. The ratio between the sensitivity of the MCP/LEDA for high and low resolution is almost one. This can be explained by the fact that an additional potential is applied in HR and therefore the ions impinging on the MCP release more electrons. The statistical error for the sensitivity measurement is $< 1\%$. The uncertainties of the pressure measurement are $\sim$14% (see App. F). Calibration uncertainties of the MCP/LEDA such as gain calibration and individual pixel gain corrections are estimated as $\sim$ 7%. Calibration uncertainties of the CEM and the FC detector are assumed to be $\sim$ 5%. The total uncertainties for the sensitivity in HR and LR are therefore: 16% for MCP/LEDA and 15% for CEM & FC. Since the signal of the peaks in HR only contains Xenon no additional uncertainties were applied for LR.

Table 16: Sensitivities of DFMS FM for Xe

Emission	MCP/LEDA	CEM	FC
	Xe Sensitivities for HR [cm^3]		
200 μA	1.559 x 10^{-19}	2.580 x 10^{-19}	3.040 x 10^{-19}
20 μA	2.414 x 10^{-19}	4.180 x 10^{-19}	N/A
2 μA	2.721 x 10^{-19}	5.250 x 10^{-19}	N/A
	Xe Sensitivities for LR [cm^3]		
200 μA	3.413 x 10^{-19}	1.020 x 10^{-17}	1.520 x 10^{-17}
20 μA	3.379 x 10^{-19}	9.790 x 10^{-18}	2.020 x 10^{-17}
2 μA	3.571 x 10^{-19}	1.230 x 10^{-17}	N/A

5.5 H_2O Water

This chapter is partly published as an article in PSS [Hässig et al., 2013] and some discussions are very detailed.

Water is one of the prime ingredients required for life. As such it is one of the major foci of past and current space missions including missions to Mars (Viking and Mars Express), to the Jupiter system with its icy moons (JUNO and JUICE), as well as missions to the poles of the moon. In the case of terrestrial water it is believed that Earth was once dry. It has been argued that some terrestrial water could have originated in hydrous minerals that were present during the early accretion phase of the Earth and the presence of these minerals helps explain different aspects of Earth's geochemistry. However, these minerals must have formed locally; this would imply that the nebula must have been cooler than the models predict [Cisela and Lauretta, 2005]. Therefore, at least part of the water must have originated from other places in the solar system [Oró, 1961]. Primary suspects are asteroids and comets. On the one hand, asteroids are suspect in particular due to the detection of carbon-rich meteorites that have deuterium to hydrogen (D/H) ratios similar to the value found in the Earth's oceans. The Nice model [Gomes et al., 2005, Tsiganis et al., 2005, Morbidelli et al., 2005], postulates that the gas giant planets underwent orbital migration and forced objects in the asteroid belt and/or Kuiper belt on eccentric orbits that put them in the path of the terrestrial planets. During this late heavy bombardment comets might have brought water to Earth and Mars.

On the other hand, the role of comets as a source of water on Earth was long questioned, or at least thought to be of limited importance. The observed D/H ratios of several Oort cloud comets, such as Halley [Balsiger et al., 1995, Eberhardt et al., 1995], Hale-Bopp [Meier et al., 1998a, Meier et al., 1998b], Hyakutake [Bockelée-Morvan et al., 1998] and 2001 Q4 NEAT [Weaver et al., 2008], were clearly higher than the Standard Mean Ocean Water (SMOW[f]) D/H ratio of (1.558 ± 0.001) x 10^{-4} on Earth. The D/H ratio in three samples from Wild 2 show even enrichment of up to three times the terrestrial value. Recent remote sensing measurements of a Jupiter-family comet, 103P/Hartley 2, by the Herschel Space Observatory of $HD^{16}O$ and $H_2^{18}O$ found an ocean-like water ratio for D/H of (1.61 ± 0.24) x 10^{-4} [Hartogh et al., 2011]. In these measurements the ratio of $^{18}O/^{16}O$ was assumed to be solar. Hence Jupiter-family comets, believed to originate in the Kuiper belt, could present, another possible source for the water on Earth and Mars. However, so far, the D/H ratio

---

[f] [Handbook of Chemistry and Physics, 2012]

for water could not be measured directly without at least the assumption of the $^{18}O/^{16}O$ ratio. This is the only D/H measurement in a Jupiter family comet. Nothing is known about the diversity among this group of comets. In addition, only four Oort cloud comets are fairly small sample. Comet 67P/Churyumov-Gerasimenko, the target of the European Space Agency's Rosetta mission, most probably also originates from the Kuiper belt region. Rosetta will accompany the comet over an extended period of time. The rendezvous with the comet will take place well beyond 3 AU and from then on Rosetta will perform observations along its inward journey to characterize the physical, chemical, and morphological characteristics of the nucleus and the surrounding coma including neutral gas, dust, and plasma. In comparison to the to date only *in situ* measurements in a comet coma, the result of DFMS should be clearly superior: The ion mass spectrometers on the Giotto spacecraft had limited resolution and the D/H ratio was determined from the hydronium ion and not from the water molecules directly [Balsiger et al., 1995, Eberhardt et al., 1995]. No attempts were made so far to determine the oxygen isotopes in water in comets apart from the very coarse determination by the Ion Mass Spectrometer - High Intensity Sensor (IMS-HIS) on Giotto [Balsiger et al., 1995] which resulted in a solar value for $^{18}O/^{16}O$ with a large uncertainty. Therefore the observations by ROSINA at comet 67P/Churyumov-Gerasimenko are an important step in confirming (or dismissing) the role of Kuiper belt objects as a major source of the water on Earth.

The calibration measurements for H_2O were performed for all detectors and all emissions at one pressure level. The pressure corrected for water was ~ 1 x 10^{-7} mbar while background pressure was 5 x 10^{-10} mbar. CASYMIR was heated during the measurements to avoid a water contamination of the chamber. Therefore the exact pressure measurements of the background might be underestimated. To put water into the chamber a gas bottle containing an amount of distilled water (1/10 of the volume) was pumped and the resulting water vapor introduced into the chamber. The bottle contained an amount of air that was removed by pumping the bottle efficiently before mounting. However since the pressure inside the bottle was lower than air pressure, some air could have leaked into the bottle during measurements, although during pumping no leak could be detected.

The fragmentation measurements of H_2O for the MCP/LEDA and the CEM can be found in Fig. 41. The fragmentation measurements were not performed for the FC since it is expected that the detection efficiency for different species of the FC is comparable to that of the CEM. For comparison the values from NIST[g] and two other sources (Rao et al. (1995) and Orient and Srivastava (1987)) are given. The fragmentation pattern measured with DFMS FM is almost comparable with the values given in NIST (and Rao et al. (1995)). However, the electron energy of DFMS is reduced and therefore more signal due to the *parent* is expected. In Rao et al. (1995) the ionization cross section for 45 eV for H_2O^+, OH^+, and O^+ is given while the fragmentation pattern is calculated relative to the H_2O^+. This fragmentation is almost comparable to the fragmentation measured with DFMS FM. In Orient (1987) the ionization cross section for 40 eV and 50 eV for H_2O^+, OH^+, and O^+ is given, therefore the values were first interpolated and then the fragmentation pattern calculated relative to the H_2O^+. This fragmentation pattern is clearly not in agreement with the measured fragmentation of DFMS FM. Lots of different values can be found in the literature as the two examples show, although non of them really represents the measurements with DFMS

---

[g] If NIST is referenced, data is from *http : //webbook.nist.gov/chemistry/* from *Mass spectrum*. All tough different values were found during several accessed from 05.02.2012-01.06.2013, the values are given as a reference to state clearly, that the fragmentation pattern must be calibrated for every compound for DFMS.

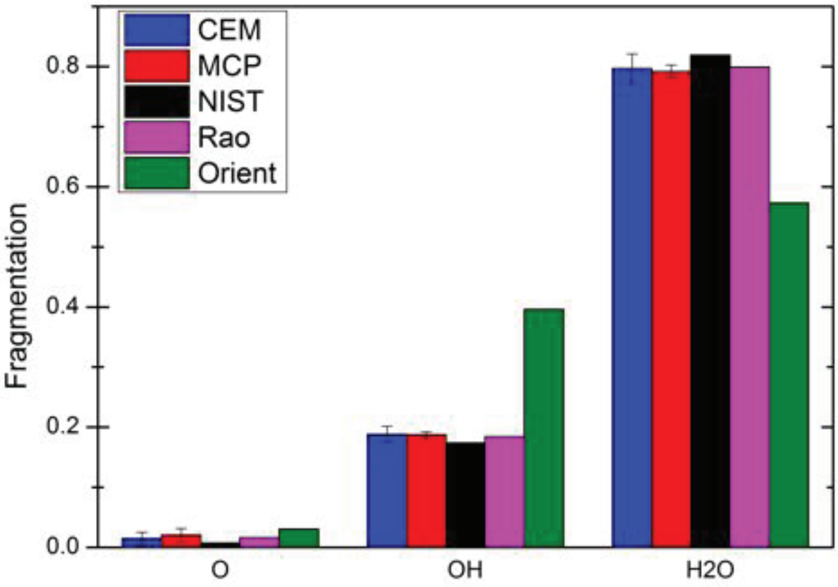

Figure 41: The fragmentation pattern for H_2O measured with DFMS FM for MCP/LEDA and CEM. For comparison NIST[4], Rao 1995 and Orient 1987 is given. Although for the latter two the electron energy of 45 eV was taken into account, they are not in agreement with the measurements of DFMS FM. Uncertainties of the measurements are due to average for all emissions.

FM. Therefore the instrument characteristic fragmentation pattern has to be measured. The isotopic abundances measured for H_2O are discussed one by one, and a summary can be found in Tab. 17:

Table 17: Isotopic ratio and abundances of D/H and the oxygen isotope measured with MCP/LEDA.

Isotopic ratio	Molecules	Results	Literature*
D/H	$HD^{16}O/H_2^{16}O$	(1.68 ± 0.15) x 10^{-4}	1.56 x 10^{-4}
D/H	$HD^{18}O/H_2^{18}O$	(1.47 ± 0.12) x 10^{-4}	1.56 x 10^{-4}
$^{17}O/^{16}O$	$H_2^{17}O/H_2^{16}O$	(4.00 ± 0.36) x 10^{-4}	3.81 x 10^{-4}
$^{18}O/^{16}O$	$^{18}OH/^{16}OH$	(2.02 ± 0.12) x 10^{-3}	2.05 x 10^{-3}
$^{18}O/^{16}O$	$H_2^{18}O/H_2^{16}O$	(2.09 ± 0.19) x 10^{-3}	2.05 x 10^{-3}
$^{16}OD/^{17}OH$	$HD^{16}O/H_2^{17}O$	0.416 ± 0.029	0.409

*[Handbook of Chemistry and Physics, 2012]

There are two ways to measure the D/H ratio for water: One is to derive the ratio from $HD^{16}O$ and $H_2^{16}O$. On the mass line 19 u/e there are $HD^{16}O$, $H_2^{17}O$, and ^{18}OH. The latter two can be easily resolved in the high-resolution mode, while $HD^{16}O$ and $H_2^{17}O$ still partly overlap at the resolution of DFMS (see Fig. 42). Nevertheless, the two overlapping peaks can easily be resolved because of the well-defined shape and separate peak of ^{18}OH on the same spectra. The two overlapping peaks are clearly wider than the single peak. The peak of ^{18}OH was fitted with a Gaussian shape and the full width half maximum (FWHM) from this peak was taken for the fit of the two overlapping peaks. The only remaining parameters needed to fit the two overlapping peaks are the corresponding amplitudes.

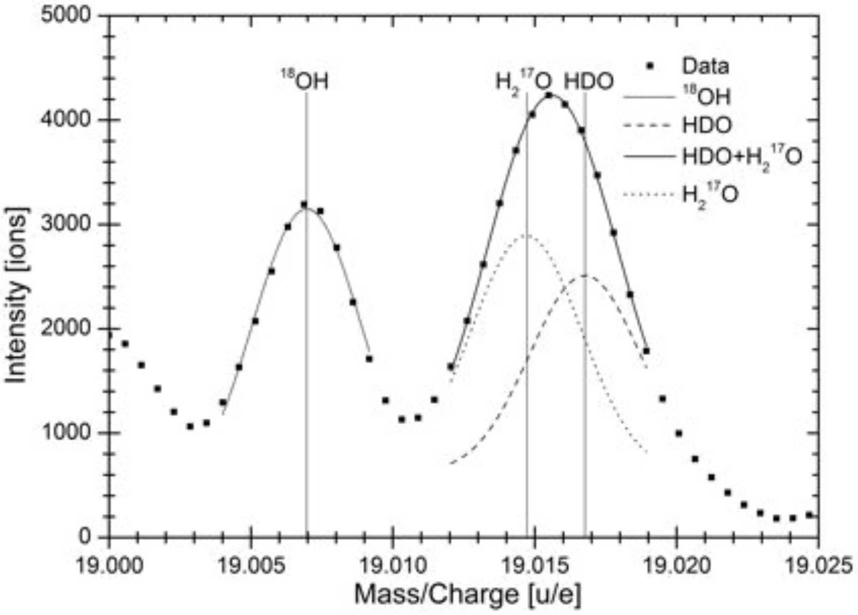

Figure 42: MCP/LEDA HR spectrum of mass 19 u/e, whereas $H^{18}O$ is clearly separated from $H_2^{17}O$ and $HD^{16}O$. The Full Width at Half Maximum (FWHM) of the peak to the right is significantly broader than that for $H^{18}O$ and implies two overlapping peaks. To resolve the latter, two Gaussian fits were applied; taking the FWHM from $H^{18}O$ as fixed for all three mass peaks and the amplitudes of $H_2^{17}O$ and $HD^{16}O$ as the free parameters to be fitted.

The other clever measurement is to deduce the D/H ratio from rarer isotopes such as $H_2^{18}O$ and $HD^{18}O$. On the 21 u/e mass line there is no signal from any other molecule except $HD^{18}O$ with a very minor contribution of $D_2^{17}O$ ($< 10^{-4}$ relative to $HD^{18}O$ [Handbook of Chemistry and Physics, 2012]). So there is no need for the high-resolution mode to resolve individual species and the measurement can be performed in the more sensitive low-resolution mode. Note that in low-resolution mode, $H_2^{18}O$ on the 20 u/e mass line competes with FH (fluorine and FH are part of the background, mostly due to vacuum grease, e.g. Braycote [Schläppi et al., 2010]). The ratio $H_2^{18}O/H^{19}F$ however, can be derived from the high-resolution mode, where $H^{19}F$ can easily be separated from $H_2^{18}O$.
The isotopic ratio deduced from mass line 18 u/e and 19 u/e are measured in high resolution and therefore not on the same spectrum, which results in a calibration error due to different DFMS MCP/LEDA detector gain (5%). Other uncertainties are due to statistical errors and the mathematical fit (7%) to resolve $HD_{16}O$ from $H_2^{17}O$ (see Fig. 42). This results in a total uncertainty of $\sim$ 9%. For the ratio of $H_2^{18}O/HD^{18}O$ the measurements were performed in low resolution, taking advantage of higher sensitivity of the instrument as well as the advantage of having both peaks on the same spectrum to avoid calibration errors from the detector gain. Because of the limited dynamic range for one single spectrum, the peak of the more abundant isotope is in saturation and has to be fitted. The total uncertainty of $\sim$ 8% contains the uncertainty of the fit and the statistical uncertainties (7%) of the HR

spectrum required to deduce the ratio of $H_2^{18}O$ to FH on the mass 20 u/e.
The uncertainties of $H_2^{17}O/H_2^{16}O$ (see Fig. 42) have the same causes as the measurements of $HD^{16}O/H_2^{16}O$ and therefore a total of $\sim$ 9%.
The only measurement of the relative abundance of oxygen isotopes in the coma of a comet is the ratio of $^{18}O/^{16}O$ measured at Halley. As is the case for the D/H ratio the only *in situ* measurements are from the Giotto flyby where a telluric ratio was found with IMS-HIS to be $(1.93 \pm 0.12) \times 10^{-3}$ [Balsiger et al., 1995] and the Neutral Mass Spectrometer to be $(2.13 \pm 0.18) \times 10^{-3}$ [Eberhardt et al., 1995]. Remote sensing measurements of the Halley coma are in line with these *in situ* measurements and are within error bars compatible with the ratio on Earth. The *in situ* measurements with DFMS at comet 67P/Churyumov-Gerasimenko will not only provide the $^{18}O/^{16}O$ ratio but furthermore enable a unique opportunity to directly measure the $^{17}O/^{16}O$ ratio. The $^{17}O/^{16}O$ ratio can be derived from mass 19 u/e in the same way as the D/H ratio with a well defined mathematical fit. The oxygen isotopic ratio $^{18}O/^{16}O$ can be measured twice; once for $H_2^{18}O/H_2^{16}O$ and once for $H^{18}O/H^{16}O$. For the second ratio, the individual instrumental fragmentation pattern of water has to be well calibrated to adapt the ratio of hydroxyl to water.
Hydroxyl is clearly separated from Ammonia in HR. The same is true for ^{18}OH from $HD^{16}O$ and $H_2^{17}O$; therefore the remaining uncertainties are due to gain calibration (5%) and statistical errors (1%). This results in a total uncertainty of $\sim$ 6%. $H_2^{18}O$ and FH on mass line 20 u/e partly overlap at the base of the line but are clearly separated at the peak. To resolve the two peaks, a mathematical fit was applied. The total error of $\sim$ 9% is due to detector gain (5%), statistics and mathematical fit (7%), whereas on mass line 18 u/e the contribution of ^{18}O, ^{17}OH, and ^{16}OD can be neglected since their abundance is in the order of $< 10^{-4}$ compared to $H_2^{18}O$ [Handbook of Chemistry and Physics, 2012].
The sensitivity measurements were performed for all detectors and emissions. The total signal for the sensitivity contains the signal of H_2O, the signal of all fragments (O, OH) and the signal of all isotopes. The sensitivity for the MCP/LEDA and CEM for 200 μA is lower than for the other emissions. The sensitivity for the FC is in good agreement with that of the CEM, however no signal could be detected for the FC for 20 μA and 2 μA. The factor between 200 μA and 2 μA is much lower than for other compounds. A possible reason for this could be that the background pressure was underestimated for this measurement since CASYMIR was heated during these measurements and therefore more background material could be released from the walls. An other explanation could be that the bottle, although pumped efficiently before the measurement contained still some air. Therefore the sensitivity of the measurements of 200 μA might be underestimated and evaluation of the data using this number should be analyzed carefully.
The statistical error for the sensitivity measurement is $<$ 1%. The uncertainties of the pressure measurement are $\sim$14% (see App. F). Calibration uncertainties of the MCP/LEDA such as gain calibration and individual pixel gain corrections are estimated as $\sim$ 7%. Calibration uncertainties of the CEM and the FC detector are assumed to be $\sim$ 5%. The total uncertainties for the sensitivity in HR are therefore: 16% for MCP/LEDA and 15% for CEM & FC. The evaluation of the proportion of the signal in LR is deduced from the HR spectra therefore an additional uncertainty ($\sim$ 5%) has to be taken into account, leading to slightly higher uncertainties. Uncertainties for the sensitivity in LR are therefore: 17% for MCP/LEDA and 16% for CEM & FC.
The measurement of D/H can be done within one single spectrum and therefore an integration time of only 20 s is needed at a water vapor pressure of 3.0×10^{-7} mbar. For comparison: at the comet at 3 AU, and to reduce statistical errors below the 5% level measuring the iso-

Table 18: Sensitivities of DFMS FM for H_2O

Emission	MCP/LEDA	CEM	FC
	H_2O Sensitivities for HR [cm^3]		
200 μA	2.308 x 10^{-19}	1.337 x 10^{-19}	1.282 x 10^{-19}
20 μA	1.396 x 10^{-18}	8.944 x 10^{-19}	N/A
2 μA	1.151 x 10^{-18}	1.138 x 10^{-18}	N/A
	H_2O Sensitivities for LR [cm^3]		
200 μA	5.092 x 10^{-18}	3.295 x 10^{-18}	4.636 x 10^{-18}
20 μA	1.823 x 10^{-17}	1.327 x 10^{-17}	N/A
2 μA	1.402 x 10^{-17}	1.069 x 10^{-17}	N/A

topic ratio requires the accumulation of 256 spectra with an ion source emission current of 200 μA, or a total integration time of 5120 s, assuming a modeled water number density at 3 AU of 4 x 10^6 cm^{-3} at 20 km above the surface of 67P/Churyumov-Gerasimenko. The density is derived with an interpolated molecule flux of 1025 molecules/s [Tenishev et al., 2008]. With the assumption of a spherically outgassing comet and at a temperature of 180 K that results in a mean velocity of 460 m/s for water molecules.

5.6 N_2 Nitrogen

The abundance of N_2 in the coma of comets is an ongoing process, since the signal of N_2 and CO can be found on the same mass (28 u/e) for mass spectrometers. However an upper limit for N_2/H_2O of ≤ 0.1 was found for comet Halley [Eberhardt et al., 1988]. Isotopic ratios for $^{14}N/^{15}N$ are not deduced directly for N_2 but in comet Hale-Bopp for CN [Arpigny et al., 2003] and HCN [Ziurys et al., 1999], while the later measurement is compatible with the terrestrial value of 273 [Handbook of Chemistry and Physics, 2012]. The first measurement indicates an unidentified additional source of CN since the isotopic ratio of $^{14}N/^{15}N$ is 140 ± 35 and not compatible with the terrestrial value. A reevaluation of the ratios found that value for CN and HCN are both not compatible with the terrestrial value [Bockelée-Morvan et al., 2008]. In addition the ratios measured for Jupiter family comet 17P/Holmes is not compatible with the terrestrial value [Bockelée-Morvan et al., 2008]. These results indicate that HCN is the *parent* of CN in cometary atmospheres. The higher abundance of ^{15}N compared to Earth atmosphere indicates an isotopic fractionation of the N volatiles in the solar nebula during formation of the solar system [Bockelée-Morvan et al., 2008]. This indicates that there was no isotropically equilibration between the main nitrogen reservoir in the solar system and the HCN molecules before they were incorporated in Oort Cloud and Kuiper Belt comets.

The calibration measurements for N_2 were performed for all detectors and all emissions at one pressure level (1 x 10^{-7} mbar with a background pressure of 4 x 10^{-10} mbar). A correction factor for the pressure was not applied since the pressure measurements are calibrated for N_2. The calibration measurements are performed manually to reduce pixel gain correction.

The isotopic abundances for $^{15}N/^{14}N$ for $^{15}N^{14}N/^{14}N_2$ measured with the MCP/LEDA detector for all emissions can be found in Fig. 43. The measurements for HR and LR are within uncertainties comparable with the literature value. Error bars are due to statistical uncertainties ($<$ 2%) and calibration uncertainties of the MCP/LEDA (5%). An other

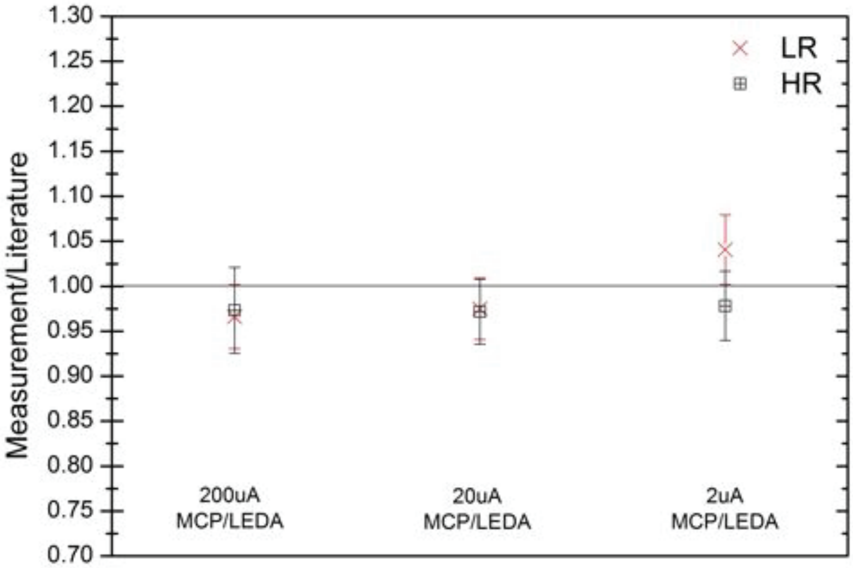

Figure 43: Comparison of the DFMS measurements for $^{15}N/^{14}N$ with literature value for the MCP/LEDA. $^{15}N/^{14}N$ ratio is measured for $^{15}N^{14}N$ relative $^{14}N_2$.

possibility is to deduce the isotopic abundance on the fragment ^{14}N of $^{14}N_2$ and the isotope ^{15}N. On mass 15 u/e the peaks of ^{15}N, ^{14}NH, $^{12}CH_3$ are well separated in HR the same is true for ^{14}N and CH_2. This was tested for the MCP/LEDA for an emission of 200 μA in HR and the ion current of ^{15}N was 0.34% of ^{14}N within uncertainties due to statistics of 2% and calibration of 5% the measurement is in agreement with literature (0.369% [Handbook of Chemistry and Physics, 2012]).

Table 19: Sensitivities of DFMS FM for N_2

Emission	MCP/LEDA	CEM	FC
	N_2 Sensitivities for HR [cm^3]		
200 μA	1.989 x 10^{-19}	2.193 x 10^{-19}	1.783 x 10^{-19}
20 μA	6.797 x 10^{-19}	8.486 x 10^{-19}	6.900 x 10^{-19}
2 μA	8.643 x 10^{-19}	1.713 x 10^{-18}	1.393 x 10^{-18}
	N_2 Sensitivities for LR [cm^3]		
200 μA	5.061 x 10^{-18}	5.682 x 10^{-18}	6.240 x 10^{-18}
20 μA	1.018 x 10^{-17}	1.172 x 10^{-17}	1.287 x 10^{-17}
2 μA	1.046 x 10^{-17}	1.740 x 10^{-17}	1.911 x 10^{-17}

Sensitivity measurements were performed in LR and HR for all detectors and emissions for one pressure level (see Tab. 19). The total signal includes isotopic abundances ($^{14}N/^{14}N$: 100%, $^{15}N/^{14}N$:0.37%) and the signal on 14 u/e for the fragment and the doubly charged N_2 of ∼5%. The sensitivity for an emission of 200 μA is lower than the other emissions for all detectors. The sensitivity for the FC is slightly lower than for the CEM. The statistical error for the sensitivity measurement is $< 1\%$. The uncertainties of the pressure measurement are ∼14% (see App. F). Calibration uncertainties of the MCP/LEDA such as gain calibration

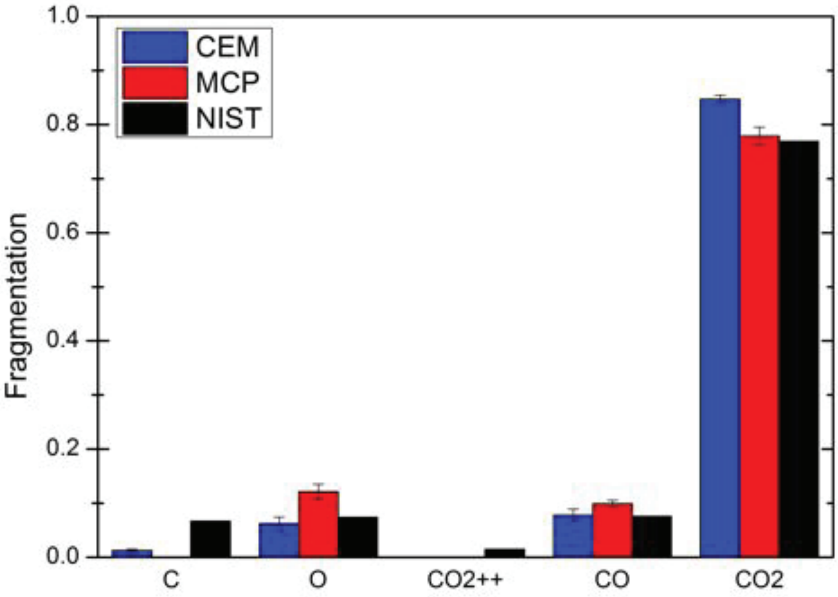

Figure 44: Fragmentation pattern for CO_2 for the MCP/LEDA and the CEM compared to NIST.

and individual pixel gain corrections are estimated as ∼ 7%. Calibration uncertainties of the CEM and the FC detector are assumed to be ∼ 5%. The total uncertainties for the sensitivity in HR are therefore: 16% for MCP/LEDA and 15% for CEM & FC. The evaluation of the proportion of the signal in LR is deduced from the HR spectra therefore an additional uncertainty (∼ 5%) has to be taken into account, leading to slightly higher uncertainties. Uncertainties for the sensitivity in LR are therefore: 17% for MCP/LEDA and 16% for CEM & FC.

5.7 CO_2 Carbon dioxide

The presence of CO_2 in cometary coma was indirectly established long time ago from the existence of CO_2^+ ions in the cometary tail [Feldman et al., 2004]. The production rate of CO_2 relative to H_2O for comet Hale-Bopp was more than 20%, however there exist only observations for r > 2.9 AU for this comet. The production rate for CO_2 for 1P/Halley was 3–4% and for 103P/Hartley was 8–10% [Bockelée-Morvan et al., 2004]. The higher production rate of Hale-Bopp can be explained by the higher volatility of CO_2 compared to H_2O at that distance from the Sun. The isotopic ratios in comets for C and O are not deduced from CO_2 nor fragments thereof.

The calibration measurements for CO_2 were performed for all detectors and all emissions at one pressure level. The background pressure was 8 x 10^{-10} mbar and the pressure corrected for CO_2 while gas was introduced was 7 x 10^{-8} mbar. The calibration measurements were performed with measurement modes for the MCP/LEDA and CEM detector while for the FC the measurements were performed manually. There exist special calibration modes for CO_2, however since this modes do not measure isotopic ratios of the fragments (17 u/e, 18 u/e and 29 u/e), scan modes for LR and HR were used.

The fragmentation pattern for CO_2 for the MCP/LEDA and the CEM compared to NIST can be found in Fig. 44. Uncertainties are due to average values for all emissions. The fragmentation pattern for the CEM is higher for the *parent* than the NIST, and therefore less for the fragments. This can be explained by the lower electron energy in the ion source. The fragmentation pattern of the MCP/LEDA is not the same as for the CEM. This can be explained by the detection efficiency of the MCP. However since the mass range of the MCP/LEDA does not cover 12 u/e the fragment C is not taken into account for the MCP/LEDA.

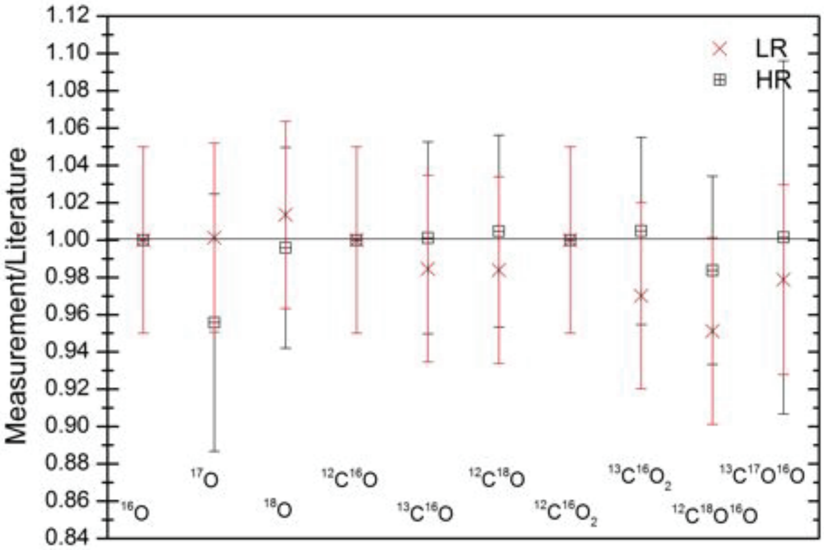

Figure 45: The measured isotopic ratios of CO_2 with the MCP/LEDA for an emission of 200 μA relative to literature value.

The isotopic abundances of CO_2 measured with the MCP/LEDA with an emission of 200 μA can be found in Fig. 45. All isotopic abundances are within uncertainties in good agreement with the literature value. Uncertainties are due to statistical errors and calibration errors of the detector of 5%. Uncertainties are dominated by the calibration errors except the measurements for $^{17}O/^{16}O$ with statistical uncertainties of 5% and $^{13}C^{17}O^{16}O/^{12}C^{16}O_2$ with statistical uncertainties of 9%. The isotopic ratios for ^{17}O and ^{18}O could only be isolated from the more dominant peaks on the same mass (^{16}OH on 17 u/e and $H_2^{16}O$ on 18 u/e), because the background pressure and therefore the water signal was very low. To obtain this ratios at the comet might be difficult since the water signal is very prominent. However to distinguish a low signal like expected for ^{18}O from a much higher signal like $H_2^{16}O$, a peak fit with respect to the slightly broader foot of the peak has to be used. Therefore a combination of a Gauss and Lorentz peak shape was used (Pseudo-Voigt). The uncertainties of the fit compared to the raw data is smaller than the statistical uncertainties of the peak itself.

The sensitivity measurements were performed for all detectors and all emissions. The total signal for CO_2 for the MCP/LEDA includes the signal of the *parent*, the fragments, all measured isotopic abundances for the *parent* and the fragments, and the amount of doubly charged *parents* (0.01%). The statistical error for the sensitivity measurement is $< 1\%$. The uncertainties of the pressure measurement are ∼14% (see App. F). Calibration uncertainties of the MCP/LEDA such as gain calibration and individual pixel gain corrections are estimated as ∼ 7%. Calibration uncertainties of the CEM and the FC detector are

Table 20: Sensitivities of DFMS FM for CO_2

Emission	MCP/LEDA	CEM	FC
	CO_2 Sensitivities for HR [cm^3]		
200 μA	1.538 x 10^{-19}	4.540 x 10^{-19}	4.727 x 10^{-19}
20 μA	5.835 x 10^{-19}	1.373 x 10^{-19}	2.895 x 10^{-18}
2 μA	6.601 x 10^{-19}	1.403 x 10^{-19}	2.865 x 10^{-18}
	CO_2 Sensitivities for LR [cm^3]		
200 μA	2.107 x 10^{-18}	5.610 x 10^{-18}	1.765 x 10^{-17}
20 μA	6.001 x 10^{-18}	9.223 x 10^{-19}	1.805 x 10^{-17}
2 μA	7.034 x 10^{-18}	1.005 x 10^{-18}	3.151 x 10^{-17}

assumed to be $\sim 5\%$. The total uncertainties for the sensitivity in HR are therefore: 16% for MCP/LEDA and 15% for CEM & FC. The evaluation of the proportion of the signal in LR is deduced from the HR spectra therefore an additional uncertainty ($\sim 5\%$) has to be taken into account, leading to slightly higher uncertainties. Uncertainties for the sensitivity in LR are therefore: 17% for MCP/LEDA and 16% for CEM & FC.

5.8 Alkanes

Alkanes are acyclic branched or un-branched hydrocarbons having the general formula C_nH_{2n+2}, and therefore consisting entirely of hydrogen atoms and saturated carbon atoms [Moss et al., 1995]. The detection of alkanes in comets are confirmed for CH_4 and C_2H_6, while for C_3H_8 the search has been negative so far [Bockelée-Morvan et al., 2004]. The following information is a summary of [Bockelée-Morvan et al., 2004]: CH_4 and C_2H_6 were first clearly spectroscopically detected in comet Hyakutake, through ground based observations in 1996. In every comet searched since then, Methane and Ethane was detected. The abundance of CH_4/H_2O varies from 0.14% to 1.4%. Among Oort cloud comets, the abundance for C_2H_6/H_2O is remarkably constant ($\sim$ 0.6%), with the exception of C/1999 S4 (LINEAR). In comet Halley an abundance of 0.4% was found with *in situ* measurements of NMS.

5.8.1 CH_4 Methane

Methane can be found in the background of Rosetta due to spacecraft outgassing, therefore a careful subtraction of the background is necessary for an absolute density in the comets coma relative to water.
Calibration measurements for CH_4 for all detectors and emissions were performed at one pressure level (1 x 10^{-7} mbar, background pressure 1 x 10^{-9} mbar). The pressure measurements are relative to N_2 since no correction factor is given for CH_4. A possible correction factor of 0.56 – 0.71 is found for a similar pressure sensor [Controller, 2001], however since this factor is not given for the used pressure sensor a correction was not applied.

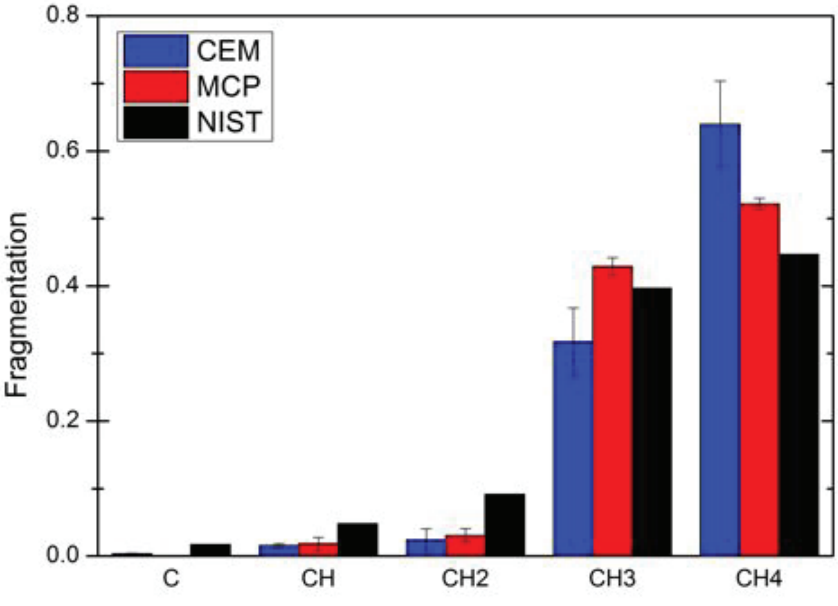

Figure 46: The fragmentation pattern for CH_4 for MCP/LEDA and CEM compared to NIST. Errorbars for MCP/LEDA and CEM are due to the average for all emissions.

The fragmentation pattern for CH_4 for MCP/LEDA and CEM relative to NIST can be found in Fig. 46. The fragmentation patterns shows more *parents* than fragments compared to NIST. This can be explained by the lower electron energy in the ion source compared to

NIST. The differences between MCP/LEDA and CEM can be explained by the detection efficiency of the MCP.

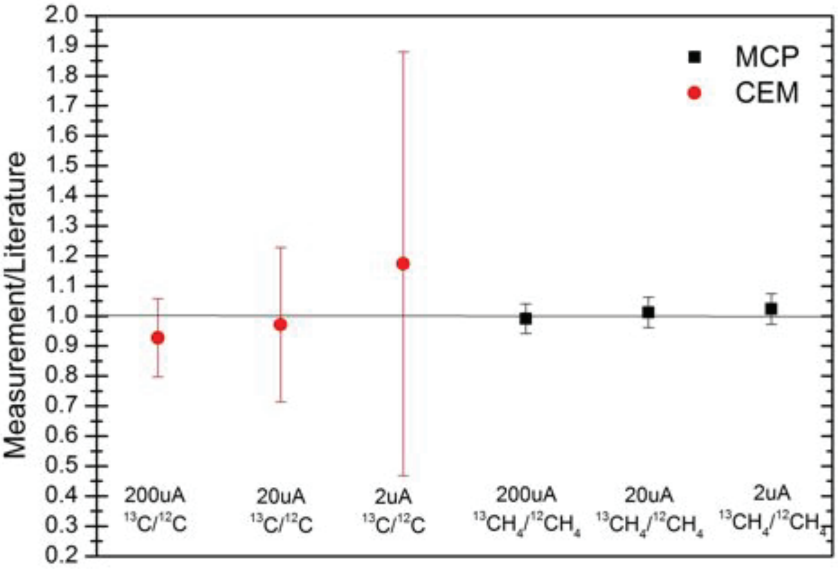

Figure 47: Isotopic abundances measured with DFMS relative to literature values for CH_4.

Isotopic abundances for $^{13}C/^{12}C$ for the CEM and $^{13}CH_4/^{12}CH_4$ for the MCP/LEDA for all emissions can be found in Fig. 47. All measurements are in agreement with the literature value, however for the CEM measurements the statistical uncertainties dominate the uncertainties due to calibration errors. Statistical uncertainties for the CEM measurements are: 200 μA 13%, 20 μA 26%, and 2 μA 60%. Statistical uncertainties for the MCP/LEDA measurements are: 200 μA 0.4%, 20 μA 0.7%, and 2 μA 1%. The total uncertainty contains also calibration uncertainties of 7% for the MCP/LEDA and 5% for the CEM. The statistical uncertainties for the CEM could be reduced by a longer integration time or the sum of several spectra.

Table 21: Sensitivities of DFMS FM for CH_4

Emission	MCP/LEDA	CEM	FC
	CH_4 Sensitivities for HR $[cm^3]$		
200 μA	5.661 x 10^{-19}	9.990 x 10^{-19}	9.440 x 10^{-19}
20 μA	6.059 x 10^{-19}	1.339 x 10^{-18}	1.700 x 10^{-18}
2 μA	3.247 x 10^{-19}	1.829 x 10^{-18}	N/A
	CH_4 Sensitivities for LR $[cm^3]$		
200 μA	1.153 x 10^{-17}	1.306 x 10^{-17}	9.480 x 10^{-18}
20 μA	1.920 x 10^{-17}	2.354 x 10^{-17}	2.650 x 10^{-17}
2 μA	2.389 x 10^{-17}	2.816 x 10^{-17}	1.430 x 10^{-17}

Sensitivity measurements for all detectors and emissions for LR and HR can be found in Tab. 21. The density for CH_4 is given relative to N_2, since the pressure measurements were not corrected. Therefore sensitivities for CH_4 are given relative to N_2. The total signal for CH_4 contains the signal of the *parent*, all fragments, and isotopic abundances for $^{13}C/^{12}C$ and $^{13}CH_4/^{12}CH_4$. No doubly charged *parent* could be detected since the mass range for DFMS does not cover 8 u/e. The sensitivity for the FC is in good agreement with the CEM sensitivities, however no signal could be detected for 2 μA for the FC in HR. The sensitivities for 200 μA are slightly lower then for the other emissions, with the exception of the MCP/LEDA in HR, where the sensitivity for 2 μA is lower than for 200 μA. A possible reason for this could be that the instrument had to be switched of several times during the measurements of the MCP/LEDA for 2 μA due to software problems. Therefore the background measurements for the MCP/LEDA were performed with a 'cold' instrument and might be underestimated. The factor between the sensitivity for LR and HR is due to the resolution sensitive slit, which explains a factor of $\sim$ 14, further differences are due to ion optical differences for LR and HR. The statistical error for the sensitivity measurement is $<$ 1%. The uncertainties of the pressure measurement are $\sim$14% (see App. F). Calibration uncertainties of the MCP/LEDA such as gain calibration and individual pixel gain corrections are estimated as $\sim$ 7%. Calibration uncertainties of the CEM and the FC detector are assumed to be $\sim$ 5%. The total uncertainties for the sensitivity in HR are therefore: 16% for MCP/LEDA and 15% for CEM & FC. The evaluation of the proportion of the signal in LR is deduced from the HR spectra therefore an additional uncertainty ($\sim$ 5%) has to be taken into account, leading to slightly higher uncertainties. Uncertainties for the sensitivity in LR are therefore: 17% for MCP/LEDA and 16% for CEM & FC.

5.8.2 C_2H_6 Ethane

Ethane can be found in the background of Rosetta due to spacecraft outgassing [Schläppi et al., 2010], therefore a careful subtraction of the background is necessary for an absolute density in the comets coma relative to water.
The calibration measurements for C_2H_6 were performed for all detectors and emissions at one pressure level. The pressure during measurements was 1 x 10^{-7} mbar and the background pressure before introducing gas into the chamber was 5 x 10^{-10} mbar. The pressure measurements are relative to N_2 since no pressure correction factor is given for C_2H_6. A possible correction factor of 0.357 – 0.400 is found for a similar pressure sensor [Controller, 2001], however since this factor is not given for the used pressure sensor a correction was not applied. The measurements were performed with measurement modes for the MCP/LEDA and CEM, and manually for 30 u/e for the FC.

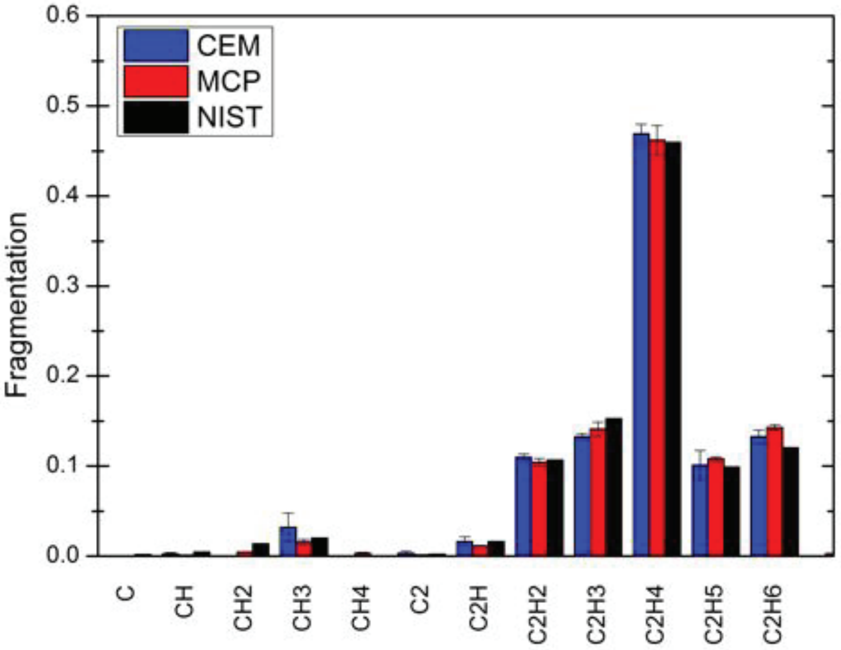

Figure 48: The fragmentation pattern of C_2H_6 measured with the MCP/LEDA and the CEM. For comparison NIST values are given. Error bars are due to standard deviation of the average for all emissions.

The fragmentation pattern of C_2H_6 for the MCP/LEDA and the CEM can be found in Fig. 48. The fragmentation pattern for both detectors are deduced from the measurements of all emissions. The average values for all emissions are given in Fig. 48. Uncertainties of the fragmentation pattern are due to standard deviation of the average of all emission for one detector. Statistical uncertainties are in the same range or lower than the standard deviation. The fragmentation behavior of the ion source DFMS FM is almost in agreement with the NIST values although the electron energy is lower. The ratio of the *parent* is slightly higher for DFMS FM than the ratio in NIST while for other fragments the values are comparable. Differences between the MCP/LEDA and the CEM can be explained by the different detection efficiencies of the detectors.
The isotopic measurements presented here are $^{13}C^{12}CH_6/^{12}C_2H_6$ measured with the MCP/LEDA

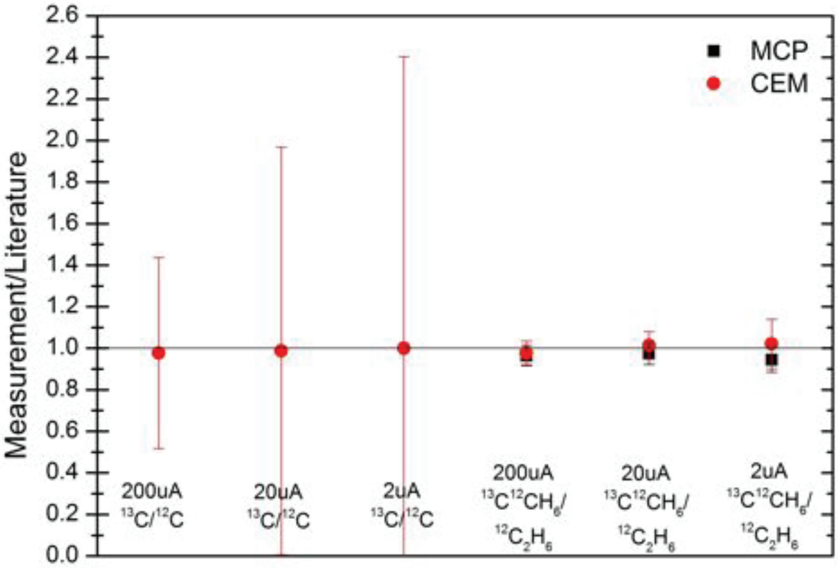

Figure 49: Isotopic measurements of C_2H_6 with the MCP/LEDA (black) and the CEM (red). The measurements are in good agreement with literature value, however the statistical uncertainties for the $^{13}C/\ ^{12}C$ measured with the CEM are rather high. Mass 12 can only be measured with the CEM, therefore no measurements for the MCP/LEDA are available for $^{13}C/\ ^{12}C$

and the CEM for all emission and $^{13}C/^{12}C$ measured with the CEM (see Fig. 49). The isotopic measurements are in good agreement with the literature value, however the statistical uncertainties for the CEM measurements are rather high since the amount of C due to fragmentation is very low ($< 1\%$). For an emission of 200 μA the statistical uncertainty is 46% and for the other emissions they are 140% for 2 μA and 100% for 20 μA. However the measurement itself is in remarkably good agreement with literature. Uncertainties of the isotopic measurements with the MCP/LEDA of $^{13}C^{12}CH_6/^{12}C_2H_6$ are dominated by the calibration uncertainty of 7% for all emissions. The statistical uncertainties are $< 1\%$ for all emissions. The isotopic measurement with the CEM are also in good agreement with literature. The statistical uncertainties for the isotopic measurements of the CEM are 3%, 4%, and 10% for 200 μA, 20 μA, and 2 μA.

Table 22: Sensitivities of DFMS FM for C_2H_6

Emission	MCP/LEDA	CEM	FC
	C_2H_6 Sensitivities for HR $[cm^3]$		
200 μA	8.712 x 10^{-20}	1.627 x 10^{-19}	1.192 x 10^{-19}
20 μA	3.108 x 10^{-19}	6.281 x 10^{-19}	6.298 x 10^{-19}
2 μA	4.596 x 10^{-19}	1.064 x 10^{-18}	N/A
	C_2H_6 Sensitivities for LR $[cm^3]$		
200 μA	2.715 x 10^{-18}	4.983 x 10^{-18}	5.434 x 10^{-18}
20 μA	4.898 x 10^{-18}	8.598 x 10^{-18}	9.097 x 10^{-18}
2 μA	8.980 x 10^{-18}	9.730 x 10^{-18}	8.949 x 10^{-18}

The sensitivity measurement for all detectors and emissions can be found in Tab. 22. No signal was detected for 2 μA with the FC, therefore the sensitivity is marked with N/A. The total signal for sensitivity calculations of C_2H_6 contains the signal of the *parent*, the fragments and the signal of the isotopes $^{13}C^{12}CH_6$ for all detectors and ^{13}C for the CEM. The sensitivities are relative to N_2 since the pressure was not corrected for C_2H_6. The sensitivities for 200 μA are clearly lower than for the other emissions. An explanation therefore could be that the space charge because of the higher density of electrons for 200 μA emission around the filament, harms the entrance of the electrons into the ionization region. The electrons have to pass a slit before entering the ionization region, and less electrons are entering the ion source through that slit because they diverge due to space charge. The factor between sensitivities of the MCP/LEDA and the CEM in HR are rather high compared to LR. The statistical error for the sensitivity measurement is $< 1\%$. The uncertainties of the pressure measurement are $\sim$14% (see App. F). Calibration uncertainties of the MCP/LEDA such as gain calibration and individual pixel gain corrections are estimated as $\sim 7\%$. Calibration uncertainties of the CEM and the FC detector are assumed to be $\sim 5\%$. The total uncertainties for the sensitivity in HR are therefore: 16% for MCP/LEDA and 15% for CEM & FC. The evaluation of the proportion of the signal in LR is deduced from the HR spectra therefore an additional uncertainty ($\sim 5\%$) has to be taken into account, leading to slightly higher uncertainties. Uncertainties for the sensitivity in LR are therefore: 17% for MCP/LEDA and 16% for CEM & FC.

5.8.3 C_3H_8 Propane

A small amount of Propane can be found in the background of Rosetta due to spacecraft outgassing [Schläppi et al., 2010], therefore a careful subtraction of the background is necessary for an absolute density in the comets coma relative to water. Furthermore the knowledge about the fragmentation pattern might help to identify fragments of the *parent* molecule.

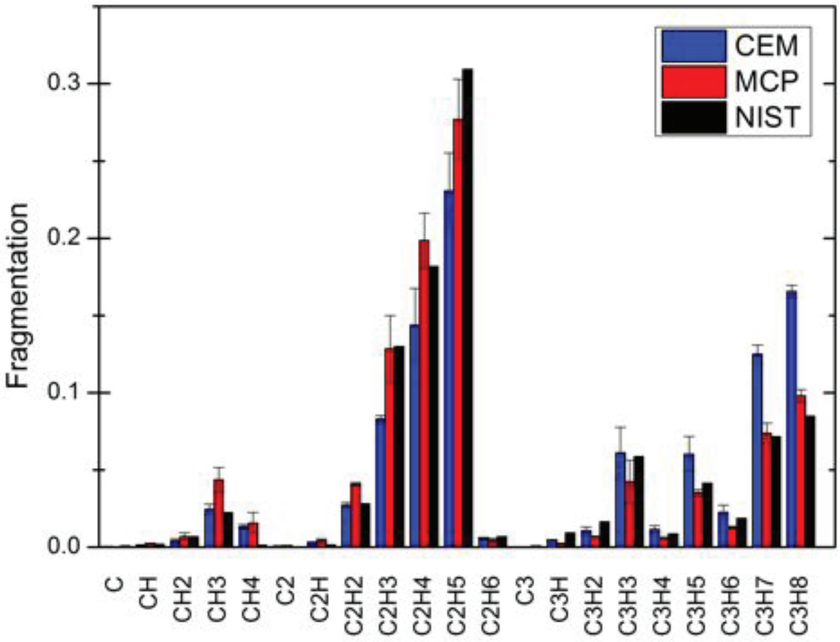

Figure 50: Fragmentation pattern for C_3H_8 measured with MCP/LEDA and CEM, with the average for all emissions compared to NIST. Error bars are due to standard deviation of the average.

Calibration measurements for C_3H_8 for all detectors and emissions were performed at one pressure level (1 x 10^{-7} mbar, background pressure 1 x 10^{-9} mbar). The pressure measurements are relative to N_2 since no correction factor is given for C_3H_8. A possible correction factor of 0.24 – 0.28 is found for a similar pressure sensor [Controller, 2001], however since this factor is not given for the used pressure sensor a correction was not applied.
The fragmentation pattern for MCP/LEDA and CEM compared to NIST can be found in Fig. 50. Error bars of the MCP/LEDA and CEM are the standard deviation of the average of all emission. In principle the amount of fragments relative to the *parent* molecule is smaller compared to NIST. However the fragment CH_4 is definitely higher than in NIST. First a contamination from the measurement before was suggested, but later measurement show the same ratio for CH_4 relative to the *parent* molecule. An other contamination source could be from Air, while leaking in between bottle and valve. This could also be ruled out because the signal for Ar, N_2, O_2, CO_2 and H_2O are within statistical uncertainties in the same order as background measurements. In summary the fragmentation pattern values for the lighter fragments (m$\leq CH_4$), should be used with care.
Measurements of the isotopic abundances are possible for the fragments that are saturated (CH_4 and C_2H_6) and the *parent* molecule itself as well as the $^{13}C/^{12}C$ ratio. Since other peaks of the isotopes overlap with the signal of the heavier fragment and are not necessarily

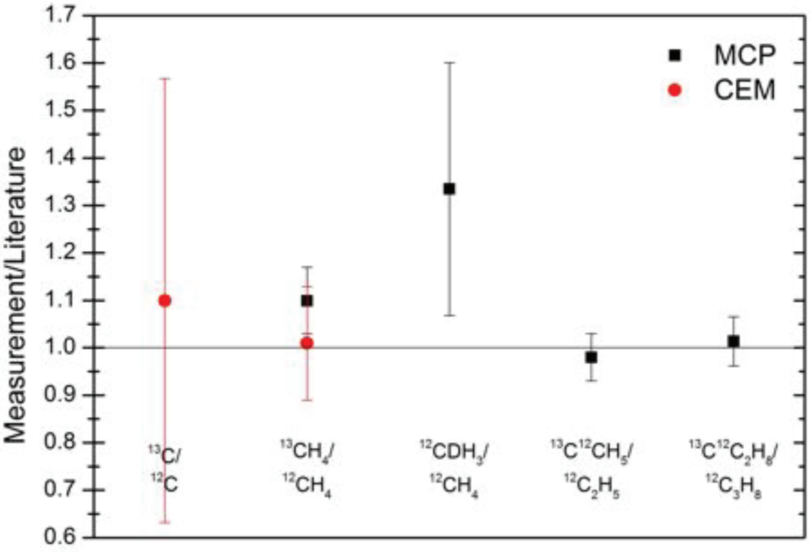

Figure 51: Isotopic abundances for C_3H_8 relative to literature value.

resolvable. The measured isotopic abundances for the MCP/LEDA for an emission of 200 μA and the CEM can be found in Fig. 51. The isotopic abundance for ^{13}C of the *parent* molecule $^{12}C_3H_8$ and the fragment $^{12}C_2H_6$ measured with the MCP/LEDA are in good agreement with the literature value within uncertainties. Uncertainties are due to statistics ($< 1\%$) and calibration (5%). Further isotopic ratios for D/H and ^{13}C for the MCP/LEDA are not in agreement with literature values. They are both higher than the literature value. A depletion for the isotopic abundances could be explained by the fragmentation pattern, since the fragmentation pattern shows a significant high signal compared to NIST for CH_4. However the two peaks for $^{13}CH_4$ and $^{12}CDH_3$ are clearly separated and do not overlap with $^{15}NH_2$ or $^{14}NH_3$. A signal due to doubly charged particles on this mass (17 u/e) is also not possible since no signal could be detected for 34 u/e. The isotopic abundances for ^{13}C measured with the CEM are in good agreement with literature value, however statistical uncertainties are rather high: 10% for $^{13}CH_4/^{12}CH_4$, and 40% for $^{13}C/^{12}C$. Since the integration time of the CEM is nominal 1 s per step while the integration time for the MCP/LEDA is 19.8 s, the statistical uncertainties are higher for the CEM than the MCP/LEDA. An other reason for the rather high statistical uncertainties is that only 1% of the total signal for propane is found as fragment on ^{12}C.

Sensitivity measurements for all detectors and emissions for LR and HR can be found in Tab. 23. The density C_3H_8 is relative to N_2, since the pressure was not corrected, therefore sensitivities are relative to N_2. The total signal for C_3H_8 contains the signal of all fragments, isotopic abundances as discussed for Fig. 51. No doubly charged *parent* molecule could be detected for C_3H_8 on mass 22 u/e. This is expected since hydrocarbons do more likely fragment, than get doubly charged. And because the electron energy energy is reduced, the amount of doubly charged particles is reduced as well. The sensitivity for the FC is in agreement with the CEM sensitivities for 200 μA in LR but slightly higher for HR. No signal could be detected for FC with 20 μA in HR and 2 μA for C_3H_8. The sensitivity for 200 μA is lower than for the other emissions. The factor between the sensitivity for LR and HR is due to the resolution sensitive slit, which explains a factor of ~ 14, further differences

Table 23: Sensitivities of DFMS FM for C_3H_8

Emission	MCP/LEDA	CEM	FC
	C_3H_8 Sensitivities for HR [cm^3]		
200 μA	8.196 x 10^{-20}	3.248 x 10^{-19}	5.089 x 10^{-19}
20 μA	3.249 x 10^{-19}	7.501 x 10^{-19}	N/A
2 μA	2.872 x 10^{-19}	9.611 x 10^{-19}	N/A
	C_3H_8 Sensitivities for LR [cm^3]		
200 μA	1.409 x 10^{-18}	5.501 x 10^{-18}	5.795 x 10^{-18}
20 μA	3.793 x 10^{-18}	9.145 x 10^{-18}	1.050 x 10^{-17}
2 μA	4.107 x 10^{-18}	1.102 x 10^{-17}	N/A

are due to ion optical differences for LR and HR.

The statistical error for the sensitivity measurement is $< 1\%$. The uncertainties of the pressure measurement are $\sim$14% (see App. F). Calibration uncertainties of the MCP/LEDA such as gain calibration and individual pixel gain corrections are estimated as $\sim$ 7%. Calibration uncertainties of the CEM and the FC detector are assumed to be $\sim$ 5%. The total uncertainties for the sensitivity in HR are therefore: 16% for MCP/LEDA and 15% for CEM & FC. The evaluation of the proportion of the signal in LR is deduced from the HR spectra therefore an additional uncertainty ($\sim$ 5%) has to be taken into account, leading to slightly higher uncertainties. Uncertainties for the sensitivity in LR are therefore: 17% for MCP/LEDA and 16% for CEM & FC.

5.8.4 C_4H_{10} Butane

Butane can be found in the background measurements of the spacecraft, due to outgassing (see Schläppi et al. (2010)).

The calibration measurements of Butane were performed with n-Butane and contain measurements of all detectors and emissions. The pressure during measurements was 1 x 10^{-7} mbar and the background pressure before introducing gas into the chamber was 5 x 10^{-10} mbar. The pressure measurements are relative to N_2 since no pressure correction factor is given for C_4H_{10}. A possible correction factor of 0.204 – 0.213 is found for a similar pressure sensor [Controller, 2001], however since this factor is not given for the used pressure sensor a correction was not applied. The measurements were performed with measurement modes for the MCP/LEDA and CEM, and manually for 58 u/e for the FC.

The fragmentation pattern for C_4H_{10} measured with MCP/LEDA and CEM can be found in Fig. 52. The values given are the average of the ratios for all emissions of one detector. The standard deviation is taken as uncertainties for the ratios. Uncertainties due to statistics are smaller than standard deviation. The fragmentation pattern of DFMS contains more heavier fragments compared to NIST, especially in the measurements with CEM the amount of C_4H_{10} is higher. Differences between the MCP/LEDA and the CEM are given by the detection efficiency of the MCP/LEDA. One can clearly see that the detection efficiency for the MCP/LEDA for the heavier masses is lower than for the CEM.

The isotopic measurements are limited to the heaviest fragments of the Alkanes (C_nH_{2n+2}, n = 1 ... 4) since the isotopes of the other fragments do overlap with heavier fragments at the resolution of the instrument. The measurements presented are in HR for an emission of 200 μA for the CEM and the MCP/LEDA (see Fig. 53). All measurements are in good agreement with literature values. The isotopic ratio of $^{13}C/^{12}C$ measured with the CEM has rather high uncertainties due to statistics (80%). $^{13}CH_4/^{12}CH_4$ could be measured with the CEM and the MCP/LEDA, statistical uncertainties for the MCP/LEDA are 3%, and 13% for the CEM. The total uncertainty contains also calibrations uncertainties of the MCP/LEDA (7%) and the CEM (5%). To resolve $^{13}CH_4$ from $^{12}CDH_3$ a Gauss fit was applied since the two partly overlap at the resolution of the instrument with the MCP/LEDA. The uncertainties of the fit are smaller than the statistical error, therefore no additional error was taken into account. The statistical uncertainties of $^{12}CDH_3/^{12}CH_4$ are 12%. For the other ratios the statistical uncertainties are $< 1\%$ and the total uncertainties are dominated by the calibration error.

The sensitivity measurements for C_4H_{10} for all detectors and emissions can be found in Tab. 24. The sensitivities are relative to N_2 since the pressure was not corrected for C_4H_{10}. The sensitivity of the CEM is much higher compared with them of the MCP/LEDA. The main reason therefore is that the detection efficiency of the MCP/LEDA is decreasing with mass. No signal could be detected for C_4H_{10} with an emission of 2 μA for the FC and in HR for an emission of 20 μA. Since the measurements with the FC were only done on C_4H_{10}, a signal could have been detected for a more abundant fragment. However the sensitivity of the FC is in agreement with the CEM sensitivity and therefore the CEM sensitivity could be used as reference for the FC.

The statistical error for the sensitivity measurement is $< 1\%$. The uncertainties of the pressure measurement are $\sim$14% (see App. F). Calibration uncertainties of the MCP/LEDA such as gain calibration and individual pixel gain corrections are estimated as $\sim$ 7%. Calibration uncertainties of the CEM and the FC detector are assumed to be $\sim$ 5%. The total uncertainties for the sensitivity in HR are therefore: 16% for MCP/LEDA and 15% for

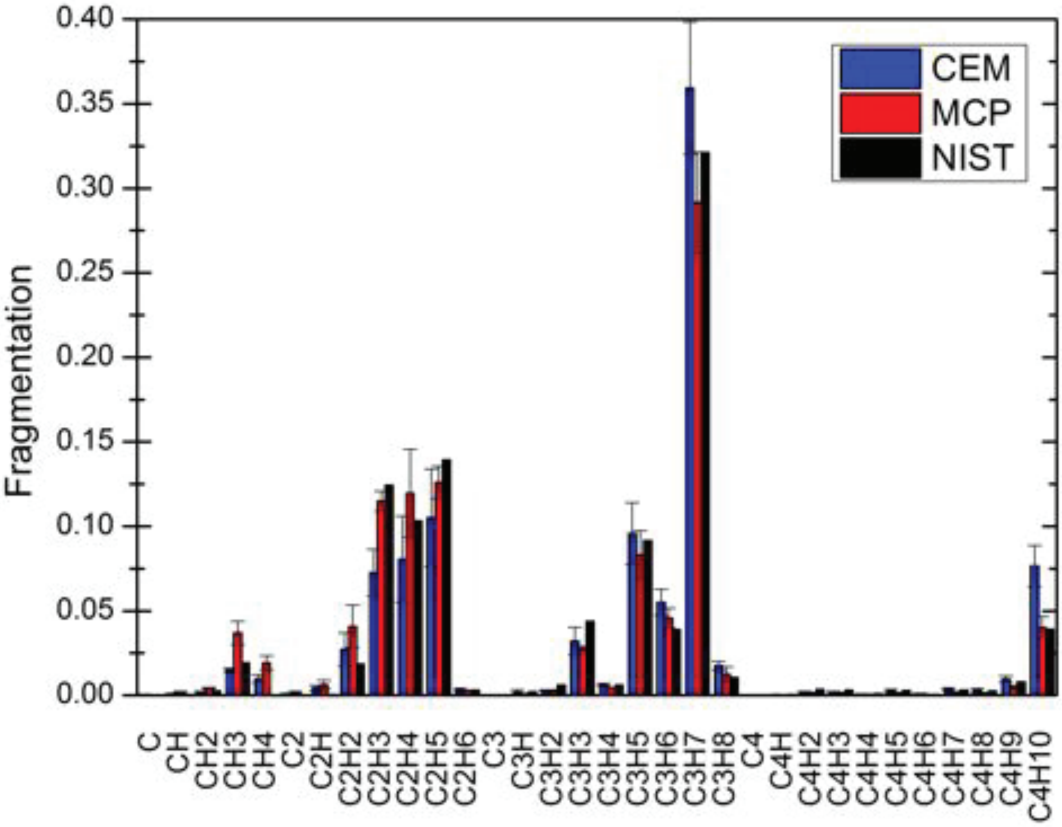

Figure 52: The fragmentation pattern for C_4H_{10} measured with MCP/LEDA and CEM. For comparison the values of NIST are given. Error bar are due to the standard deviation of the average for all emission.

CEM & FC. The evaluation of the proportion of the signal in LR is deduced from the HR spectra therefore an additional uncertainty ($\sim$ 5%) has to be taken into account, leading to slightly higher uncertainties. Uncertainties for the sensitivity in LR are therefore: 17% for MCP/LEDA and 16% for CEM & FC.

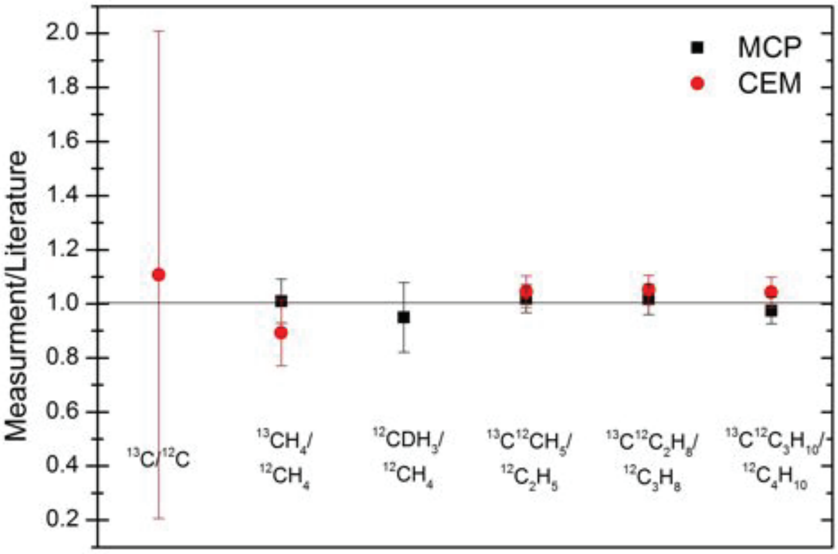

Figure 53: Isotopic abundances of C_4H_{10} relative to literature. The measurements are performed with an emission of 200 μA for the MCP/LEDA (black) and the CEM (red). The measurements are in good agreement with literature value.

5.9 Alkene

Alkenes are acyclic branched or unbranched hydrocarbons having one carbon-carbon doubly bond and the general formula C_nH_{2n} [Moss et al., 1995]. The detection of Alkenes in comets was negative so far [Bockelée-Morvan et al., 2004]. However a bunch of hydrocarbons are present in the gas cloud surrounding Rosetta due to spacecraft outgassing [Schläppi et al., 2010], therefore a careful calibration is necessary. Alkenes measurements presented in this work are only available for Ethylene, other compounds will be part of the still ongoing calibration campaign for DFMS.

5.9.1 C_2H_4 Ethylene

The calibration measurements for C_2H_4 were performed for all detectors and all emission at one pressure level. The pressure during measurements was 1 x 10^{-7} mbar and the background pressure before gas inlet was 1 x 10^{-9} mbar. The pressure measurements are not corrected because no correction factor was available for the pressure gauge. The pressure measurements are therefore relative to N_2. A possible correction factor of 0.400 – 0.455 is found for a similar pressure sensor [Controller, 2001], however since this factor is not given for the used pressure sensor a correction was not applied. The measurements were performed with measurement modes for the MCP/LEDA and CEM, and manually for 28 u/e for the FC.

The fragmentation pattern measured with DFMS FM recorded with the MCP/LEDA and CEM can be found in Fig. 54. For comparison the fragmentation found in NIST is given, note that the electron energy for the NIST values is 70 eV, while the electron energy for DFMS is 45 eV and the fragmentation pattern of DFMS is not expected to be the same as the one given in NIST. The fragmentation presented here is the average of all measurements for different emissions. As uncertainties the standard deviation of the average is given.

Table 24: Sensitivities of DFMS FM for C_4H_{10}

Emission	MCP/LEDA	CEM	FC
	C_4H_{10} Sensitivities for HR $[cm^3]$		
200 μA	1.515 x 10^{-19}	3.205 x 10^{-19}	4.611 x 10^{-19}
20 μA	1.946 x 10^{-19}	5.877 x 10^{-19}	N/A
2 μA	2.047 x 10^{-19}	7.542 x 10^{-19}	N/A
	C_4H_{10} Sensitivities for LR $[cm^3]$		
200 μA	2.212 x 10^{-18}	6.193 x 10^{-18}	6.860 x 10^{-18}
20 μA	2.037 x 10^{-18}	7.454 x 10^{-18}	7.127 x 10^{-18}
2 μA	1.340 x 10^{-18}	7.518 x 10^{-18}	N/A

Statistical uncertainties are in the same range as the standard deviation, therefore the standard deviation was used. The fragmentation pattern of DFMS contains more *parents*, while the fragment C_2H_3 is depleted compared to NIST, the other fragments are in the same range or higher than NIST. Differences between MCP/LEDA and CEM can be explained by differences in the detection efficiencies of the detectors.

The evaluation of isotopic abundances was only done for C_2H_4 since the signal of the isotopes of a fragment due overlap with the heavier fragment and can only be separated if the heavier fragment is less abundant than the isotope. The isotopic abundances measured with DFMS for C_2H_4 and C are all in good agreement with literature (see Fig. 55). $^{13}C/^{12}C$ was measured with the CEM with 200 μA, statistical uncertainties are 20% and dominate the total uncertainties. The measurements for $^{13}C^{12}CH_4/^{12}C_2H_4$ with the MCP/LEDA are given for all emissions. The total uncertainties are dominated by the calibration uncertainties of 5% for the MCP/LEDA and statistical uncertainties are $< 1\%$. $^{13}C_2H_4/^{12}C_2H_4$ measured with the MCP/LEDA for all emissions are in agreement with literature. Statistical uncertainties are: 200 μA 6%, 20 μA 9%, and 2 μA 18%.

The sensitivity was calculated for all detectors and all emissions for DFMS FM (see Tab. 25). The sensitivities are lower for 200 μA and the CEM is more sensitive than the MCP/LEDA. This can be explained by the detection efficiency of the MCP/LEDA, that is lower than for the CEM for C_2H_4. The total ion current of C_2H_4 for the sensitivity contains the signal of C_2H_4, the fragments and the isotopes of the *parent*. Since the pressure measurements are not corrected, the sensitivities for C_2H_4 are relative to N_2.

Table 25: Sensitivities of DFMS FM for C_2H_4

Emission	MCP/LEDA	CEM	FC
	C_2H_4 Sensitivities for HR $[cm^3]$		
200 μA	6.912 x 10^{-20}	1.380 x 10^{-19}	1.493 x 10^{-19}
20 μA	4.490 x 10^{-19}	8.905 x 10^{-19}	7.310 x 10^{-19}
2 μA	6.466 x 10^{-19}	1.300 x 10^{-18}	N/A
	C_2H_4 Sensitivities for LR $[cm^3]$		
200 μA	7.460 x 10^{-19}	1.596 x 10^{-18}	2.065 x 10^{-18}
20 μA	8.354 x 10^{-18}	1.281 x 10^{-17}	1.370 x 10^{-17}
2 μA	8.260 x 10^{-18}	1.523 x 10^{-17}	1.809 x 10^{-17}

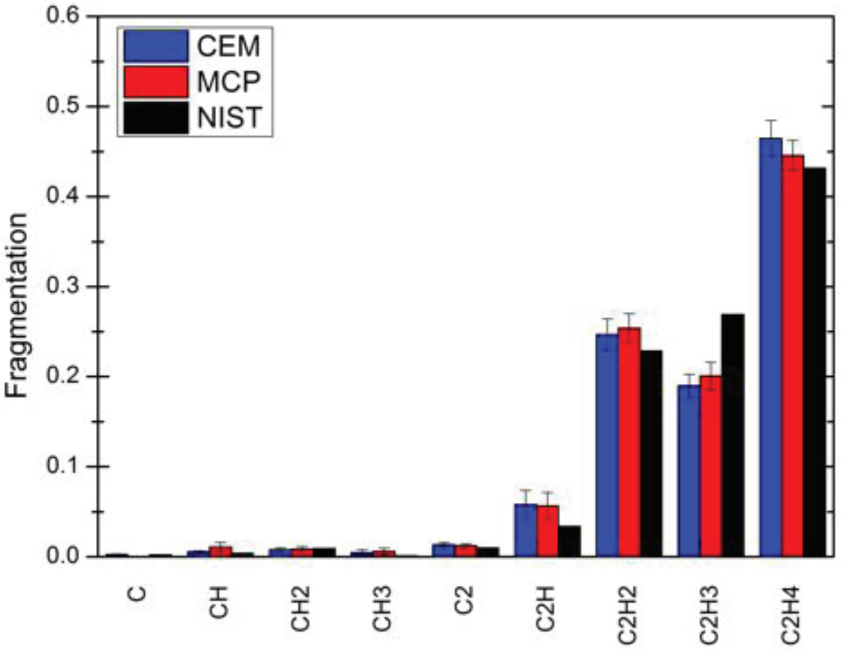

Figure 54: The fragmentation pattern for C_2H_4 measured with MCP/LEDA and CEM. For comparison the values found in NIST are given. Error bar are due to the standard deviation of the average for all emission.

The statistical error for the sensitivity measurement is $< 1\%$. The uncertainties of the pressure measurement are ~14% (see App. F). Calibration uncertainties of the MCP/LEDA such as gain calibration and individual pixel gain corrections are estimated as $\sim 7\%$. Calibration uncertainties of the CEM and the FC detector are assumed to be $\sim 5\%$. The total uncertainties for the sensitivity in HR are therefore: 16% for MCP/LEDA and 15% for CEM & FC. The evaluation of the proportion of the signal in LR is deduced from the HR spectra therefore an additional uncertainty ($\sim 5\%$) has to be taken into account, leading to slightly higher uncertainties. Uncertainties for the sensitivity in LR are therefore: 17% for MCP/LEDA and 16% for CEM & FC.

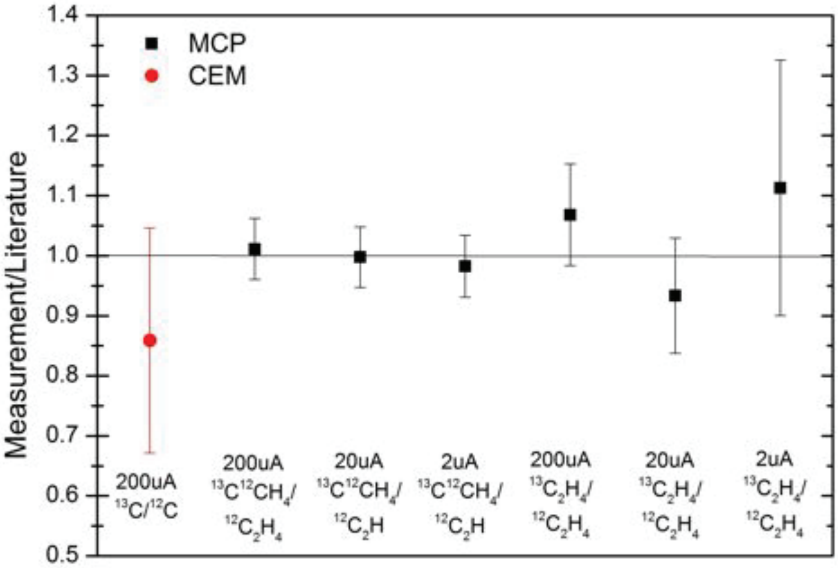

Figure 55: The isotopic abundances for C_2H_4 and C measured with the MCP/LEDA (black) and the CEM (red). All measurements are in good agreement with literature. Error bars are discussed in the text. For C no measurements are available for the MCP/LEDA, because of the limited mass range.

5.10 Minimal densities detectable with DFMS FM and adapted for FS

The detectable density limit of DFMS is important to show DFMS capabilities to detect gas of cometary origin when the comet is not yet very active. Immediately after hibernation of the spacecraft (and far away from the comet) the signal will be dominated by spacecraft outgassing [Schläppi et al., 2010] but will play a minor role when the comet gets more active. The density is calculated by solving Eq. 15 for the density:

$$\rho_i = \frac{I_i}{S_{total,i} \cdot I_{emi}} \tag{40}$$

where ρ_i is the number density for neutral species i $[cm^{-3}]$, I_i is the detected current of the corresponding ion on the MCP/LEDA or CEM $[A]$, $S_{total,i}$ is the sensitivity of species i $[cm^3]$, and I_{emi} is the emission current of the filament $[A]$. To keep the rough estimation as simple as possible the dissociative electron impact ionization from higher mass molecules on the same m/q signal was neglected.

To deduce the minimal density detectable with DFMS, the following settings are chosen to maximize the signal of this density at the detectors: LR and an emission of 200 μA, because more ions can pass the resolution sensitive slit in LR than in HR and more ions get ionized at the maximum emission. The sensitivities for the FM are lower for an emission of 200 μA than for the lower emissions as shown during calibration. However, the sensitivity for the FS is higher for 200 μA than for the other emissions [Eberhardt, 2008a, Altwegg, 2008a, Eberhardt, 2008b, Altwegg, 2008b], and the minimal density detectable with DFMS might therefore be higher for the FM than for the FS.

To deduce the minimal signal detected by the detectors the following assumptions are made:

- MCP/LEDA: one ion impinges on the MCP for an integration time of 20 s and the resulting signal is detected by the LEDA (according to Eq. 18 this is a signal of ∼ 150 counts on GS 16).

- CEM: five ions during an integration time of 1 s (according to Eq. 34 this is a signal of 1 count in LR).

To get an overview of the detection limits of the calibrated species, they are listed in Tab. 26:

Table 26: Minimal densities detectable by DFMS FM

Species	Density MCP/LEDA [cm^{-3}]	Density CEM [cm^{-3}]
Ne	33 ± 5	3419 ± 547
Ar	10 ± 2	493 ± 79
Kr	62 ± 10	633 ± 101
Xe	117 ± 19	399 ± 64
H_2O	8 ± 1	1237 ± 198
N_2	8 ± 1	716 ± 115
CO_2	19 ± 3	725 ± 116
CH_4	3 ± 1	313 ± 50
C_2H_6	15 ± 2	817 ± 131
C_3H_8	29 ± 5	740 ± 118
C_4H_{10}	18 ± 3	657 ± 105
C_2H_4	54 ± 9	2559 ± 409

The detection limits for the MCP/LEDA are much lower than for the CEM. However, the nominal integration time of the MCP/LEDA is 20 s and therefore a factor of 20 higher than for the CEM. The detection limit can be further reduced by addition of several spectra and therefore a higher total integration time. The minimal densities of these species detected by the FS will be higher because of the higher sensitivity for 200 μA and can be used as upper limits of the minimal density required to be detectable by DFMS FS. Also the detection limit for water is harmed by the spacecraft surrounding background cloud due to outgassing (see Schläppi et al. (2010)).
The required sensitivity given in Balsiger et al. (2007) of 10^{-5} $A/mbar$ correlates with a signal of 1 ion detected in 500 s for a density of 1 cm^{-3} and an emission of 10 μA and meets the here presented signal of one ion in 20 s for an emission of 200 μA. The sensitivity for this condition calculated according to Eq. 15 is ∼ 1 x 10^{-17} cm^3. This sensitivity could be roughly reproduced with the FM for the following species in LR: Ar, H_2O, N_2, CH_4, and C_2H_6.

6 Analysis of gas mixture

In this chapter different gas mixtures are analyzed to show the quality of the calibration measurements. This chapter presents the most difficult part of the data analysis; where signal is first identified, transformed into ion current, and ultimately resulting in deduction of partial and total densities. DFMS FS can measure relative densities at the comet and COPS FS measurements will be used to translate into accurate total densities. The intent is to show DFMS capabilities immediately after hibernation as the first measurements will utilize the settings used for the measurements in this section (MCP/LEDA, HR, and 200 μA). Three gas mixtures were analyzed:

- GCU gas a mixture of Ne, Xe and CO_2
- Noble gas mixture containing Ne, Ar, Kr, and Xe
- Gas mixture containing CO_2 and C_3H_8

The measurement procedure was the same as for the calibration campaign (see Sec. 5.2).

6.1 Data treatment

The lab environment has the advantage that the measured species are known and therefore the data analysis is biased by this knowledge. It is clearly known if a species is a fragment or the *parent* itself. The situation for the FS and therefore the analysis of the data is different. The measured mixture at the comet will be dominated by the background due to spacecraft outgassing as the comet will not yet be very active (directly after hibernation of the spacecraft). Although the background is mainly dominated by water, a lot of different species were detected before hibernation [Schläppi et al., 2010]. These species will likely still be detectable after hibernation, but should be of the same order of magnitude or less. Once the comet becomes active and the spacecraft is close, the detected signal should then be dominated by outgassing of the comet. Once a signal is identified as the signal of species i, the total density can be calculated by the following (i can be a fragment, the *parent* or an isotope):

$$\rho_{total,i} = \frac{I_i}{S_{total,i}} \frac{1}{f_i} \frac{1}{I_{emi}} \tag{41}$$

Where $\rho_{total,i}$ is the total density for i $[cm^{-3}]$ including the density of all the fragments and isotopes. I_i is the measured ion current for i $[A]$, $S_{total,i}$ is the total sensitivity for i $[cm^3]$, f_i is the factor of the fragmentation pattern or the isotopic abundance (if known) and I_{emi} is the emission current $[A]$. I_i is calculated as described for the MCP/LEDA in Eq. 18 and for the CEM in Eq. 34. The MCP/LEDA data was treated as described in Sec. 4.3.
The partial density of i can be calculated the following:

$$\rho_i = \frac{I_i}{S_{total,i}} \frac{1}{I_{emi}} \tag{42}$$

The partial density of i does not need to be corrected for a fragmentation pattern, since the ion currents can be directly interpreted as the partial density of i.

6.2 Possible approach

Identification of parent molecules and the composition analysis requires a complex approach. The data analysis process involves an informed correlation of the signal in the spectra of each individual mass to identify *parents*, fragments and isotopes. The best way to find the *parents* is to start at the heaviest masses. Species that are known to be measured such as H_2O, CO_2, and the GCU-component gases, help to determine the mass scales of each spectrum and therefore the range of p_0. Since the mass range of DFMS is limited, comparisons with RTOF for heavier species will help to identify heavy molecules and the possible fragments thereof. Once a *parent* is identified, the fragmentation pattern of this molecule can be subtracted and with the remaining signal one can proceed. To check if the identification of a signal is adequate, the spectra of the isotopes and the fragments must also be taken into account. If the fragments or isotopes are not available or their abundances do not adequately match the data, the signal might be incorrectly identified. Because the isotopic abundances in the coma of the comet are not necessarily expected to be in agreement with Earth abundances they must be handled carefully.

To get an overview of the total mass range, the ion currents for every spectrum can be placed together according to their mass.

6.3 GCU gas: Ne+CO_2+Xe

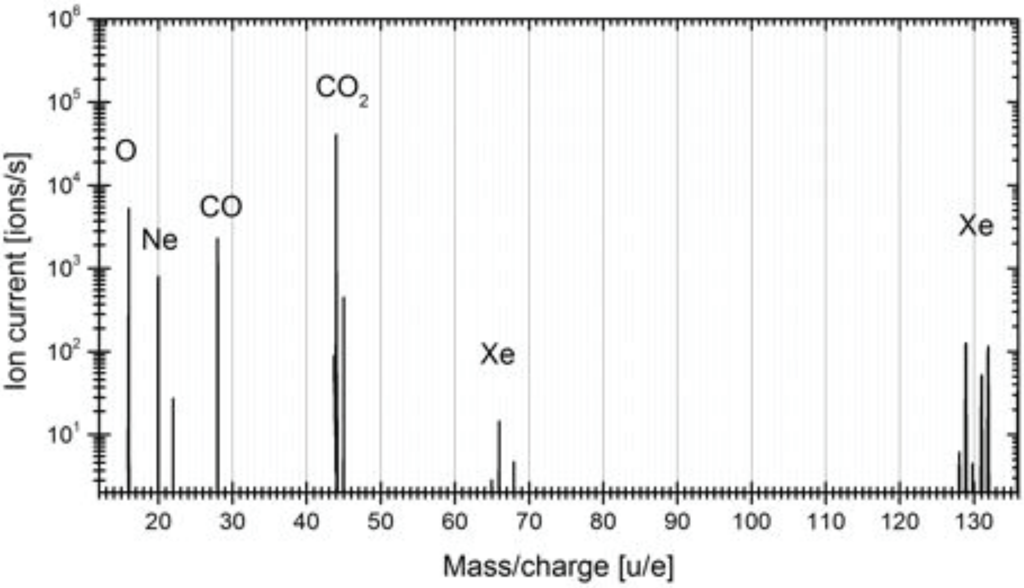

Figure 56: MCP/LEDA measurement in HR with an emission of 200 μA for the GCU gas. The GCU contains Ne, CO_2 and Xe. The peaks around 66 u/e are the signal of the doubly charged Xe. The signal of O and CO are the fragments of CO_2.

The gas in the GCU of DFMS contains mainly CO_2, Ne and Xe. The mixture was chosen to contain 90% CO_2, 9% Ne and 0.9% Xe and 0.1% He of the volume. The description of the bottle containing the same GCU gas as used to fill the GCU can be found in Tab. 27.

Table 27: Description of the GCU gas mixture.

Species	Ratio of Volume [%]	Relative ratio of Volume [%]	Relative ratio of weight [%]	Bottle description [%]	rel. deviation [%]
CO_2	100	90.1	92.886	91.938 (rest)	2
Ne	10	9.0	4.260	4.490	2
Xe	1	0.9	2.845	2.574	2
He	0	0.1	0.009	0.998	2

The GCU gas is directly introduced into the ion source of DFMS. The pressure outside of the ion source was 1.0 x 10^{-7} mbar (no correction applied). This pressure is expected to be lower than the actual pressure inside the ion source, since the gas is introduced directly into the ion source. The calibration measurements for CO_2, Ne, and Xe can now be used to calibrate the pressure inside the ion source for GCU measurements. For the GCU measurements there exist special measurement modes. In these modes the masses 44, 45, 28, 22, 20, 16, 64, 65, 66 (only in HR), 68, 129, 132 (only in HR), 136, and 44 again are commanded. Therefore the isotopic measurements are limited. To reduce measurement time for the MCP/LEDA the total integration time of this modes is 66 ms and 150 accumulations, resulting in a total integration time of 9.9 s. The measurements presented are recorded with the MCP/LEDA at HR and an emission setting of 200 μA.

Table 28: Fragmentation of the GCU gas for CO_2 measured with the MCP/LEDA in HR for an emission of 200 μA.

Species	Fragmentation measured	Total uncertainties [%]	Fragmentation calibrated	Standard deviation
^{16}O	0.110	5	0.121	0.014
$^{12}C^{16}O$	0.105	5	0.099	0.006
$^{12}C^{16}O_2$	0.784	5	0.779	0.016

The fragmentation pattern for CO_2 in the GCU gas is given in Tab. 28. For comparison the calibrated fragmentation pattern for CO_2 is given with the standard deviation as uncertainties. The fragmentation behavior for CO_2 in the GCU gas is in good agreement with the calibrated fragmentation. Total uncertainties for CO_2 in the GCU gas is given by the calibration error of the MCP/LEDA and the statistical uncertainties (<1%).

Table 29: Isotopic abundances of the GCU gas measured with the MCP/LEDA in HR with an emission of 200 μA. The gas mixture contains: Ne, CO_2 and Xe. Total uncertainties are discussed in the text.

Species	Measured isotopic abundance [%]	Total uncertainties [%]	Literature* [%]
^{20}Ne	100	5	100
^{22}Ne	10.2	6	10.2
^{132}Xe	100	5	100
^{136}Xe	31.2	6	33.0
^{129}Xe	99.9	5	98.8
$^{12}C^{16}O_2$	100	5	100
$^{13}C^{16}O_2$	1.09	6	1.08

*[Handbook of Chemistry and Physics, 2012]

The measured isotopic abundances for the GCU gas can be found in Tab. 29. All isotopic measurements are in good agreement with literature. Since the covered mass range is limited, some isotopic ratios were not evaluated. The statistical uncertainties for all ratios is $< 1\%$. The total uncertainties include a calibration error of 5%.

The total density for Ne was calculated using Eq. 41 for the total density ($f_{^{20}Ne} = 0.905$) and Eq. 18 for the ion current of ^{20}Ne. The total density for Xe was calculated in the same way for ^{132}Xe ($f_{^{132}Xe} = 0.269$). The total density of CO_2 was calculated for CO_2 ($f_{CO_2} = 0.779$). The total density for the GCU gas is the total of the three and is (1.87 ± 0.52) x 10^{10} cm^3 containing 10.4% ± 1.7% Ne, 3.0% ± 0.2% Xe and 86.6% ± 13.9% CO_2. The uncertainties are due to the calibration of the sensitivities (Ne: 16%, Xe: 16%, and CO_2: 16%). The composition is in agreement with the given composition of the GCU-gas. The total density is not in agreement with the pressure measured outside of the ion source. The GCU-gas is introduced directly into the ion source and a higher pressure inside the ion source is expected. The pressure inside the ion source according to the measured density is (7.05 ± 1.95) x 10^{-7} mbar.

6.4 Noble gas mixture: Ne–Ar–Kr–Xe

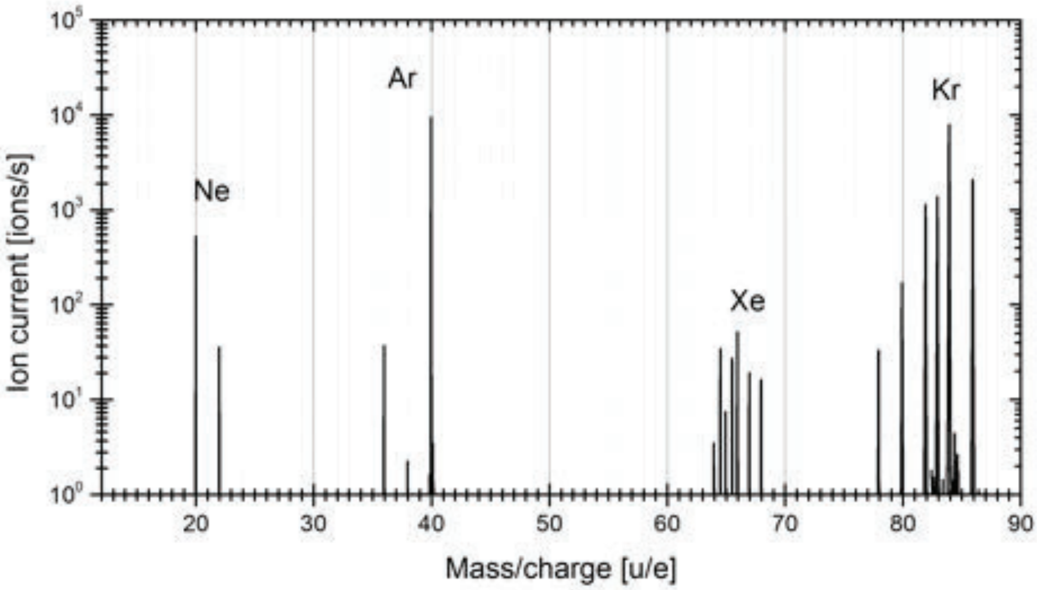

Figure 57: Measurement of a gas mixture containing Ne, Ar, Kr, and Xe measured with the MCP/LEDA in HR at an emission of 200 μA. The peaks marked as Xe are due to the doubly charged Xenon.

The measurements of the gas mixture with Ne, Ar, Kr, and Xe are performed at a measured pressure of 1 x 10^{-7} mbar (no correction applied). The background pressure was 5 x 10^{-9} mbar. The gas mixture is a bottle containing 25% of the molecules of each gas. A spectrum of the total mass range for this mixture is given in Fig. 57. The measurements are recoded with nominal scan modes, therefore the mass range of the HR mode does not cover the mass of Xe but the doubly charged Xenon. Since all the detected ions were originally neutrals and measurements were performed in the neutral mode, the charge state of the atoms is not indicated. The background measurements are already subtracted, therefore neither H_2O nor CO_2 are visible.

The measured isotopic abundances for the mixture can be found in Tab. 30. All the measurements are in good agreement with literature value. The total uncertainties contain the calibration uncertainties of the MCP/LEDA (5%) and the statistical uncertainties. With the exception of ^{126}Xe and ^{124}Xe the total uncertainties are dominated by the calibration uncertainties.

Table 30: Isotopic abundances of the gas mixture measured with the MCP/LEDA in HR with an emission of 200 μA. The gas mixture contains: Ne, Ar, Kr, and Xe. Total uncertainties are discussed in the text.

Species	Measured isotopic abundance [%]	Total uncertainties [%]	Literature* [%]
^{20}Ne	100	5	100
^{21}Ne	0.30	7	0.30
^{22}Ne	10.7	5	10.2
^{40}Ar	100	5	100
^{38}Ar	0.06	6	0.06
^{36}Ar	0.36	5	0.34
^{84}Kr	100	5	100
^{86}Kr	30.2	5	30.3
^{83}Kr	20.3	5	20.2
^{82}Kr	20.2	5	20.3
^{80}Kr	4.00	5	4.01
^{78}Kr	0.62	5	0.62
^{132}Xe	100	5	100
^{136}Xe	32.5	6	33.0
^{134}Xe	38.4	6	38.8
^{131}Xe	79.7	5	78.8
^{130}Xe	14.8	6	15.2
^{129}Xe	97.6	5	98.8
^{128}Xe	7.09	7	7.14
^{126}Xe	0.33	16	0.35
^{124}Xe	0.32	16	0.35

*[Handbook of Chemistry and Physics, 2012]

The total density for Ne was calculated by the sum of the partial density using Eq. 42 for every isotope and the sensitivity of the MCP/LEDA for 200 μA in Tab. 13. The ion current for every isotope was calculated according to Eq. 18. The total densities for Ar and Kr are calculated in the same way with the corresponding sensitivities (Ar: Tab. 14 and Kr: Tab. 15). The sensitivity for Xe in Tab. 16 was corrected for the doubly charged Xe with a factor of 0.013 (1.3%). The total density is then calculated in the same way as for the other noble gases. The total measured density for the mixture is 3.45 x 10^9 cm^{-3} and contains; 13% ± 2% Ne, 24% ± 4% Ar, 26%± 4% Kr, and 37% ± 5% Xe. The measured pressure of 1.08 x 10^{-7} mbar is corrected with the average of all the correction factors (for correction factors see App. F), since the ratio of every gas should be the same. The total density measured with DFMS is in good agreement with the total density deduced from the pressure measurements of 3.56 x 10^9 cm^{-3}. The uncertainties are dominated by the uncertainties of the sensitivities of 16%, however the difference between the total densities is only 3.1%. The composition of the mixture is not in agreement with the expected 25% for every compound. A possible reason for the difference could be found in the setup for static measurements. Since the pumps are always running while the amount of pumped gas is compensated by the inlet of the gas, this is not a completely static environment. The pumping efficiency for the different compounds has an influence on the relative composition of the measured gas. Ne is much easier to pump than Xe. This was observed during the calibration campaign, since the contamination of the background measurements after the calibration of Xe was much higher then for Ne. Ne disappears almost immediately after the gas inlet is closed, it must therefore be much easier to pump. This might not be the only explanation but seems appropriate. An other explanation could be that the calibration of the sensitivities is not in the expected quality. But this can be negotiated since the same effect is also detected in the measurements with LR and for other emissions.

6.5 CO_2+C_3H_8

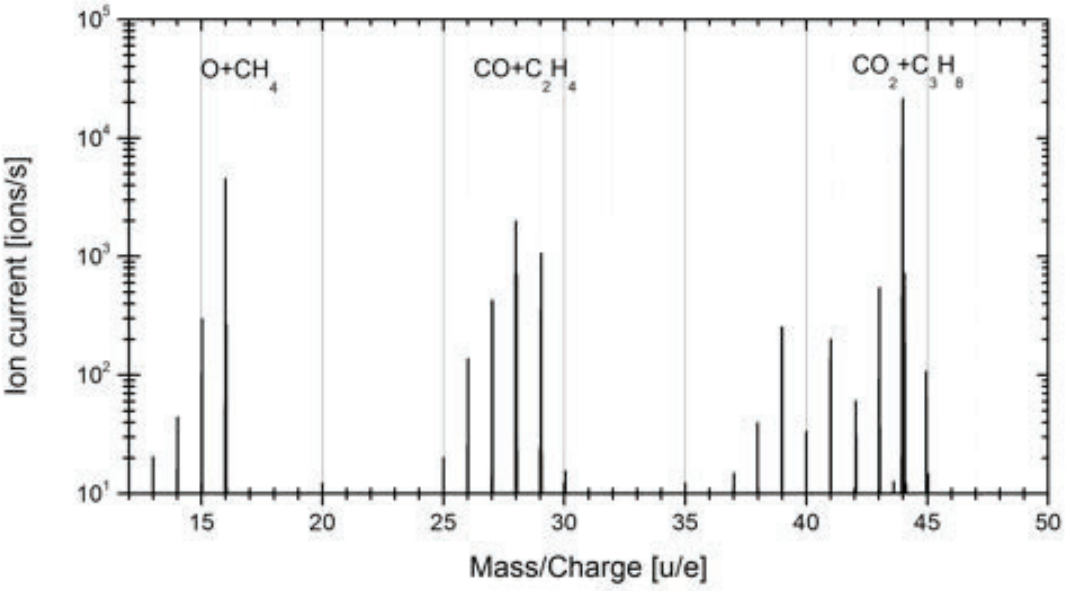

Figure 58: MCP/LEDA measurement in HR with an emission of 200 μA for the $CO_2 + C_3H_8$ mixture. HR spectra with a better resolution of the three highlighted peaks can be found in Fig. 59. For a better overview the other fragments of C_3H_8 are not highlighted but can be found in Tab. 32.

The measurements of the gas mixture containing $CO_2 + C_3H_8$ are performed at a measured pressure of 8.9 x 10^{-7} mbar (no correction applied). The background pressure was 6.8 x 10^{-10} mbar. The gas mixture was produced through the flow controller of CASYMIR in the GMU (see Sec. 5.1). To control the gas inlet one gas after the other was introduced into the GMU and the GMU was still pumped. When the pump was switched off, the GMU was filled with ~50% CO_2 and ~50% C_3H_8. The gas was then introduced from the GMU into the chamber at the leak valve (LV4) used for the static calibration. The measurements for the MCP/LEDA with an emission of 200 μA are recorded with scan modes covering the mass range of 13 u/e – 50 u/e. The complete mass scan in HR of the mixture recorded with the MCP/LEDA at an emission of 200 μA can be found in Fig. 58. The peaks were signals of both gases can be found are highlighted and the composition is indicated. To show the capability of DFMS to resolve these peaks, spectra of 16 u/e, 28 u/e, and 44 u/e in a logarithmic scale are given in Fig. 59. Background measurements are carefully subtracted, therefore no signal of N_2 is found on the spectrum of 28 u/e.

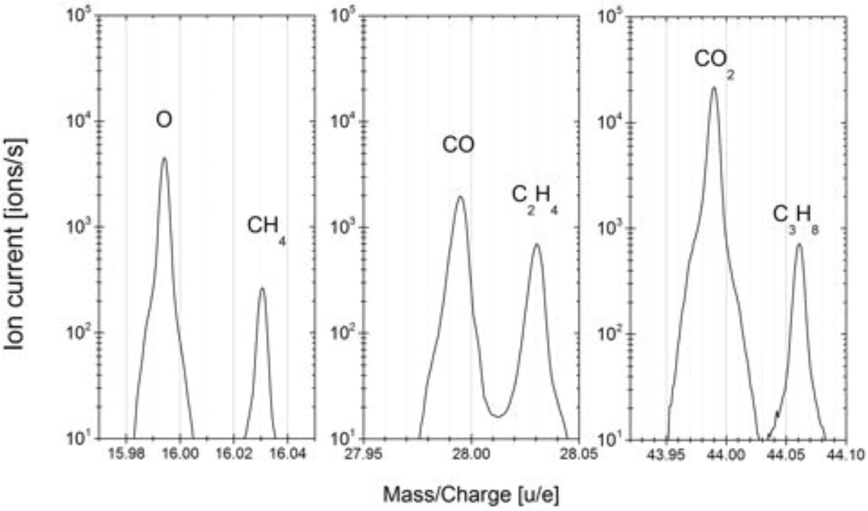

Figure 59: The three spectra of the fragments and the parent molecule of both gases. MCP/LEDA measurement in HR with an emission of 200 μA for the CO_2 + C_3H_8 mixture.

Table 31: Fragmentation of the gas mixture for CO_2 measured with the MCP/LEDA in HR for an emission of 200 μA.

Species	Fragmentation measured	Total uncertainties [%]	Fragmentation calibrated	Standard deviation
^{16}O	0.119	5	0.121	0.014
$^{12}C^{16}O$	0.091	5	0.099	0.006
$^{12}C^{16}O_2$	0.775	5	0.779	0.016

The fragmentation pattern for the gas mixture of CO_2 + C_3H_8 can be found in Tab. 31 for CO_2 and Tab. 32 for C_3H_8. For comparison the calibrated fragmentation pattern of the calibration campaign is given and the standard deviation as uncertainties. The total uncertainties of the fragmentation pattern of the gas mixture contain the statistical uncertainties and the calibration uncertainties for the MCP/LEDA. The fragmentation behavior of CO_2 is in good agreement with the calibrated fragmentation. The fragmentation ratio of $^{12}C_3H$, $^{12}C_3H_5$, and $^{12}C_3H_6$ for C_3H_8 are not in agreement with the calibration. An explanation could be that the most present fragment $^{12}C_2H_5$ has total uncertainties of 5% and can therefore deviate 0.014, this has an influence on the other fragments ratios. To show the impact of the statistical uncertainties, the total uncertainties does not take into account this variation. In summary the fragmentation behavior of CO_2 and C_3H_8 during the calibration could be reproduced in this gas mixture.

Table 32: Fragmentation of the gas mixture for C_3H_8 measured with the MCP/LEDA in HR for an emission of 200 μA.

Species	Fragmentation measured	Total uncertainties [%]	Fragmentation calibrated	Standard deviation
^{12}CH	0.002	5	0.002	0.000
$^{12}CH_2$	0.008	5	0.007	0.002
$^{12}CH_3$	0.041	5	0.044	0.008
$^{12}CH_4$	0.018	5	0.016	0.007
$^{12}C_2$	0.001	6	0.001	0.000
$^{12}C_2H$	0.004	5	0.004	0.001
$^{12}C_2H_2$	0.042	5	0.041	0.001
$^{12}C_2H_3$	0.128	5	0.128	0.022
$^{12}C_2H_4$	0.194	5	0.198	0.018
$^{12}C_2H_5$	0.285	5	0.277	0.026
$^{12}C_3$	0.000	17	0.000	0.000
$^{12}C_3H$	0.003	5	0.002	0.000
$^{12}C_3H_2$	0.007	5	0.007	0.001
$^{12}C_3H_3$	0.040	5	0.042	0.014
$^{12}C_3H_4$	0.007	5	0.006	0.001
$^{12}C_3H_5$	0.032	5	0.035	0.002
$^{12}C_3H_6$	0.010	5	0.013	0.001
$^{12}C_3H_7$	0.072	5	0.074	0.007
$^{12}C_3H_8$	0.100	5	0.098	0.004

The isotopic ratios for the gas mixture containing CO_2 and C_3H_8 can be found in Tab. 33. All isotopic ratios are in agreement with literature. The total uncertainties take into account the calibration uncertainties of the MCP/LEDA (5%) and statistical uncertainties. The statistical uncertainties of the isotopes are: 4% for $^{13}C^{16}O$, 3% for $^{13}C^{16}O_2$, 3% for $^{13}C^{12}CH_5$, and 4% for $^{13}C^{12}C_2H_8$.

Table 33: Isotopic abundances of the gas mixture with the MCP/LEDA in HR at an emission of 200 μA. The gas mixture contains: CO_2 and C_3H_8. Total uncertainties are discussed in the text.

Species	Measured isotopic abundance [%]	Total uncertainties [%]	Literature* [%]
$^{12}C^{16}O$	100	5	100
$^{13}C^{16}O$	1.05	7	1.08
$^{12}C^{16}O_2$	100	5	100
$^{13}C^{16}O_2$	1.05	6	1.08
$^{12}C_2H_5$	100	5	100
$^{13}C^{12}CH_5$	2.03	6	2.16
$^{12}C_3H_8$	100	5	100
$^{13}C^{12}C_2H_8$	3.11	7	3.24

*[Handbook of Chemistry and Physics, 2012]

The total density for CO_2 was calculated for CO_2 using Eq. 41 and the sensitivity of Tab. 20. For f_{CO_2} the calibrated fragmentation ratio for CO_2 in Tab. 31 was used. The total density for CO_2 is (1.04 ± 0.17) x 10^9 cm^{-3}. The total uncertainties are dominated by the calibration uncertainties of the sensitivity of 16%. The total density for C_3H_8 was calculated for C_3H_8 in the same way and is (1.18 ± 0.19) x 10^9 cm^{-3}. The total density for the gas mixture is then (2.22 ± 0.36) x 10^9 cm^{-3} containing 47% ± 8% CO_2 and 53% ± 8% C_3H_8. The pressure measurements are (7.0 ± 1.2) x 10^{-8} mbar. The pressure measurements are corrected with the average of the corrections factors for CO_2 and N_2, since the ratio for both gases is the same and C_3H_8 sensitivities are given relative to N_2 (for explanation see Sec. 5.8.3). The uncertainties of the pressure measurements are 14%. The resulting density is then (2.0 ± 0.28) x 10^9 cm^{-3}. The total density of the gas mixture is in good agreement with the density of the pressure measurements.

7 Conclusion and outlook

The goal of this work was to further improve the knowledge about the peculiarities of DFMS, the instrument handling with GSEOS, to improve the knowledge about the data analysis and the handling of technical problems is achievable. This part is intended as a brief conclusion and outlook of this work, concerning DFMS, the characteristics, the calibration, and the evaluation of measured gas mixtures.

DFMS characteristics:

The characterization of the instrument contains: ionization and fragmentation behavior in the ion source, instrument transmission and detection efficiency. Furthermore a detailed description of the data analysis to transform the signal into an ion current is given.

The sensitivity of an instrument depends on the ionization efficiency in the ion source, the instrument transmission and the detection efficiency. The ionization in the ion source for different electron energies confirmed the most efficient ionization for an electron energy of 45 eV as expected from the work in Schläppi (2011). The fragmentation behavior of the ion source of DFMS depends strongly on the electron energy and can therefore be manipulated to suppress (22 eV) or force (70 eV) fragmentation. The transmission of the instrument depends on the resolution of the instrument because of the ion path through the instrument and goes roughly with 1/m. The sensitivity then is the combination of the ionization efficiency, the fragmentation behavior, the instrument transmission and the detection efficiency. An absolute calibration of each of these characteristics is not feasible since the sensor is operated as a total an therefore the sensitivity is the combination of these characteristics. However, e.g. the ratio of the detection efficiencies of the MCP/LEDA relative to the CEM can be deduced and is necessary to deduce sensitives of species where a calibration was not realizable.

The characteristics for the FM can be adapted to the FS with the exception of the ionization efficiency of the different emission currents of the filament. The ionization efficiency of the FM for an emission current of 200 μA is less than a factor of 10 compared to 20 μA, but for the FS the factor is > 10. However, since the FS is on the spacecraft the influence of this effect can be used in a beneficial way, although the physical effect is not understood by the author.

Calibration of DFMS in a static environment:

The calibration was performed for several species (see Tab. 34) and the results for isotopic ratios mostly confirm literature values[Handbook of Chemistry and Physics, 2012]. The sensitivity of DFMS FM for this species, was calibrated and the fragmentation behavior measured.

The linear behavior of the signal measured by DFMS and the density of the gas could be reproduced for Ne and Ar and is therefore expected for the other species as well. The quality of the calibration of the fragmentation pattern is difficult to set in context with other measurements and instruments as found in NIST, since the electron energy in the ion source is reduced (DFMS: 45 eV and NIST: 70 eV). However, the tendency that the fragmentation is lower for lower energies and higher for higher electron energies has been shown. The calibration campaign presented in this work as well as further calibration measurements

Table 34: The gases used for calibration of DFMS and references for tables.

Species	Tab. of Sensitivities	Tab. of fragmentation pattern MCP	Tab. of fragmentation pattern CEM
Ne	13	MCP/LEDA: None	CEM: None
Ar	14	MCP/LEDA: None	CEM: None
Kr	15	MCP/LEDA: None	CEM: None
Xe	16	MCP/LEDA: None	CEM: None
H_2O	18	MCP/LEDA: E.4	CEM: E.3
N_2	19	MCP/LEDA: E.6	CEM: E.5
CO_2	20	MCP/LEDA: E.8	CEM: E.7
CH_4	21	MCP/LEDA: E.10	CEM: E.9
C_2H_6	22	MCP/LEDA: E.12	CEM: E.11
C_3H_8	23	MCP/LEDA: E.14	CEM: E.13
C_4H_{10}	24	MCP/LEDA: E.16	CEM: E.15
C_2H_4	25	MCP/LEDA: E.18	CEM: E.17

will provide fragmentation pattern for DFMS although a confirmation of the fragmentation pattern in NIST could have reduced the calibration measurements.

To compare the sensitivities of the calibration with earlier calibrations, the sensitivities in this work are transferred into a slope. The slope for Ne (20 μA) measured with the MCP/LEDA given in Riesen (2007) is 1.14 x 10^{12} for LR and 1.14 x 10^{11} for HR. The slope calculated as defined in Riesen (2007) for the Ne calibration in this work and for an emission of 20 μA is 4.77 x 10^{12} for LR and 2.13 x 10^{11} for HR. The slope represents the sensitivity over different pressure ranges. A higher slope means that the signal detected relative to the pressure was higher and therefore the sensitivity of the instrument. The sensitivity of DFMS FM for Ne has improved since the work of Riesen (2007). A possible explanation could be that the gain of the MCP was recalibrated or that the pixel gain corrections were consequently applied in this work, while Riesen (2007) tried to avoid this correction by shifting the maximal signal on the same pixel. The more likely reason however might be that between this work and Riesen (2007), the instrument was optimized by Schläppi (2011). The optimization was necessary to describe the sensor and its setting as total and in a physical manner and not only to find optimized settings to record one spectra for a small mass range.

The required sensitivity given in Balsiger et al. (2007) of 10^{-5} $A/mbar$ correlates with a signal of 1 ion detected in 500 s for a density of 1 cm^{-3} and an emission of 10 μA. The sensitivity for this conditions calculated according to Eq. 15 is $\sim$ 1 x 10^{-17} cm^3. DFMS FM does meet that requirement for the MCP/LEDA for the following species of the calibration in LR: Ar, H_2O, N_2, CH_4, and C_2H_6. It is known for the FS that the sensitivity for an emission of 200 μA is higher than for the other emissions. With the assumption that the FS is as sensitive as the FM for 20 μA and 2 μA, the list of species that meet the requirement given in Balsiger (2007) might even be enlarged.

The calibration campaign should be continued with other gases (e.g. CO, O_2) and other solid or liquid compounds that are expected to be found in comets or the spacecraft surrounding cloud. A detailed list of postulated and detected species in the coma of comets can be found in Bockelée-Morvan et al. (2004). To introduce the gaseous phase of these compounds the gas inlet of CASYMIR should be further improved so that compounds can be heated in a controlled way and the gaseous phase introduced into the chamber.

Analysis of gas mixtures:

The three gas mixtures that were analyzed are the following: GCU-gas with Ne+Xe+CO_2, noble gas mixture with Ne+Ar+Kr+Xe, and CO_2+C_3H_8. They were evaluated according to the calibration values found during the calibration campaign and are a test for the quality of the calibration. Although the set of mixtures was rather small and the evaluation was focused on the measurements of the MCP/LEDA, the expected densities and ratios of the mixture are in good agreement with the measurements of DFMS FM. However, mixtures of gases, where the fragment of one gas is detected on the same peak as the parent molecule of the other gas (CO and CO_2) might then show the real quality of the calibration of the fragmentation pattern and the sensitivities. Other interesting mixtures to measure are the combination of H_2O and CO_2. Therefore the calibration facility (CASYMIR) should be further improved to produce mixtures of different phases like H_2O and CO_2 in a controlled way and introduce them into the chamber. The calibration of the GCU-gas density inside the ion source is important to compare measurements of the FS with the FM.

The software to control the settings of the voltages and modes of DFMS is in a very stable condition so that the instrument can be operated over nights and weekends without minor errors. However, the stability of the software will only be confirmed if all three sensors (DFMS, RTOF and COPS) can measure at the same time, while commanded from the same DPU and over a long time range without any failures. Therefore additional software tests of all three sensors are planned.

Appendix

A SPICE Solar Aspect Angle (SAA)

```
****************************************************************************

SPICE code in c to extract the Solar Aspect Angle (SAA) of Rosetta
for the Lutetia flyby

****************************************************************************


---------------------------------kernel input-------------------------------
RO_kernels.tm contains the kernel input in the following order:

ck:   ATNR_P040302093352_00116.BC
fk:   EARTH_TOPO_050714.TF
fk:   EARTHFIXEDITRF93.TF
fk:   NEW_NORCIA_TOPO.TF
fk:   ROS_V16.TF
fk:   RSSD0002.TF
ik:   ROS_ROSINA_V11.TI
lsk:  NAIF0009.TLS
pck:  DE403-MASSES.TPC
pck:  EARTH_000101_110304_101211.BPC
pck:  PCK00008.TPC
sclk: ROS_101110_STEP.TSC
spk:  ORHR_______________00109.BSP
spk:  DE405.BSP
spk:  ROS_STRUCT_V2.BSP

The following kernels should be updated if the time range does not match the
time range of the kernels:

ck:  ATNR_P040302093352_00116.BC
pck: EARTH_000101_110304_101211.BPC
spk: ORHR_______________00109.bsp

Time ranges for these kernels:
ATNR_P040302093352_00116.BC
Object:  -226000
Interval Begin ET        Interval End ET          AV
------------------------ ------------------------ ---
2004-MAR-02 09:33:52.767 2011-MAR-31 01:01:06.183 Y

EARTH_000101_110304_101211.BPC
```

```
Frame: ITRF93 (3000)
 Start of Interval (ET)             End of Interval (ET)
 -----------------------------      -----------------------------
 2000 JAN 01 00:01:04.183           2011 MAR 05 00:01:06.185

ORHR______________00109.bsp
Body: ROSETTA (-226)
Start of Interval (ET)             End of Interval (ET)
-----------------------------      -----------------------------
2004 MAR 02 09:26:21.583           2014 MAY 23 01:43:30.120
-----------------------------------------------------------------------------

-------------------------------C-code----------------------------------------

#include <stdio.h>
#include <string.h>
#include "SpiceUsr.h"

#define METAKR "RO_kernels.tm"

#define SCLKID -226  // Cassini NAIF ID (aus naif_ids.html) -226 for ROSETTA
#define STRLEN 50  // Lenght of utctim +1!


int main (void)
      {

      SpiceChar               utctim [STRLEN];
      SpiceChar               utctim_start [STRLEN];
      SpiceChar               utctim_end [STRLEN];
      SpiceChar               start [STRLEN];
      SpiceChar               filename [STRLEN];

      SpiceDouble angle_radx;
      SpiceDouble angle_rady;
      SpiceDouble angle_radz;
      SpiceDouble angle_degx;
      SpiceDouble angle_degy;
      SpiceDouble angle_degz;
      SpiceDouble state [6];
      SpiceDouble rosx [3];
      SpiceDouble rosy [3];
      SpiceDouble rosz [3];
```

```
      SpiceDouble  et_start;
      SpiceDouble  et_end;
      SpiceDouble  et;
      SpiceDouble ltime;
      SpiceDouble delta;

      SpiceDouble pos [3];
      SpiceDouble dist_km;
      SpiceDouble dist_au;

      SpiceDouble step;
      SpiceDouble imax;

FILE  *solar_angle;

      furnsh_c ( METAKR );

// get UTC time to extract SAA
      prompt_c( "Input UTC Start-Time (2010-02-18T12:00:00): ",
STRLEN, utctim_start );
      prompt_c( "Input UTC End-Time (2010-02-18T22:00:00): ",
STRLEN, utctim_end );

      printf( "Converting UTC Start-Time: %s\n", utctim_start );
      printf( "Converting UTC End-Time: %s\n", utctim_end );

      strncpy (start, utctim_start, 10);
      sprintf( filename , "solarangle-%s.dat" , start );

      solar_angle = fopen ( filename ,"w"); // w :write

// Print used kernels in *.xls file
      fprintf(solar_angle,
      "The loaded Kernels are:\n %s\n %s\n %s\n %s\n %s\n %s\n
%s\n %s\n %s\n %s\n %s\n %s\n %s\n %s\n %s\n\n",
       "kernels/ck/ATNR_P040302093352_00116.BC",
"kernels/fk/EARTH_TOPO_050714.TF",
"kernels/fk/EARTHFIXEDITRF93.TF",
"kernels/fk/NEW_NORCIA_TOPO.TF",
"kernels/fk/ROS_V16.TF",
"kernels/fk/RSSD0002.TF",
"kernels/ik/ROS_ROSINA_V11.TI",
"kernels/lsk/NAIF0009.TLS",
```

```
"kernels/pck/DE403-MASSES.TPC",
"kernels/pck/EARTH_000101_110304_101211.BPC",
"kernels/pck/PCK00008.TPC",
"kernels/sclk/ROS_101110_STEP.TSC",
"kernels/spk/ORHR______________00109.BSP",
"kernels/spk/DE405.BSP",
"kernels/spk/ROS_STRUCT_V2.BSP");

      fprintf(solar_angle,"%s\t %s\t %s\t %s\t %s\n",
"UTC [YYYY-MM-DDTHH:MM:SS]","Solar angle x [deg]",
"Solar angle y [deg]", "Solar angle z [deg]","Solar Distanz [AU]");

// Convert start and end time into ET
      utc2et_c( utctim_start, &et_start );
      utc2et_c( utctim_end, &et_end );

// Time step to extract SAA in s (300 s = 5 min)
      step = 300;
      imax = (et_end - et_start)/step;

// Extract position vector (x,y,z) of the Sun in the Rosetta frame from kernels
      int i;
      for ( i=0; i< imax ;i++){
      et = (et_start + step*i);

      if( et < et_end )
      {
      spkezr_c( "SUN", et, "ROS_SPACECRAFT", "NONE", "ROSETTA", state, &ltime);

      rosx[0] = 1;
      rosx[1] = 0;
      rosx[2] = 0;

      rosy[0] = 0;
      rosy[1] = 1;
      rosy[2] = 0;

      rosz[0] = 0;
      rosz[1] = 0;
      rosz[2] = 1;


// Convert angle from rad to degrees for every vector
```

```
    angle_radx = vsep_c ( state, rosx );
    convrt_c ( angle_radx, "RADIANS", "DEGREES", &angle_degx);

    angle_rady = vsep_c ( state, rosy );
    convrt_c ( angle_rady, "RADIANS", "DEGREES", &angle_degy);

    angle_radz = vsep_c ( state, rosz );
    convrt_c ( angle_radz, "RADIANS", "DEGREES", &angle_degz);

// Extract heliocentric distance of Rosetta relative to the Sun
    pos [0] = state [0];
    pos [1] = state [1];
    pos [2] = state [2];

// Convert distance from km to AU

    dist_km = vnorm_c ( pos );
    convrt_c ( dist_km, "KM", "AU", &dist_au );

    }

// Convert time stamp of the data in s back to UTC
    et2utc_c ( et, "ISOC",0,STRLEN,utctim);

// Print time stamp in UTC, angle (x,y,z), distance to the Sun
fprintf(solar_angle,"%s\t %20.6f\t %20.6f\t %20.6f\t %20.6f\n" ,
utctim , angle_degx , angle_degy, angle_degz, dist_au );


      }
      fclose  ( solar_angle );
      return 0;
      }
```

B SPICE: Trajectories

```
*****************************************************************************

SPICE code in c to extract the position of Rosetta relative to 67P
for bound orbits for planing purposes

*****************************************************************************


---------------------------------kernel input-------------------------------
Chury-trajectory.tm contains the kernel input in the following order:

fk: ROS_V17.TF
lsk: NAIF0010.TLS
pck: PCK00010.TPC
pck: ROS_CGS_RSOC_V03.TPC
sclk: ROS_101110_STEP.TSC
spk: roviz_t104_p000_c000_s000_g000_r003_a0_v000.bsp
spk: ORHW_______________00016.BSP
spk: DE405.BSP

The trajectory kernels should be updated if the time range does not match:

spk: roviz_t104_p000_c000_s000_g000_r003_a0_v000.bsp

Time range:
Body: ROSETTA (-226)
      Start of Interval (ET)              End of Interval (ET)
      -----------------------------       -----------------------------
      2014 DEC 01 00:01:06.183            2015 FEB 01 00:01:06.183

------------------------------------------------------------------------------

-------------------------------C-code----------------------------------------

#include <stdio.h>
#include <string.h>
#include "SpiceUsr.h"

#define METAKR "Chury-trajectory.tm"
#define SCLKID -226 // Cassini NAIF ID (aus naif_ids.html) -226 for ROSETTA
#define STRLEN 50 // Lenght of utctim +1!
```

```
int main (void)
      {

      SpiceChar               utctim [STRLEN];
      SpiceChar               utctim_start [STRLEN];
      SpiceChar               utctim_end [STRLEN];
      SpiceChar               start [10];
      SpiceChar               end [10];
      SpiceChar               filename [44];

      SpiceDouble state [6];
      SpiceDouble  et_start;
      SpiceDouble  et_end;
      SpiceDouble  et;
      SpiceDouble ltime;

      SpiceDouble pos [3];
      SpiceDouble dist_m;

      SpiceDouble step;
      SpiceDouble imax;

FILE  *chury_trajectory;

      furnsh_c ( METAKR );

// Give start and end time
      strncpy(utctim_start, "2014-12-01T01:00:00", STRLEN);
      strncpy(utctim_end, "2014-12-31T00:00:00", STRLEN);
      strncpy (start, utctim_start, 10);
      strncpy (end, utctim_end, 10);

      sprintf( filename , "%s-%s-chury_trajectory.dat" , start, end);
      chury_trajectory = fopen ( filename ,"w"); // w :write

// Print used kernels in *.xls file
      fprintf(chury_trajectory,
      "The loaded Kernels are:\n %s\n %s\n %s\n %s\n %s\n %s\n %s\n %s\n\n",
       "kernels/fk/ROS_V17.TF",
"kernels/lsk/NAIF0010.TLS",
"kernels/pck/PCK00010.TPC",
"kernels/pck/ROS_CGS_RSOC_V03.TPC",
"kernels/sclk/ROS_101110_STEP.TSC",
```

```
"kernels/spk/roviz_t104_p000_c000_s000_g000_r003_a0_v000.bsp",
"kernels/spk/ORHW_______________00016.BSP",
"kernels/spk/DE405.BSP");

// Convert start and end time into ET
      utc2et_c( utctim_start, &et_start );
      utc2et_c( utctim_end, &et_end );

// Time step to extract position in s (300 s = 5 min)
      step = 3600;

      imax = (et_end - et_start)/step;
      fprintf(chury_trajectory, "Start time UTC: %s\t End time UTC:
%s\t Step: %f\n", utctim_start, utctim_end, step);
      fprintf(chury_trajectory,"%s\t %s\t %s\t %s\n",
"x [m]","y [m]","z [m]","Distanz [m]");

// Extract position vector (x,y,z) of Rosetta relative to comet
      int i;
      for ( i=0; i< imax ;i++){
      et = (et_start + step*i);

      if( et < et_end )
      {
      spkezr_c( "ROSETTA", et, "67P/C-G_CSO", "LT", "CHURYUMOV-GERASIMENKO",
state, &ltime);

      pos [0] = state [0]*1000.0;
      pos [1] = state [1]*1000.0;
      pos [2] = state [2]*1000.0;

// Calculate distance of Rosetta to comet from position vector
    dist_m = vnorm_c ( pos );
    }
    et2utc_c ( et, "ISOC",0,STRLEN,utctim);

// Print position vector (x,y,z) of Rosetta relative to comet and distance
    fprintf(chury_trajectory,"%f\t %f\t %f\t %f\n" ,
pos[0] , pos[1] , pos[2] , dist_m );
      }
      fclose  ( chury_trajectory );
      return 0;
      }
```

C MCP gain calibration data

The following data files were used to calibrate the gain polynom. The data files are extracted from the folowing recorderfiles:
EGSE1_V7A1FM_ROSINA_DFMS_FM2_GainPolynom_20110622
EGSE1_V7A1FM_ROSINA_DFMS_FM2_GainPolynom_20110809
EGSE1_V7A1FM_ROSINA_DFMS_FM2_GainPolynom_20110830
EGSE1_V7A1FM_ROSINA_DFMS_FM2_GainPolynom_20110808
EGSE1_V7A1FM_ROSINA_DFMS_FM2_GainPolynomIsotopes_20110901

Table C.1: Gainpolynom calibration data recorded 09.08.2011 gain steps 6-16

File name	Gain step
GainPloly_m18_GS06_1.dat	6
GainPloly_m18_GS07_1.dat	7
GainPloly_m18_GS08_1.dat	8
GainPloly_m18_GS09_1.dat	9
GainPloly_m18_GS09_2.dat	9
GainPloly_m16_GS10_1.dat	10
GainPloly_m16_GS10_2.dat	10
GainPloly_m18_GS10_1.dat	10
GainPloly_m16_GS11_1.dat	11
GainPloly_m44_GS11_1.dat	11
GainPloly_m16_GS12_1.dat	12
GainPloly_m44_GS12_1.dat	12
GainPloly_m16_GS13_1.dat	13
GainPloly_m44_GS13_1.dat	13
GainPloly_m16_GS14_1.dat	14
GainPloly_m44_GS14_1.dat	14
GainPloly_m44_GS14_2.dat	14
GainPloly_m44_GS15_1.dat	15
GainPloly_m44_GS16_1.dat	16

Recorderfile:
EGSE1_V7A1FM_ROSINA_DFMS_FM2_GainPolynom_20110809

Table C.2: Gainpolynom calibration data recorded 22.06.2011 gain steps 3-16

File name	Gain step
m44_GS3_1.dat	3
m44_GS3_2.dat	3
m44_GS3_3.dat	3
m44_GS3_4.dat	3
m44_GS4_1.dat	4
m44_GS4_2.dat	4
m44_GS4_3.dat	4
m44_GS4_4.dat	4
m44_GS5_1.dat	5
m44_GS5_2.dat	5
m44_GS5_3.dat	5
m44_GS5_4.dat	5
m44_GS6_1.dat	6
m44_GS6_2.dat	6
m44_GS6_3.dat	6
m44_GS6_4.dat	6
m44_GS7_1.dat	7
m44_GS7_2.dat	7
m44_GS7_3.dat	7
m44_GS7_4.dat	7
m44_GS8_4.dat	8
GainPoly_m20_GS11_1.dat	11
GainPoly_m20_GS11_2.dat	11
GainPoly_m20_GS12_1.dat	12
GainPoly_m20_GS12_2.dat	12
GainPoly_m20_GS13_1.dat	13
GainPoly_m20_GS13_2.dat	13
GainPoly_m20_GS14_1.dat	14
GainPoly_m20_GS14_2.dat	14
GainPoly_m34_GS14_1.dat	14
GainPoly_m34_GS15_1.dat	15
GainPoly_m34_GS15_2.dat	15
GainPoly_m34_GS16_1.dat	16

Recorderfile:
EGSE1_V7A1FM_ROSINA_DFMS_FM2_GainPolynom_20110622

D Recorder files of the calibration

The calibration measurements are recorded with GSEOS in the following recorderfiles and data can be extracted thereof:

Noble Gases:
EGSE1_V7AEFM_ROSINA_DFMS_FM2_Ne-sensitivity_20130405

EGSE1_V7AEFM_ROSINA_DFMS_FM2_Ar-isotopes_20130404

EGSE1_V7A9FM_ROSINA_DFMS_FM2_Kr-sensitivity_20120228
EGSE1_V7A9FM_ROSINA_DFMS_FM2_Kr-sensitivity_20120229
EGSE1_V7A9FM_ROSINA_DFMS_FM2_Kr-sensitivity_20120312
EGSE1_V7A9FM_ROSINA_DFMS_FM2_Kr-sensitivity_20120315

EGSE1_V7A9FM_ROSINA_DFMS_FM2_Xe-sensitivity_20120710

Water:
EGSE1_V7A9FM_ROSINA_DFMS_FM2_H2O_20120402
EGSE1_V7A9FM_ROSINA_DFMS_FM2_H2O_20120403
EGSE1_V7A9FM_ROSINA_DFMS_FM2_H2O_20120404
EGSE1_V7A9FM_ROSINA_DFMS_FM2_H2O_20120405

Nitrogen:
EGSE1_V7A9FM_ROSINA_DFMS_FM2_N2-sensitivity_20120423
EGSE1_V7A9FM_ROSINA_DFMS_FM2_N2-sensitivity_20120424

Carbon-dioxide:
EGSE1_V7A9FM_ROSINA_DFMS_FM2_CO2-sensitivity_20120503
EGSE1_V7A9FM_ROSINA_DFMS_FM2_CO2-sensitivity_20120507
EGSE1_V7AFFM_ROSINA_DFMS_FM2_CO2_20130416

Alkanes:
EGSE1_V7A9FM_ROSINA_DFMS_FM2_CH4-sensitivity_20120607
EGSE1_V7A9FM_ROSINA_DFMS_FM2_CH4-sensitivity_20120608

EGSE1_V7A9FM_ROSINA_DFMS_FM2_C2H6-sensitivity_20120711
EGSE1_V7AAFM_ROSINA_DFMS_FM2_C2H6-sensitivity_20120712

EGSE1_V7A9FM_ROSINA_DFMS_FM2_C3H8-sensitivity_20120612
EGSE1_V7A9FM_ROSINA_DFMS_FM2_C3H8-sensitivity_20120613
EGSE1_V7AEFM_ROSINA_DFMS_FM2_C3H8-sensitivity_20130408
EGSE1_V7AEFM_ROSINA_DFMS_FM2_C3H8-sensitivity_20130409

EGSE1_V7AFFM_ROSINA_DFMS_FM2_C4H10_20130411
EGSE1_V7AFFM_ROSINA_DFMS_FM2_C4H10_20130412
EGSE1_V7AFFM_ROSINA_DFMS_FM2_C4H10_20130415

Alkene:
EGSE1_V7A9FM_ROSINA_DFMS_FM2_C2H4-sensitivity_20120605
EGSE1_V7A9FM_ROSINA_DFMS_FM2_C2H4-sensitivity_20120606

Gas mixtures:
EGSE1_V7AFFM_ROSINA_DFMS_FM2_SW-test_20130411

EGSE1_V7A9FM_ROSINA_DFMS_FM2_ROSINA-Quiz_20120509
EGSE1_V7A9FM_ROSINA_DFMS_FM2_ROSINA-Quiz_20120510

EGSE1_V7AFFM_ROSINA_DFMS_FM2_Ne-Ar-Kr-Xe_20130423

Electron energy stepping:
EGSE1_V7A9FM_ROSINA_DFMS_FM2_electron-energy-stepping_20120508

E Fragmentation pattern for MCP/LEDA and CEM (f_i) and possible yield corrections

Table E.3: H_2O fragmentation pattern for CEM and NIST values

Species	f_{H_2O}	Δf_{H_2O}	f_{H_2O} [%]	Δf_{H_2O} [%]	NIST
O	0.015	0.010	1.89	68.80	0.007
OH	0.188	0.014	23.56	7.41	0.174
H_2O	0.797	0.024	100.00	3.04	0.819

Table E.4: H_2O fragmentation pattern and possible yield corrections for MCP/LEDA

Species	f_{H_2O}	Δf_{H_2O}	f_{H_2O} [%]	Δf_{H_2O} [%]	yield
O	0.021	0.011	2.61	52.75	2.017
OH	0.187	0.005	23.67	2.55	1.557
H_2O	0.792	0.011	100.00	1.39	1.808

Table E.5: N_2 fragmentation pattern for CEM and NIST values

Species	f_{N_2}	Δf_{N_2}	f_{N_2} [%]	Δf_{N_2} [%]	NIST
N	0.040	0.022	4.21	54.81	0.121
N_2	0.960	0.022	100.00	2.31	0.879

Table E.6: N_2 fragmentation pattern and possible yield corrections for MCP/LEDA

Species	f_{N_2}	Δf_{N_2}	f_{N_2} [%]	Δf_{N_2} [%]	yield
N	0.050	0.010	5.23	20.60	0.933
N_2	0.950	0.010	100.00	1.08	0.684

Table E.7: CO_2 fragmentation pattern for CEM and NIST values

Species	f_{CO_2}	Δf_{CO_2}	f_{CO_2} [%]	Δf_{CO_2} [%]	NIST
C	0.012	0.003	1.47	21.03	0.067
O	0.062	0.012	7.32	19.77	0.074
CO_2^{++}	0.000	0.000	0.05	89.42	0.015
CO	0.078	0.011	9.24	13.47	0.075
CO_2	0.847	0.008	100.00	0.90	0.769

Table E.8: CO_2 fragmentation pattern and possible yield corrections for MCP/LEDA

Species	f_{CO_2}	Δf_{CO_2}	f_{CO_2} [%]	Δf_{CO_2} [%]	yield
O	0.121	0.014	15.57	11.35	1.958
CO_2^{++}	0.000	0.000	0.06	95.93	1.130
CO	0.099	0.006	12.72	6.30	1.266
CO_2	0.779	0.016	100.00	2.08	0.920

Table E.9: CH_4 fragmentation pattern for CEM and NIST values

Species	f_{CH_4}	Δf_{CH_4}	f_{CH_4} [%]	Δf_{CH_4} [%]	NIST
^{12}C	0.004	0.001	0.56	24.92	0.017
^{12}CH	0.015	0.003	2.41	18.66	0.048
$^{12}CH_2$	0.024	0.016	3.78	66.31	0.091
$^{12}CH_3$	0.317	0.051	49.59	15.97	0.397
$^{12}CH_4$	0.640	0.064	100.00	10.04	0.447

Table E.10: CH_4 fragmentation pattern and possible yield corrections for MCP/LEDA

Species	f_{CH_4}	Δf_{CH_4}	f_{CH_4} [%]	Δf_{CH_4} [%]	yield
^{12}CH	0.019	0.011	3.56	61.63	1.605
$^{12}CH_2$	0.031	0.012	5.87	40.25	1.803
$^{12}CH_3$	0.429	0.016	82.25	3.71	1.623
$^{12}CH_4$	0.522	0.011	100.00	20.10	2.106

Table E.11: C_2H_6 fragmentation pattern for CEM and NIST values

Species	$f_{C_2H_6}$	$\Delta f_{C_2H_6}$	$f_{C_2H_6}$ [%]	$\Delta f_{C_2H_6}$ [%]	NIST
^{12}C	0.001	0.000	0.18	39.13	0.002
^{12}CH	0.002	0.001	0.50	32.21	0.005
$^{12}CH_2$	0.008	0.002	1.79	26.26	0.014
$^{12}CH_3$	0.026	0.007	5.69	25.84	0.020
$^{12}CH_4$	0.005	0.000	1.00	9.92	0.000
$^{12}C_2$	0.001	0.000	0.31	8.04	0.002
$^{12}C_2H$	0.012	0.001	2.65	7.71	0.016
$^{12}C_2H_2$	0.102	0.008	22.49	8.13	0.107
$^{12}C_2H_3$	0.135	0.009	29.75	6.93	0.153
$^{12}C_2H_4$	0.454	0.020	100.00	4.50	0.460
$^{12}C_2H_5$	0.102	0.002	22.52	2.19	0.099
$^{12}C_2H_6$	0.148	0.008	32.72	5.34	0.121

Table E.12: C_2H_6 fragmentation pattern and possible yield corrections for MCP/LEDA

Species	$f_{C_2H_6}$	$\Delta f_{C_2H_6}$	$f_{C_2H_6}$ [%]	$\Delta f_{C_2H_6}$ [%]	yield
^{12}CH	0.003	0.001	0.59	26.30	1.471
$^{12}CH_2$	0.012	0.007	2.32	59.32	1.528
$^{12}CH_3$	0.043	0.023	8.16	53.62	1.345
$^{12}CH_4$	0.000	0.005	0.00	20.10	1.837
$^{12}C_2$	0.002	0.000	0.29	19.09	1.918
$^{12}C_2H$	0.012	0.001	2.25	12.40	2.100
$^{12}C_2H_2$	0.114	0.024	21.59	21.02	1.909
$^{12}C_2H_3$	0.095	0.012	17.96	12.83	2.979
$^{12}C_2H_4$	0.528	0.028	100.00	5.30	1.782
$^{12}C_2H_5$	0.086	0.004	16.26	4.99	2.468
$^{12}C_2H_6$	0.106	0.017	20.10	15.76	2.911

Table E.13: C_3H_8 fragmentation pattern for CEM and NIST values

Species	$f_{C_3H_8}$	$\Delta f_{C_3H_8}$	$f_{C_3H_8}$ [%]	$\Delta f_{C_3H_8}$ [%]	NIST
^{12}C	0.000	0.000	0.19	62.94	0.001
^{12}CH	0.001	0.000	0.60	27.12	0.002
$^{12}CH_2$	0.004	0.001	1.82	26.49	0.007
$^{12}CH_3$	0.025	0.003	10.66	13.08	0.022
$^{12}CH_4$	0.013	0.001	5.82	9.66	0.001
$^{12}C_2$	0.001	0.000	0.34	7.88	0.000
$^{12}C_2H$	0.003	0.000	1.40	10.00	0.002
$^{12}C_2H_2$	0.027	0.002	11.83	6.30	0.028
$^{12}C_2H_3$	0.083	0.002	35.95	2.86	0.129
$^{12}C_2H_4$	0.144	0.024	62.27	16.66	0.180
$^{12}C_2H_5$	0.231	0.025	100.00	10.66	0.307
$^{13}C^{12}CH_5$	0.006	0.001	2.16	11.65	0.007
$^{12}C_3$	0.000	0.000	0.08	13.37	0.001
$^{12}C_3H$	0.005	0.000	1.96	10.60	0.009
$^{12}C_3H_2$	0.011	0.002	4.67	21.75	0.016
$^{12}C_3H_3$	0.061	0.017	26.49	27.14	0.058
$^{12}C_3H_4$	0.011	0.002	4.97	21.46	0.009
$^{12}C_3H_5$	0.060	0.011	26.15	18.83	0.041
$^{12}C_3H_6$	0.023	0.005	9.80	20.56	0.018
$^{12}C_3H_7$	0.125	0.006	54.12	4.80	0.071
$^{12}C_3H_8$	0.166	0.004	71.78	2.49	0.084
$^{13}C^{12}C_2H_8$	0.005	0.001	2.15	13.25	0.002

Table E.14: C_3H_8 fragmentation pattern and possible yield corrections for MCP/LEDA

Species	$f_{C_3H_8}$	$\Delta f_{C_3H_8}$	$f_{C_3H_8}$ [%]	$\Delta f_{C_3H_8}$ [%]	yield
^{12}CH	0.002	0.0004	0.82	19.74	1.61
$^{12}CH_2$	0.007	0.0024	2.45	35.91	1.80
$^{12}CH_3$	0.044	0.0080	15.73	18.34	1.62
$^{12}CH_4$	0.016	0.0069	5.62	44.61	2.11
$^{12}C_2$	0.001	0.0002	0.36	19.29	2.20
$^{12}C_2H$	0.004	0.0011	1.54	24.97	2.05
$^{12}C_2H_2$	0.041	0.0010	14.74	2.35	1.95
$^{12}C_2H_3$	0.128	0.0217	46.37	16.89	1.90
$^{12}C_2H_4$	0.198	0.0178	71.66	8.98	2.14
$^{12}C_2H_5$	0.277	0.0260	100.00	9.38	2.39
$^{13}C^{12}CH_5$	0.006	0.0014	2.16	23.68	2.39
$^{12}C_3$	0.000	0.0000	0.03	36.80	6.46
$^{12}C_3H$	0.002	0.0004	0.84	16.35	5.44
$^{12}C_3H_2$	0.007	0.0005	2.41	7.77	4.11
$^{12}C_3H_3$	0.042	0.0138	15.32	32.62	4.10
$^{12}C_3H_4$	0.006	0.0006	2.17	10.13	4.90
$^{12}C_3H_5$	0.035	0.0020	12.73	5.80	4.42
$^{12}C_3H_6$	0.013	0.0007	4.67	5.44	4.25
$^{12}C_3H_7$	0.074	0.0065	26.62	8.84	4.85
$^{12}C_3H_8$	0.098	0.0040	35.35	4.11	4.83
$^{13}C^{12}C_2H_8$	0.003	0.0004	1.15	14.13	4.83

Table E.15: C_4H_{10} fragmentation pattern for CEM and NIST values

Species	$f_{C_4H_{10}}$	$\Delta f_{C_4H_{10}}$	$f_{C_4H_{10}}$ [%]	$\Delta f_{C_4H_{10}}$ [%]	NIST
^{12}C	0.000	0.000	0.12	60.50	0.000
^{12}CH	0.000	0.000	0.01	127.87	0.001
$^{12}CH_2$	0.001	0.000	0.29	20.54	0.003
$^{12}CH_3$	0.002	0.000	0.59	16.01	0.019
$^{12}CH_4$	0.015	0.001	4.22	6.82	0.000
$^{12}C_2$	0.001	0.000	0.28	16.49	0.000
$^{12}C_2H$	0.004	0.002	1.22	35.73	0.001
$^{12}C_2H_2$	0.027	0.010	7.57	35.85	0.019
$^{12}C_2H_3$	0.073	0.014	20.18	19.00	0.124
$^{12}C_2H_4$	0.081	0.026	22.45	31.63	0.103
$^{12}C_2H_5$	0.105	0.029	29.24	27.46	0.139
$^{12}C_2H_6$	0.003	0.001	0.91	29.97	0.003
$^{12}C_3$	0.000	0.000	0.00	30.50	0.000
$^{12}C_3H$	0.002	0.001	0.56	66.42	0.002
$^{12}C_3H_2$	0.003	0.000	0.81	14.24	0.006
$^{12}C_3H_3$	0.032	0.008	8.94	25.38	0.044
$^{12}C_3H_4$	0.006	0.001	1.73	12.64	0.006
$^{12}C_3H_5$	0.096	0.018	26.64	19.04	0.092
$^{12}C_3H_6$	0.055	0.008	15.33	13.91	0.039
$^{12}C_3H_7$	0.359	0.039	100.00	10.88	0.321
$^{12}C_3H_8$	0.018	0.003	4.89	14.85	0.011
$^{12}C_4H$	0.000	0.000	0.14	12.49	0.001
$^{12}C_4H_2$	0.002	0.000	0.55	19.04	0.004
$^{12}C_4H_3$	0.002	0.000	0.60	13.82	0.003
$^{12}C_4H_4$	0.001	0.000	0.23	26.44	0.001
$^{12}C_4H_5$	0.003	0.001	0.74	33.89	0.003
$^{12}C_4H_6$	0.001	0.000	0.30	12.82	0.001
$^{12}C_4H_7$	0.004	0.001	1.06	19.17	0.003
$^{12}C_4H_8$	0.003	0.001	0.85	34.53	0.003
$^{12}C_4H_9$	0.010	0.002	2.70	19.71	0.008
$^{12}C_4H_{10}$	0.077	0.012	21.31	15.82	0.039

Table E.16: C_4H_{10} fragmentation pattern and possible yield corrections for MCP/LEDA

Species	$f_{C_4H_{10}}$	$\Delta f_{C_4H_{10}}$	$f_{C_4H_{10}}$ [%]	$\Delta f_{C_4H_{10}}$ [%]	yield
^{12}CH	0.002	0.000	0.75	13.25	1.43
$^{12}CH_2$	0.004	0.000	1.50	6.88	1.47
$^{12}CH_3$	0.037	0.007	12.68	18.82	1.33
$^{12}CH_4$	0.019	0.004	6.58	21.82	1.73
$^{12}C_2$	0.002	0.001	0.61	31.95	1.84
$^{12}C_2H$	0.006	0.003	2.22	39.65	2.05
$^{12}C_2H_2$	0.041	0.013	13.99	30.67	1.95
$^{12}C_2H_3$	0.115	0.006	39.39	5.15	1.90
$^{12}C_2H_4$	0.120	0.026	40.98	21.87	2.14
$^{12}C_2H_5$	0.126	0.010	43.16	7.63	2.39
$^{12}C_2H_6$	0.003	0.000	0.93	15.35	3.34
$^{12}C_3$	0.001	0.000	0.35	22.18	2.79
$^{12}C_3H$	0.003	0.001	0.92	24.44	6.53
$^{12}C_3H_2$	0.028	0.001	9.46	4.94	3.24
$^{12}C_3H_3$	0.005	0.000	1.55	1.95	3.46
$^{12}C_3H_4$	0.083	0.014	28.50	17.15	4.23
$^{12}C_3H_5$	0.046	0.006	15.67	12.81	3.58
$^{12}C_3H_6$	0.292	0.030	100.00	10.24	3.88
$^{12}C_3H_7$	0.013	0.004	4.37	32.79	3.93
$^{12}C_3H_8$	0.000	0.000	0.12	26.57	4.34
$^{12}C_4H$	0.000	0.000	0.09	17.80	6.02
$^{12}C_4H_2$	0.001	0.000	0.50	11.36	4.20
$^{12}C_4H_3$	0.001	0.000	0.49	3.30	4.64
$^{12}C_4H_4$	0.001	0.000	0.17	14.13	4.86
$^{12}C_4H_5$	0.002	0.000	0.53	7.72	5.09
$^{12}C_4H_6$	0.001	0.000	0.18	12.97	6.64
$^{12}C_4H_7$	0.002	0.000	0.63	18.05	6.37
$^{12}C_4H_8$	0.001	0.000	0.50	16.19	6.09
$^{12}C_4H_9$	0.005	0.001	1.65	22.25	6.32
$^{12}C_4H_{10}$	0.040	0.007	13.77	16.21	6.15

Table E.17: C_2H_4 fragmentation pattern for CEM and NIST values

Species	$f_{C_2H_4}$	$\Delta f_{C_2H_4}$	$f_{C_2H_4}$ [%]	$\Delta f_{C_2H_4}$ [%]	NIST
^{12}C	0.003	0.001	0.56	21.60	0.002
^{12}CH	0.006	0.001	1.21	18.36	0.004
$^{12}CH_2$	0.008	0.002	1.66	30.66	0.009
$^{12}CH_3$	0.005	0.003	1.04	58.80	0.001
$^{12}C_2$	0.013	0.002	2.90	18.53	0.010
$^{12}C_2H$	0.058	0.016	12.47	26.96	0.034
$^{12}C_2H_2$	0.245	0.018	53.10	7.17	0.229
$^{12}C_2H_3$	0.189	0.012	40.87	6.60	0.269
$^{12}C_2H_4$	0.462	0.020	100.00	4.35	0.432

Table E.18: C_2H_4 fragmentation pattern and possible yield corrections for MCP/LEDA

Species	$f_{C_2H_4}$	$\Delta f_{C_2H_4}$	$f_{C_2H_4}$ [%]	$\Delta f_{C_2H_4}$ [%]	yield
^{12}CH	0.011	0.006	2.42	55.48	1.156
$^{12}CH_2$	0.009	0.003	1.92	37.43	1.803
$^{12}CH_3$	0.006	0.004	1.33	71.58	1.623
$^{12}C_2$	0.012	0.003	2.74	21.76	2.201
$^{12}C_2H$	0.056	0.018	12.66	32.21	2.052
$^{12}C_2H_2$	0.253	0.020	56.97	7.90	1.945
$^{12}C_2H_3$	0.200	0.018	45.04	9.11	1.896
$^{12}C_2H_4$	0.444	0.021	100.00	4.69	2.088

F Pressure correction factor for pressure sensor

The pressure measurements with the stabil ion gauge (Series 370 STABIL-ION) are species dependent. The pressure measurements are nominal performed for N_2, while a correction factor is calibrated for other species. The pressure gauge is designed according to a Bayard-Albert ionization gauge with and accuracy of 6–14%. A detailed documentation can be found in [Granville-Phillips, 2007].

Table F.19: Scale factors to correct the N_2 calibrated pressure readings for the Granville-Phillips SABIL-ION Vacuum measurement System [Granville-Phillips, 2007].

GAS	Scale Factor
N_2	1.00
He	5.56
Ne	3.33
Ar	0.775
Kr	0.515
Xe	0.348
H_2O	0.893
CO_2	0.704
CO	0.952

References

[A'Hearn et al., 2011] A'Hearn, M., Belton, M. J. S., Delamere, W. A., Feaga, L. M., Hampton, D., Kissel, J., Klaasen, K. P., McFadden, L. A., Meech, K. J., Melosh, H. J., Schultz, P. H., Sunshine, J. M., Thomas, P. C., Veverka, J., Wellnitz, D. D., Yeomans, D. K., Besse, S., Bodewits, D., Bowling, T. J., Carcich, B. T., Collins, S. M., Farnham, T. L., Groussin, O., Hermalyn, B., Kelley, M. S., Li, J.-Y., Lindler, D. J., Lisse, C. M., McLaughlin, S. A., Merlin, F., Protopapa, S., Richardson, J. E., and Williams, J. L. (2011). EPOXI at Comet Hartley 2. *Science*, 332:1396–1400.

[Altwegg, 2008a] Altwegg, K. (2008a). Memo DFMS FS sensitivites before launch and in flight. Technical report, University of Bern.

[Altwegg, 2008b] Altwegg, K. (2008b). Some remarks to the document: Spontaneous sensitivity changes of DFMS FS and I_{trap}/I_{total} as monitor of sensitivity. Technical report, University of Bern.

[Arpigny et al., 2003] Arpigny, C., Jehin, E., Manfroid, J., Hutsemékers, D., Schulz, R., Stüwe, J., J.-M.Zucconi, and Ilyin, I. (2003). Anomalous nitrogen isotope ratio in comets. *Science*, 301(5639):1522–1524.

[Balsiger et al., 2007] Balsiger, H., Altwegg, K., Bochsler, P., Eberhardt, P., Fischer, J., Graf, S., Jäckel, A., Kopp, E., Langer, U., Mildner, M., Müller, J., Riesen, T., Rubin, M., Scherer, S., Wurz, P., Wüthrich, S., Arijs, E., Delanoye, S., Keyser, J. D., Neefs, E., Nevejans, D., Rème, H., Aoustin, C., Mazelle, C., Médale, J. L., Sauvaud, J. A., Berthelier, J. J., Bertaux, J. L., Duvet, L., Illiano, J. M., Fuselier, S. A., Ghielmetti, A. G., Magoncelli, T., Shelley, E. G., Korth, A., Heerlein, K., Lauche, H., Livi, S., Loose, A., Mall, U., Wilken, B., Gliem, F., Fiethe, B., Gombosi, T. I., Block, B., Carignan, G. R., Fisk, L. A., Waite, J. H., Young, D. T., and Wollnik, H. (2007). ROSINA-Rosetta Orbiter Spectrometer for Ion and Neutral Analysis. *Space Science Review*, 128:745–801.

[Balsiger et al., 1995] Balsiger, H., Altwegg, K., and Geiss, J. (1995). D/H and $^{18}O/^{16}O$ ratio in the hydronium ion and in neutral water from in situ ion measurements in comet Halley. *Journal Geophysical Research*, 100:5827–5834.

[Berner et al., 2002] Berner, C., Bond, P., Bourillet, L., van Casteren, J., Ellwood, J., Kasper, M., Kletzkine, P., Schulz, R., Schwehm, G., and Warhaut, M. (2002). *Rosetta: ESA's Comet Chaser, ESA Bulletin, 112.*

[Bockelée-Morvan et al., 1998] Bockelée-Morvan, D., Gautier, D., Lis, D. C., Young, K., Keene, J., Phillips, T., Owen, T., Crovisier, J., Goldsmith, P. F., Bergin, E. A., Despois, D., and Wootten, A. (1998). Deuterated Water in the Comet C/1996 B2 (Hyakutake) and Its Implications for the Origin of Comets. *Icarus*, 133:147–162.

[Bockelée-Morvan et al., 2004] Bockelée-Morvan, D., Mumma, M. J., and Weaver, H. A. (2004). *Comet II*, chapter The Composition of Cometary Volatiles, pages 391–423. The University of Arizona Press and Tucson.

[Bockelée-Morvan et al., 2008] Bockelée-Morvan, D., N. Biver, E. J., Cochran, A. L., Wiesemeyer, H., J. Manfroid, D. H., Arpigny, C., Boissier, J., Cochran, W., Colom, P., Crovisier, J., Milutinovic, N., Moreno, R., Prochaska, J. X., Ramirez, I., Schulz, R., and Zucconi, J.-M. (2008). Large Excess of Heavy Nitrogen in Both Hydrogen Cyanide and Cyanogen from Comet 17P/Holmes . *Astrophysical Journal*, 679:L49–L52.

[Brown et al., 2004] Brown, M. E., Trujillo, C., and Rabinowitz, D. (2004). Discovery of a candiate inner Oort cloud planetoid. *The Astrophysical Journal*, 617:645–649.

[Cisela and Lauretta, 2005] Cisela, F. and Lauretta, D. (2005). Radial migration and dehydration of phyllosilicates in the solar nebula. *Earth and Planetary Science Letters*, 231:1–8.

[Combi et al., 2004] Combi, M. R., Harris, M., and Smyth, W. H. (2004). *Comet II*, chapter Gas Dynamics and Kinetcs in the Cometary Coma: Theory and Observations, pages 523–550. The University of Arizona Press and Tucson.

[Controller, 2001] Controller, M.-G. (2001). *Instruction Manual to Multi-Gauge Controller Part No. L8350301.*

[Crifo and Rodionov, 1997] Crifo, J. F. and Rodionov, A. V. (1997). The Dependence of the Circumnuclear Coma Structure on the Properties of the Nucleus. *Icarus*, 127 (2):319–353.

[de Pater and Lissauer, 2001] de Pater, I. and Lissauer, J. J. (2001). *Planetary Sciences.* Cambridge University Press.

[Eberhardt, 2008a] Eberhardt, P. (2008a). DFMS FS sensitivity in flight. Technical report, University of Bern.

[Eberhardt, 2008b] Eberhardt, P. (2008b). Spontaneous sensitivity changes of DFMS FS and I_{trap}/I_{total} as monitor of sensitivity. Technical report, University of Bern.

[Eberhardt et al., 1988] Eberhardt, P., Krankowsky, D., Schulte, W., Dolder, U., Lämmerzahl, P., Berthelier, J., Woweries, J., Stubbemann, U., Hodges, R., Hoffman, J., et al. (1988). The CO and N_2 abundance in comet P/Halley. *Astronomy and Astrophysics*, 187:481–484.

[Eberhardt et al., 1995] Eberhardt, P., Reber, M., Krankowsky, D., and Hodges, R. R. (1995). The D/H and $^{18}O/^{16}O$ ratios in water from comet 1P/Halley. *Astronomy and Astrophysics*, 302:301–316.

[Feldman et al., 2004] Feldman, P. D., Cochran, A. L., and Combi, M. C. (2004). *Comet II*, chapter Spectroscopic investigations of fragment species in the coma, pages 427–448. The University of Arizona Press and Tucson.

[Glassmeier et al., 2009] Glassmeier, K.-H., Boehnhardt, H., Koschny, D., Kührt, E., Richter, I., Schulz, R., and Alexander, C. (2009). *ROSETTA: ESA's Mission to the Origin of the Solar System*, chapter The ROSETTA Mission: Flying Towards the Origin of the Solar System, pages 1–20. Springer.

[Gomes et al., 2005] Gomes, R., Levison, H. F., Tsiganis, K., and Morbidelli, A. (2005). Origin of the cataclysmic Late Heavy Bombardment period of the terrestrial planets. *Nature*, 435:466–469.

[Granville-Phillips, 2007] Granville-Phillips (2007). *Instruction Manual to Granville-Phillips Series 370 Stabil-Ion Vaccum Measurement Controller.*

[Handbook of Chemistry and Physics, 2012] Handbook of Chemistry and Physics (2012). *Davis R. Lide and Taylor and Francis*. CRC Press.

[Hartogh et al., 2011] Hartogh, P., Lis, D. C., Bockelée-Morvan, D., de Val-Borro, M., Biver, N., Küppers, M., Emprechtinger, M., Bergin, E. A., Crovasier, J., Rengel, M., Moreno, R., Szutowicz, S., and Blake, G. A. (2011). Ocean-like water in the Jupiter-family comet 103P/Hartley 2. *Nature*, 478:218–220.

[Haser, 1957] Haser, L. (1957). Distribution d'intensite danls la tete d'une comete. *Bull. Acad. R. de Belgique*, Classe de Sci. 43(5):740–750.

[Hässig et al., 2013] Hässig, M., Altwegg, K., Balsiger, H., Berthelier, J., Calmonte, U., Combic, M., Keyser, J. D., Fiethe, B., Fuselier, S., and Rubin, M. (2013). ROSINA/DFMS capabilities to measure isotopic ratios in water at comet 67P/Churyumov-Gerasimenko. *Planetary and Space Science*, page DOI: 10.1016/j.pss.2013.05.014.

[Irvine and Lunine, 2004] Irvine, W. M. and Lunine, J. I. (2004). *Comet II*, chapter The Cycle of Matter in Our Galaxy: From Clouds to Comets, pages 25–31. The University of Arizona Press and Tucson.

[Jewitt et al., 2008] Jewitt, D., Morbidelli, A., and Rauer, H. (2008). *Trans-Neptunian Objects and Comets*. Springer.

[Johnson and Nier, 1953] Johnson, E. and Nier, A. (1953). Angular aberrations in sector shaped electromagnetic lenses for focusing beams of charged particles. *Physicsal Review*, 91:10–17.

[JPL, 2013] JPL (2013). Jet Propulsion Laboratory, California Institute of Technology, Small-Body Database Browser.
$http : //ssd.jpl.nasa.gov/sbdb.cgi?sstr = 67P; orb = 1; cov = 0; log = 0; cad = 0elem$
last compiled 05.05.2013.

[Keller et al., 2010] Keller, H. U., Barbieri, C., Koschny, D., Lamy, P., Rickman, H., Rodrigo, R., Sierks, H., AHearn, M. F., Angrilli, F., Barucci, M. A., Bertaux, J.-L., Cremonese, G., Deppo, V. D., Davidsson, B., Cecco, M. D., Debei, S., Fornasier, S., Fulle, M., Groussin, O., Gutierrez, P. J., Hviid, S. F., Ip, W.-H., Jorda, L., Knollenberg, J., Kramm, J. R., Kührt, E., Küppers, M., Lara, L.-M., Lazzarin, M., Moreno, J. L., Marzari, F., Michalik, H., Naletto, G., Sabau, L., Thomas, N., Wenzel, K.-P., Bertini, I., Besse, S., Ferri, F., Kaasalainen, M., Lowry, S., Marchi, S., Mottola, S., Sabolo, W., Schröder, S. E., Spjuth, S., and Vernazza, P. (2010). E-Type Asteroid (2867) Steins as Imaged by OSIRIS on Board Rosetta. *Science*, 327:190–193.

[Krasnopolsky and Mumma, 2001] Krasnopolsky, V. A. and Mumma, M. J. (2001). Sepctroscopy of Comet Hyakutake at 80-700 Å: First detection of solar wind charge transfer emission. *Astrophysical Journal*, 549:629–634.

[Krasnopolsky et al., 1997] Krasnopolsky, V. A., Mumma, M. J., Abott, M., Flynn, B. C., Meech, K. J., Yeomans, D. K., Feldman, P. D., and Cosmivici, C. B. (1997). Detection of soft X-rays as sensitive search for noble gases in comet Hale-Bopp (C/1995 O1). *Science*, 277:1488–1491.

[Lamy et al., 2009] Lamy, P. L., Toth, I., Davidsson, B. J. R., Groussin, O., Gutiérez, P., Jorda, L., Kaasalainen, M., Lowry, S. C., Schulz, R., Alexander, C., Boehnhart, H., and Glassmeier, K.-H. (2009). *ROSETTA: ESA's Mission to the Origin of the Solar System*, chapter The Nucleus of Comet 67P/Churyumov-Gerasimenko, pages 21–54. Springer.

[Langer, 2003a] Langer, U. (2003a). DFMS-FM and static mode calibration. Technical report, University of Bern.

[Langer, 2003b] Langer, U. (2003b). DFMS-FS and static mode calibration. Technical report, University of Bern.

[Langer et al., 2003] Langer, U., Altwegg, K., Balsiger, H., Berthelier, J.-J., Eberhardt, P., Fiethe, B., Fischer, J., Fuselier, S. A., Gombosi, T. I., Illiano, J.-M., Korth, A., Kopp, E., Nevejans, D., Neefs, E., and Rubin, M. (2003). Calibration Report of DFMS-FS Static Mode Calibration. Technical report, University of Bern.

[Lara et al., 2010] Lara, L. M., Lin, Z.-Y., Rodrigo, R., and Ip, W.-H. (2010). 67P/Churyumov-Gerasimenko activity evolution during its last perihelion before the Rosetta encounter. *Astronomy and Astrophysics*, 525:1–8.

[Meier et al., 1993] Meier, R, Eberhardt, and P (1993). Velocity and ion species dependence of the gain of microchannel plates. *International Journal of Mass Spectrometry and Ion Processes*, 123(1):19–27.

[Meier et al., 1998a] Meier, R., Owen, T. C., Matthews, H. E., Jewitt, D. C., Bockelée-Morvan, D., Biver, N., Crovisier, J., and Gautier, D. (1998a). A determination of the HDO/H_2O Ratio in Comet C/1995 O1 (Hale-Bopp). *Science*, 279:842–844.

[Meier et al., 1998b] Meier, R., Owen, T. C., Matthews, H. E., Jewitt, D. C., Senay, M., Bockelée-Morvan, D., Biver, N., Crovisier, J., and Gautier, D. (1998b). Deuterium in Comet C/1995 O1 (Hale-Bopp): Detection of DCN. *Science*, 279:1707–1710.

[Morbidelli and Brown, 2004] Morbidelli, A. and Brown, M. E. (2004). *Comet II*, chapter The Kuiper Belt and the Primordial Evolution of the Solar System, pages 175–192. The University of Arizona Press and Tucson.

[Morbidelli et al., 2005] Morbidelli, A., Levison, H. F., Tsiganis, K., and Gomes, R. (2005). Chaotic capture of Jupiter's Trojan asteroids in the early Solar System. *Nature*, 435:462–465.

[Moss et al., 1995] Moss, G. P., Smith, P. A. S., Tavernier, D., et al. (1995). Glossary of class names of organic compounds and reactivity intermediates based on structure (IUPAC Recommendations 1995). *Pure and applied chemistry*, 67(8):1307–1375.

[Neefs et al., 2002] Neefs, E., Illiano, J.-M., and Nevejans, D. (2002). DFMS MCP-LEDA detector calibration in CASYMS and Flight Spare model. Technical report, Belgian Institute for Space Aeronomy (BIRA-IASB).

[Neefs et al., 2004] Neefs, E., Illiano, J.-M., and Nevejans, D. (2004). DFMS Detector User Manual FS version (in flight). Technical report, Belgian Institute for Space Aeronomy (BIRA-IASB).

[Nevejans et al., 2002] Nevejans, D., Neefs, E., Kavadias, S., Merken, P., and Hoof, C. V. (2002). The leda512 integrated circuit anode array for the analog recording of mass spectra. *International Journal of Mass Spectrometry*, 215:77–88.

[Nevejans et al., 2001] Nevejans, D., Neefs, E., Riondato, J., and Illiano, J.-M. (2001). DFMS MCP-LEDA detector calibration in CASYMS and Flight model. Technical report, Belgian Institute for Space Aeronomy (BIRA-IASB).

[NIST,] NIST. NIST Chemistry WebBook, NIST Standard Reference Database Number 69. $http://webbook.nist.gov/chemistry/$ last compiled 05.06.2013.

[Orient and Srivastava, 1987] Orient, O. J. and Srivastava, S. K. (1987). Electron impact ionisation of H_2O, CO, CO_2 and CH_4. *Journal of Physics B: Atomic and Molecular and Optical Physics*, 20:3923–3936.

[Oró, 1961] Oró, J. (1961). Comets and the formation of biochemical compounds on the primitive Earth. *Nature*, 290:389–390.

[Penn State University, 2013] Penn State University (2013). Departement of Astronomy and Atrophysics.
$http://www2.astro.psu.edu/users/niel/astro1/slideshows/class43/slides-43.html$.

[Rao et al., 1995] Rao, M. V. V. S., Iga, I., and Srivastava, S. K. (1995). Ionization cross-sections for the production of positive ions from $H2O$ by electron impact. *Journal of Geophysical Research*, 100:421–426.

[Rice University, 2013] Rice University (2013). Physics and Astrononmy department and Atomic and Molecular Collision Group.
$http://www.ruf.rice.edu/\sim atmol/electron\_data.html$ last compiled 05.05.2013.

[Riesen, 2007] Riesen, T. (2007). *Calibration of the ROSINA DFMS in a static and dynamic environment*. PhD thesis, University of Bern, Philosophisch-naturwissenschaftliche Fakultät.

[Schläppi, 2011] Schläppi, B. (2011). *Characterization of the ROSINA Double Focusing Mass Spectrometer*. PhD thesis, University of Bern, Philosophisch-naturwissenschaftliche Fakultät.

[Schläppi et al., 2010] Schläppi, B., Altwegg, K., Balsiger, H., Hässig, M., Jäckel, A., Wurz, P., Fiethe, B., Rubin, M., Fuselier, S. A., Berthelier, J. J., Keyser, J. D., Réme, H., and Mall, U. (2010). Influence of spacecraft outgassing on the exploration of tenuous atmospheres with in situ mass spectrometry. *Journal of Geophysical Research*, 115:12313.

[Schulz et al., 2009] Schulz, R., Alexander, C., Boehnhart, H., and Glassmeier, K.-H., editors (2009). *ROSETTA: ESA's Mission to the Origin of the Solar System*. Springer.

[Schulz et al., 2012] Schulz, R., Sierks, H., Küppers, M., and Accomazzo, A. (2012). Rosetta fly-by at asteroid (21) Lutetia: An overview. *Planetary and Space Science*, 66(1):2–8.

[Schwehm and Schulz, 1999] Schwehm, G. and Schulz, R. (1999). ROSETTA goes to Wirtanen. *Space Science Review*, 90:313–319.

[Svitil and Foley, 2004] Svitil, K. A. and Foley, D. (2004). Beyond pluto. *Discover*, November 2004.

[Tenishev, 2011] Tenishev, V. (2011). Numerical Simulation of Dust in a Cometary Coma: Application to Comet 67P/Churyumov-Gerasimenko. *The Astrophysical Journal*, 732:104:17.

[Tenishev et al., 2008] Tenishev, V., Combi, M. C., and Davidsson, B. (2008). A global kinetic model for cometary comae: The evolution of the coma of the Rosetta target comet Churyumov-Gerasimenko throughout the mission. *Astrophysical Journal*, 685:659–677.

[Tsiganis et al., 2005] Tsiganis, K., Gomes, R., Morbidelli, A., and Levison, H. F. (2005). Origin of the orbital architecture of the giant planets of the Solar System. *Nature*, 435:459–461.

[University of Michigan, 2013] University of Michigan (2013). ICES - Inner Coma Environment Simulator. $http://ices.engin.umich.edu/index.php$ last compiled 05.05.2013.

[Weaver et al., 2008] Weaver, H. A., A'Hearn, M. F., Arpigny, C., Combi, M. R., Feldman, P. D., Tozzi, G.-P., Russo, N. D., and Festou, M. C. (2008). Atomic Deuterium Emission and the D/H ratio in Comets. *Asteroids and Comets and Meteors*, 1405:8216.

[Westermann, 2000] Westermann, C. B. (2000). *A Novel Calibration System for the Simulation of Cometary Atmospheres*. PhD thesis, University of Bern, Philosophisch-naturwissenschaftliche Fakultät.

[Westermann et al., 2001] Westermann, C. B., Luithard, W., Kopp, E., Koch, T., Linger, R., Hofstetter, H., Fischer, J., Altwegg, K., and Balsiger, H. (2001). A high precision calibration system for the simulation of cometary gas environments. *Measurement Science and Technology*, 12:1594–1603.

[Wüthrich, 2007] Wüthrich, S. (2007). *Characterization of the ROSINA DFMS Instrument by Numerical Modelling*. PhD thesis, University of Bern, Philosophisch-naturwissenschaftliche Fakultät.

[Zahnd, 2002] Zahnd, B. (2002). DFMS FM2 Recertification Thermal-Vacuum Test. Technical report, University of Bern.

[Ziurys et al., 1999] Ziurys, L. M., Savage, C., Brewster, M. A., Apponi, A. J., Pesch, T. C., and Wyckoff, S. (1999). Cyabice chemistry in comet Hale-Bopp (C/1995 O1). *Astrophysicsal Journal Letters*, 527:L67–L71.

Acknowledgments

I would like to thank my advisor, Prof. Dr. Kathrin Altwegg for the unique opportunity to write my PhD thesis on such an interesting project as the ROSINA DFMS. I appreciate the many fruitful discussions and the infinite patience as well as the permanent support at any occasions. I also appreciate all the possibilities to attend many meetings and conferences to present our work and enlarge my horizon at countless occasions.

Special thanks go to Prof. Dr. Cécile Engrand from the University of Paris for refereeing this work.

The operation and maintenance of DFMS requires technical assistance from many individuals from the whole physics institute. I owe many thanks to:

- Harry Mischler and the mechanics for helping hands when ever needed.
- Adrian Etter for the support with CASYMIR and CASYMS and helping hands when ever needed.
- Jürg Jost for the repair of the RDP electronics and the GCU.

Furthermore I owe many thanks to:

- Dr. Bernhard Schläppi for the collaboration with DFMS, for the many fruitful discussions and for staying relaxed when DFMS shows unexpected anomalies.
- Dr. Annette Jäckel for all the fruitful discussions, for the support to find references and being there when ever a helping hand or a listening ear is needed.
- Dr. Martin Rubin for all the fruitful discussions, for reading through my thesis and your never ending patience.
- Dr. Léna Le Roy for taking care of DFMS, for the collaboration and for reading through my thesis.
- Dr. André Bieler for the collaboration and for reading through my thesis.
- Ursina Calmonte, Chia-You (Helen) Tzou, Sébastien Gasc and Thierry Sémon for the collaboration.
- Prof. Ernest Kopp for all the fruitful discussions and your help to find pictures.
- Prof. Hand Balsiger as honorary PI and many fruitful discussions.
- Prof. Peter Wurz for the collaboration and the fruitful discussions.
- Brain Magee for reading trough parts of my thesis.
- The ROSINA team members for the collaboration, for advices in many situations, for support and proofreading of drafts.
- Many others for help in administrative and technical matters or being nice roommates.

Finally, I would like to thank my parents and my brother for all their support. Special thanks to Beat who experienced the struggles and the time consuming of such a work first hand. Thank you for bringing me back to Earth again when things tend to get out of hand and make me smile again.

This work was funded by the Swiss National Science Foundation, the Prodex Program of the European Space Agency, and the Kanton of Bern.

Erklärung

gemäss Art. 28 Abs. 2 RSL 05

Name/Vorname:	Hässig Myrtha Marianne
Matrikelnummer:	03-113-388
Studiengang:	Physik
	Bachelor ☐ Master ☐ Dissertation ☒
Titel der Arbeit:	Sensitivity and fragmentation calibration of the ROSINA Double Focusing Mass Spectrometer
LeiterIn der Arbeit:	Prof. Dr. Kathrin Altwegg

Ich erkläre hiermit, dass ich diese Arbeit selbständig verfasst und keine anderen als die angegebenen Quellen benutzt habe. Alle Stellen, die wörtlich oder sinngemäss aus Quellen entnommen wurden, habe ich als solche gekennzeichnet. Mir ist bekannt, dass andernfalls der Senat gemäss Artikel 36 Absatz 1 Buchstabe r des Gesetztes vom 5. September 1996 über die Universität zum Entzug des auf Grund dieser Arbeit verliehenen Titels berechtigt ist.

…………………………………………………………

Ort/Datum

…………………………………………………………

Unterschrift

Curriculum Vitae

Personal Data

Name: Hässig
First Name: Myrtha Marianne
Date of birth: 13.07.1984
Adress: Dorfstrasse 2, 3655 Sigriswil, Switzerland

Education

1991-1997	Primary school in Sigriswil
1997-1999	Secondary school in Sigriswil
1999-2003	Grammar school in Thun-Schadau
2003	Matura at Gymnasium Thun-Schadau main focus physics and applied mathematics

Academic record

2003-2008	Studies at the University of Bern in experimental physics, mathematics and philosophies (science history and science theory)
2007-2008	Master's thesis in physics at the Institute of Applied Physics, University of Bern, Division of Laser Physics, entitled: "Optical fibers with a conductive core", Supervisor: Prof. Dr. Willy Lüthy
2008-2010	Diploma of teaching physics at grammar school of PH Bern
2009-2013	PhD thesis in experimental physics at the physics institute, University of Bern, Division of Space Research and Planetary Science, entitled: "Sensitivity and fragmentation calibration of the ROSINA Double Focusing Mass Spectrometer", Supervisor: Prof. Dr. Kathrin Altwegg

Professional Training

2002-2006	Internship at the engineering department of Frutiger AG (construction firm) in Thun
2008-2012	Teaching physics at Gymnasium und Fachmittelschule Thun-Seefeld
2009-2013	Teaching assistant at University of Bern of physics exercises and laboratory classes for students of medicine and other branches